University of Leoben

Microstructural evolution during SPD of AlCu3

Diploma Thesis

by

Michael Josef Faller

This work was done at the Erich Schmid Institute of Materials Science of the Austrian Academy of Sciences and the Department Materials Physics of the University of Leoben.

Leoben, September 2010

Gewidmet meinem Grossvater Josef Faller sen.

by Dan Perjovschi

Danksagung

Zuallererst möchte ich mich bei den "Masterminds" des Erich Schmid Instituts, Herrn Prof. Reinhard Pippan and Herrn Prof. Gerhard Dehm für die vertrauensvolle Vergabe dieser Diplomarbeit, ihre Gelassenheit über meine Fehler hinwegzusehen, und ihre ständige Gesprächsbereitschaft bedanken. Die Betreuung durch Herrn Prof. Pippan, die Möglichkeit so selbsverantwortlich alle Einrichtungen zu benutzen, grundsätzlich alle Freiheiten die ich bei der Arbeit am Institut genossen habe, sind an dieser Universität wohl einzigartig.

Den "Spirit" des Erich Schmid Institutes formen meiner Meinung nach alle seine Mitarbeiter mit ihrem hilfsbereiten, freundlichen und homorvollen Umgang miteinander, und so denke ich haben zum Gelingen dieser Arbeit alle beigetragen. Danke!

Ich bedanke mich besonders bei der gesamten SPD-Gruppe um Prof. Pippan, bei Stephan Scheriau und Toni Hohenwarter sowie bei Andrea Bachmaier, Georg Rathmayer und Christoph Kammerhofer, die mir viele wertvolle Tipps gegeben und mir immer bereitwillig mit Rat und Tat geholfen haben. Danke Euch!

Mein aufrichtiger Dank gilt auch dem Werkstättenteam, den "alten Hasen" Günther Aschauer und Franz Hubner, für ihre Hilfe. Es war ein Genuß, in technischer wie in kulinarischer Hinsicht, von ihnen etwas zu lernen.

Bei "Doris" Schrutt und "Marianne" Fließer bedanke ich mich sehr für die unkomplizierte Erledigung aller administrativen Angelegenheiten, mögen sie mir meine Schwächen verzeihen. Wenn es EUCH nicht gäbe....

Besonderer Dank gebührt den Damen der Metallographie, Edeltraud Haberz, Gabi Moser und Silke Modritsch. Letzlich ist ihnen die erfolgreiche SEM- und TEM-Probenpräparation zu verdanken, und ich hoffe sie verzeihen mir meine Hartnäckigkeit und Zweifel.

Dem wahren "Meister des Aluminium", Herrn Peter Kutlesa, danke ich für die informativen und kurzweiligen Rauchpausen sowie für seine Hilfsbereitschaft bei den HPT- und Auslagerungsversuchen.

Für die Unterstützung bei der TEM-Probenpräparation, und ihre Geduld in den Übungsstunden am Mikroskop, möchte ich mich bei Christiane Vieh herzlich bedanken. Außerordentlicher Dank gebührt Frau Boriana Rashkova die mir einen Einblick in die Arbeit mit dem TEM gegeben, mir mit Engelsgeduld beim Auswerten der Beugungsbilder geholfen, und mich auch in moralischer Hinsicht sehr unterstützt hat. Herrn Jörg Thomas danke ich für die prompte Hilfe bei allen technischen Problemen und Problemchen mit dem Mikroskop.

Ich möchte die Gelegenheit nutzen und mich an dieser Stelle auch bei Herrn Prof. Ingomar Jäger und Herrn Dr. Thomas Schöberl bedanken. So "oberflächlich" und von Vakuum geprägt die Zusammenarbeit mit ihnen aus fachlicher Sicht auch war, so sehr habe ich sie in menschlicher Hinsicht zu schätzen gelernt. Die Erfahrungen die ich bei der Arbeit mit ihnen sammeln durfte möchte ich keinesfalls missen.

Selbstverständlich müssen im Rahmen dieser Danksagung auch die werten Herrn Studienkollegen Otsch, Franz, Fuuz, Bernd, Moki, Arek und Christian zum Zug kommen: Danke für die unvergessliche Zeit.

Danke auch an die "Homeys": Exxe, Lex, Hannes, Adi, Alex, Chekov, Babsi, Flow, Gabi, Holy, Rö, Krämmaling, Matze, Michl, Anita, Katl, Petz, Marko, Lisl, Renne, und und und... bei eich is "Daham".

Großer Dank gebührt meiner ganzen Familie, insbesondere meinen Eltern, die mir dieses Studium erst ermöglicht haben.

Dem FWF (Projekt S10402-N16) danke ich für die finanzielle Unterstützung dieser Arbeit.

Affidavit

I declare in lieu of oath, that I wrote this thesis and performed the associated research myself, using only literature cited in this volume.

Leoben, September 2010 Michael Faller

Task

Materials processing by severe plastic deformation (SPD) is a main topic at the Erich Schmid Institute of Materials Science (ESI). To extend the variety of single phase and composite materials already investigated concerning their behavior during SPD, in this work the deformation behavior of an age hardening Al-3wt%Cu model alloy should be studied by high pressure torsion (HPT). HPT processing at various deformation temperatures of three for age-hardening alloys typical material conditions, such as solution-treated, peak-aged and over-aged, as well as annealing and aging of the material after deformation, may give a further understanding of the phenomena during and after SPD of age-hardening alloys. Microhardness measurements are supposed to be a sufficient method to characterise the mechanical properties, while the occurring microstructures should be investigated by scanning and transmission electron microscopy.

Leoben, June 2009 Univ.-Prof. Dipl.-Ing. Dr.mont. Reinhard Pippan

Abstract

By severe plastic deformation (SPD) ultra-fine-grained (UFG) materials can be produced. Because of their extraordinary mechanical and physical properties such materials are of scientific interest and promising for future technical applications. Of all established SPD techniques high-pressure-torsion (HPT) offers the major deformation potential and the feasibility of a saturation in structural refinement. In SPD-processed single-phase metals the occurring UFG microstructures are thermally not very stable. SPD deformed metal-matrix composites show enhanced structural refinement and thermal stability. Age-hardening alloys can be seen as chemical composite materials. By sufficient heat treatments various phases can be introduced, which may influence the limit of refinement and stabilize the occurring microstructure. In this work an age-hardening Al-3wt%Cu model alloy was studied, to get a better understanding of the phenomena in age-hardening alloys during and after SPD. Samples were heattreated to different material conditions and HPT deformed at various temperatures. During deformation the torque was recorded and HPT-deformed specimens were subsequently aged. The mechanical properties were characterised by micro-hardness measurements and the occurring microstructures were investigated by scanning electron microscopy and transmission electron microscopy. By HPT-processing the investigated Al-Cu alloy an UFG structure was obtained. During deformation the hardening precipitates are disrupted and possibly dissolved. The resulting microstructure consists of mainly high-angle grain boundaries with incoherent grain-boundary precipitates. SPD up to very high strain possibly leads to a structure independent from the initial material condition. The grain-size increases with increasing deformation temperature and decreases with decreasing particle size of the second phase. According to the Hall-Petch relation the strength of the deformed material is mainly governed by the grain size. When aging the deformed material, hardening phases could not be found. Only the incoherent grain boundary precipitates were found to grow, supposedly by interfacial diffusion of copper. Grain-growth during aging seems to be limited by the grain boundary precipitates.

Contents

Chapter 1.

Introduction

The Al-Cu alloy system is the classic example for age hardening alloys. First discovered by Alfred Wilm in 1909 (Duralumin) [1] it nowadays forms the basis for the high strength aluminum alloys of the 2xxx series, mostly used for light-weight applications mainly in the automotive and aviation industries. The binary Al-Cu system is a model alloy, while commercial alloys usually have defined contents of Zn, Mn, Mg, Fe, and Si added. The strength of these alloys is based on the formation of homogeneously distributed intermetallic precipitates of Al and the alloying elements achieved by a special heat treatment referred to as aging. Serving as obstacles, the precipitates have to be either cut or bypassed by dislocations and therefore raise the yield stress of the material. The gain in mechanical strength depends on volume fraction, the size and the mean distance of the precipitates and can be adjusted by the amount of alloying elements as well as varying duration and temperature of the heat treatment.

Over the last 15 years, methods for materials processing by severe plastic deformation (SPD) to obtain ultra-fine-grained materials (UFG) have been developed. The major methods already established for the fabrication of UFG materials are high pressure torsion (HPT), twist extrusion (TE), multi directional forging (MDF), equal-channel angular pressing (ECAP), accumulative roll-bonding (ARB), cyclic extrusion and compression (CEC), and repetitive corrugation and straightening (RCS)[2][3]. Materials processed by SPD show extraordinary physical and mechanical properties with a high potential for future applications but are, in conjunction with modern methods of investigation, also of great scientific interest giving a further insight into the fundamentals of the plastic deformation behavior of materials. HPT is of special interest as it gives the opportunity to deform a large variety of materials by simple shear under hydrostatic pressure to extremely high strains without loss of shape.

In metals high plastic deformation leads to a refinement in the microstructure. In many materials severely deformed to very high strains, a saturation in refinement is observed. The resulting granular microstructure contains mainly high-angle grain boundaries with grain sizes in the submicrometre and nanometre range. In single-phase materials, alloying, the temperature and the strain path are the most important parameters

controlling the saturation in structural refinement[4]. The behavior of dual and multiphase materials is more complex: it varies from simple homogenization of the phase distribution, fragmentation of one phase to disintegration and supersaturation of the phases [4]. Consolidation of fine powders by HPT is a very interesting field as it discloses opportunities to produce UFG metal matrix composites that show enhanced stability [5]. Powder treatment and/or mixtures with various dispersions are new parameters to influence the limit of refinement.

The mechanisms involved in maintaining a saturated strength and structure during deformation are still under discussion. The same amount of dislocations produced by the applied strain has to be annihilated to keep the dislocation density balanced. Furthermore, to keep up a constant boundary length in saturation, the generation and annihilation of boundaries has to be be in equilibrium.

Age-hardening alloys can be seen as chemical composite materials. Various phases that may influence the structural refinement can be introduced by different heat treatments. During and after HPT processing the formation, dissolution or transformation of precipitates are facilitated by the influence of a huge amount of defects introduced during deformation. The thermodynamics of the occurring reactions are influenced by temperature but may also depend on the applied pressure. Possibly the occurring phases can stabilize the UFG microstructure generated by SPD.

In order to understand better the phenomena in age-hardening alloys during and after SPD, in this work a model binary precipitation hardening Al-3wt%Cu alloy was heat treated (aged) to different conditions and HPT deformed at various temperatures into or at least near to the saturation regime. During HPT deformation the resulting torque was recorded and HPT deformed samples where subsequently aged/annealed. The mechanical properties were characterized by microhardness measurements, while ocurring microstructures were investigated by SEM and TEM.

Generally this report is divided into two parts. Firstly the aging characteristic of the original material is determined. Based on the results, HPT experiments were performed, which will be outlined and discussed in the second part.

Chapter 2.

Ageing Characteristic of the Raw Material

2.1. Overview

The phenomenon of age- or precipitation-hardening in the Al-Cu alloy system was very intensively researched since its fortuitous discovery by A.Wilm in 1909 (Duralumin). Hence in this chapter only the most important facts about age hardening will be repeated besides the description of the conducted experiments and the results obtained. More details about thermodynamics and growth kinetics can be found in the standard work of Porter and Easterling [6], while references [7], [1] and [8] also discuss in more detail the occurring strengthening mechanisms. This chapter mainly refers to these books as source of figures and the theoretical background.

To find suitable heat treatments for samples to be deformed by HPT, the aging characteristic of the raw material was investigated with three different types of samples. On heat-treated specimens Vickers micro-hardness measurements were carried out to characterize the mechanical properties. The coarse cast structure could be seen with the naked eye by etching, and was recorded by digital reflex camera. Shape and size of the precipitates were investigated by TEM. Electro polishing was tried out as a preparation method for SEM analyses.

2.2. Age-hardening of Al-Cu

Looking at the Al-rich end of the Al-Cu phase diagram shown in figure 2.1 one can see that it is possible to bring up to 5.65wt% copper into solid solution in the fcc aluminum crystal at 548°C. This partial solubility of Cu in Al is a basic requirement for age- or precipitation-hardening. If an alloy with the composition of Al-3wt% Cu, as investigated in this work, is heated to 550°C all copper is in solid solution as a stable fcc α phase. By quenching the specimen rapidly, e.g. in cold water, there is no time for any transformation to occur so that the solid solution is retained largely unchanged to room temperature. Now the solid solution

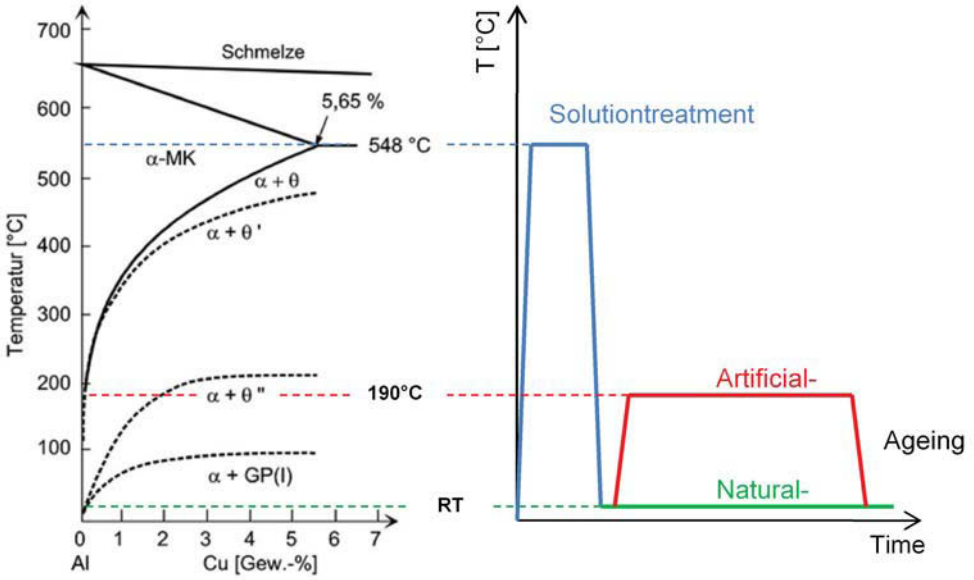

Figure 2.1.: *Al-rich end of the Al-Cu phase diagram and schematic illustration of heat treatment.*

is supersaturated with Cu and there is a driving force for precipitation of the equilibrium θ phase.

If the alloy is now held for a period of time at room temperature (natural aging) or artificially aged at elevated temperatures up to 200°C, schematically depicted in figure 2.1, it is found that the precipitation process does not start with the equilibrium θ phase but follows a precipitation sequence of metastable phases shown in figure 2.3. The evolution of hardness depends on aging time and temperature and is depicted in figure 2.2 for various Al-Cu alloys. Higher copper contents provide a higher volume fraction of precipitates and therefore higher peak hardness. Due to the lower driving force at higher aging temperatures, early stages of the precipitation sequence are skipped and the precipitates become larger, while peak hardness is reached earlier due to the higher diffusion rate. According to the lower plot in figure 2.2, for the experiments with the 3wt%-Cu alloy in this work, a temperature of 190° was chosen for artificial aging to keep aging time in a practical range. At elevated aging temperatures, precipitates form by a conventional nucleation and growth mechanism, while during quenching, the Cu atoms may gather to GP zones by a spinodal type of decomposition. Natural

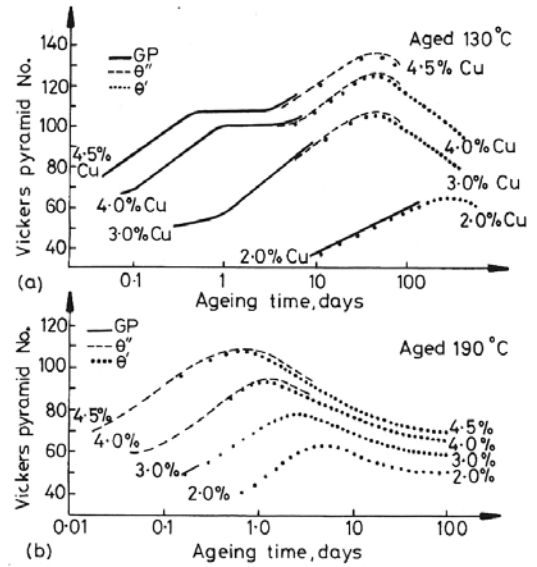

Fig. 5.37 Hardness v. time for various Al–Cu alloys at (a) 130 °C (b) 190 °C. (After J.M. Silcock, T.J. Heal and H.K. Hardy, *Journal of the Institute of Metals* **82** (1953–1954) 239.

Figure 2.2.: *Hardness vs. time for various Al-Cu alloys from [6].*

aging is governed by the presence of (thermal) vacancies trapped by quenching from the temperature of solution treatment. Besides the balance of volume and interfacial energy, the particle shape is mainly determined by the elastic anisotropy of the crystal structure coupled with the misfit of the lattice parameters, to minimize elastic strain energy. For Al-Cu with misfit in atomic radius of 10% and a fcc α matrix, the preferred shape is disc-like with the large face parallel to the softest crystallographic direction.

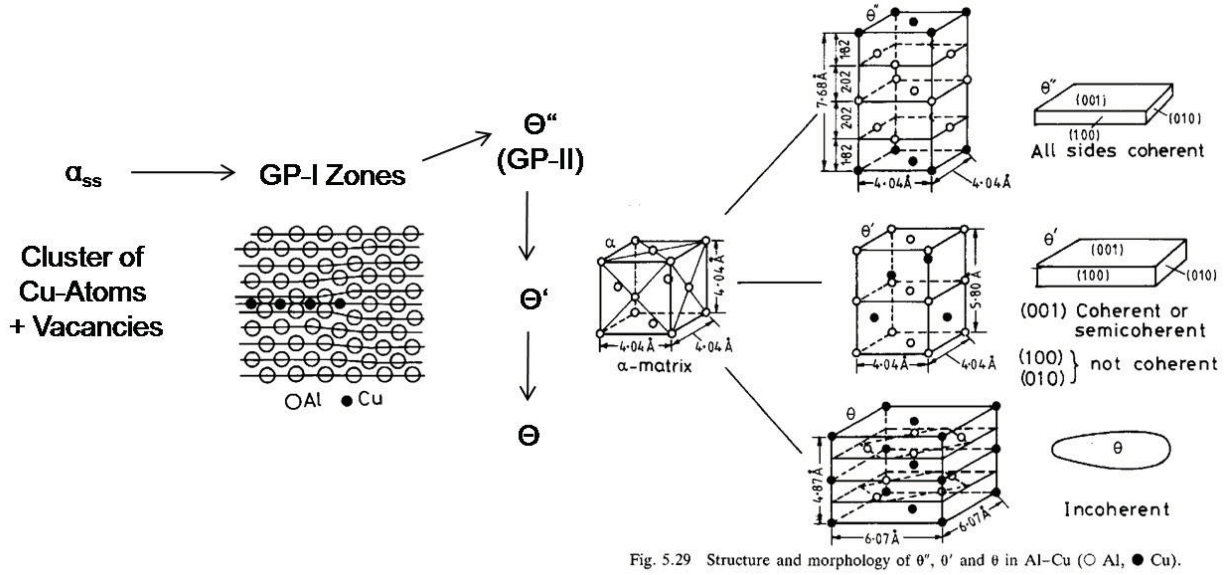

Fig. 5.29 Structure and morphology of θ″, θ′ and θ in Al–Cu (○ Al, ● Cu).

Figure 2.3.: *Illustration of the full precipitation sequence. Structure and morphology of the occurring phases.*

The GP zones, named after the discoverers Guinier and Preston, are coherent mono-atomic plates of Cu atoms formed, due to the elastic energy component of the solid-solid transformation, parallel to {100} planes of the α lattice. The GP-II zones or θ” can be seen as a superstructure of GP-I layers spaced by three layers of Al atoms but also represent a transition phase to the more complex tetragonal θ’ structure at elevated temperatures. The strengthening effect of the coherent particles is dominated by long-range coherency-stress fields in their surroundings. Small precipitates of θ’ may still be coherent with the Al matrix along their largest face, but with increasing particle size the misfit is accommodated by edge dislocations along the interface to reduce elastic strain. During artificial aging the incoherent θ phase forms by heterogeneous nucleation mainly at grain boundaries, leaving a more-or-less pronounced precipitation-free zone in their vicinity, dependent on quenching speed and aging temperature, as grain boundaries are sinks for vacancies, needed for zone formation[9]. Since the region surrounding large incoherent particles is relaxed by dislocations, strengthening and the loss of strength with increasing particle size can be described by the Orowan mechanism.

2.3. Sample Preparation and Hardness Measurement

The original material was a cast bar of about 60×100×10mm with some excess material from the sprue at one edge. The first more-or-less irregularly shaped samples, some shown in figure 2.4(a), were cut from this excessive part by a *Struers Secotom-10*. These specimens will be referred to as A samples hereafter. The remaining part was homogenized for three days in a chamber furnace in air, starting at 480°C and increasing the temperature in steps of 50°C every 24 hours to avoid partial melting of liquation, possibly formed during casting, and was subsequently quenched in tap water of about 15°C. Using a cutting wheel the bar was sectioned into pieces of 10×10×25mm from which the consistently shaped specimens where cut as depicted in figure 2.4(b) and will be referred to as B and C samples hereafter. The B samples are 10×5×2mm, the C samples 2×2×5mm in size.

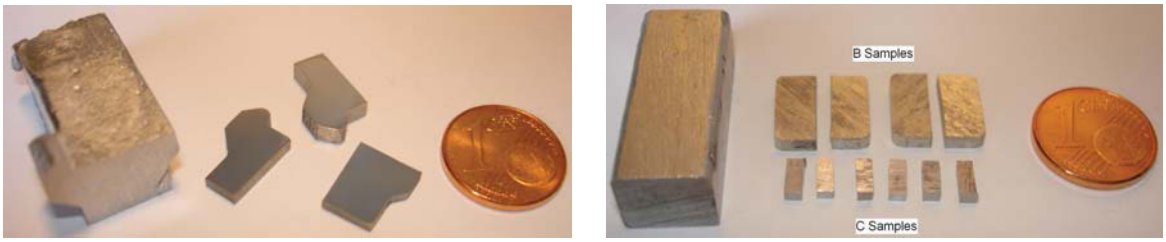

(a) (b)

Figure 2.4.: *Samples of raw material from, excess material of the sprue for A samples(a), homogenized material for B and C samples(b).*

2.3.1. Solution Treatment and Aging

The samples were put on a metal sheet as depicted in figure 2.5(b) and solution treated for 3 hours at 550±5°C in air using the furnace depicted in figure 2.5(a). Since there is a temperature gradient from top to bottom inside the chamber, a Ni/CrNi thermocouple, spot-welded on a reference specimen, was placed at the height of the samples to adjust the temperature as exactly as possible. Subsequently the specimens were quenched in cold tap water. A and B samples were placed randomly on the metal sheet while the C samples were laid along the edge to provide more even quenching conditions. Some of the C samples were kept at room temperature after quenching to see the effect of natural aging.

Using the drying oven depicted in figure 2.5(c), the A and C samples were artificially aged at 190°C, the B samples, by mistake, at 180°C. The short-term samples were dipped in oil, kept in a small jar inside the oven, while the intermediate and long term samples were placed on an aluminum profile and on small glass plates shown in figure 2.5(d). In logarithmic time steps specimens were taken out of the oven and cooled to room temperature in air.

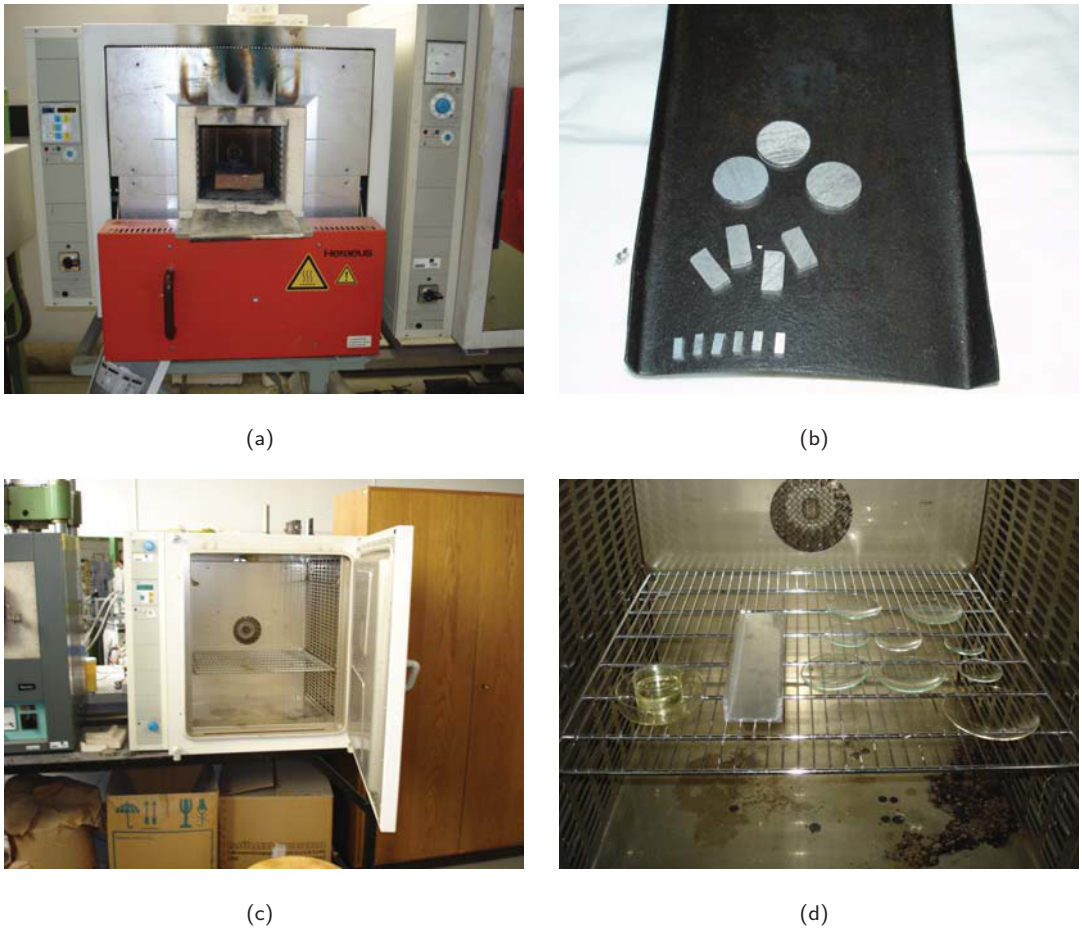

(a) (b)

(c) (d)

Figure 2.5.: *Furnace used for solution treatment (a). Samples on a metal sheet as placed inside the furnace (b). Drying oven used for artificial aging (c). Sample containers and oil jar inside the oven (d).*

2.3.2. Microhardness Measurements

For hardness measurements one sample-surface was ground on a *Struers LaboPol-25* device using abrasive paper in four grit steps, P400, P800, P1200 and P2500, and further polished by hand on a soft polishing disc using 0.3μm alumina/water suspension. The dimensions of the specimens vary, because of the imprecise cutting. Therefore the hardness indents were placed oriented to the center of the samples, as illustrated in figure 2.6. The micro hardness was measured using a Vickers indenter on a *Buehler Omnimet 5104* device equipped with a CCD camera for digital image processing. All indents were done with a load of 200gf for 10s. For better comparability the indents sizes were measured automatically with the *Omnimet MHT 7.1 REV 4* software. Frequently performed manual corrections did not change values more than one unit on the scale of hardness. The load of 200gf was chosen so that at the highest magnification, the software window-frame just covered the indent size of the lowest hardness values observed. It was assumed that in this case highest accuracy is given while the largest indents were just small enough not to influence each other in a distance of $\approx$0.4 mm according to the rule of thumb: distance $\geq$ indent size $\times$ 3.

On the A samples 5 to 10 indents where placed more-or-less randomly on the surface. The indents on the B and C samples were made along the center line on the surface at intervals of 1 mm (B samples) and 0.5 mm (C samples) as shown in figure 2.6.

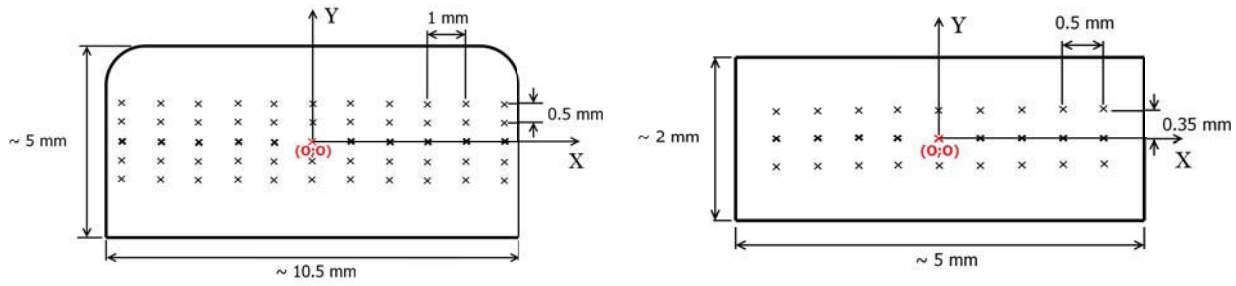

(a) B Sample (b) C Sample

Figure 2.6.: *Schematic illustration of the grid of micro-hardness indents as made on (a) B samples and (b) C samples.*

Since the process of natural aging starts instantly after quenching, even the solution treated samples are naturally aged for the time of grinding and polishing until the micro hardness was measured. To get an impression of the surface-hardness distribution, on three B samples a grid of indents was made as depicted in figure 2.6(a). One solution treated C-sample was cut into two halves to see the difference between bulk and surface hardness after quenching, as sketched in figure 2.7. On the faces, corresponding to the colored faces in figure 2.7, a grid of indents was made as illustrated in figure 2.6(b).

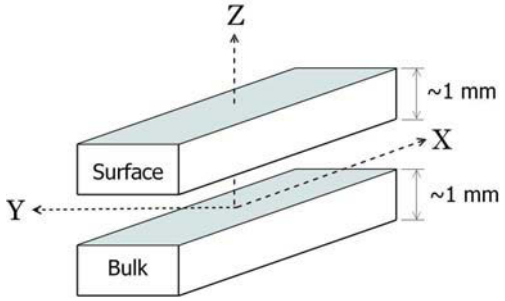

Figure 2.7.: *Sketch of a halved C sample, for comparison of surface and bulk hardness.*

The images in figure 2.8 reveal a very coarse grain structure of the homogenized original material. The structural size covers approximately the size of the C samples as well as the distance between the micro-hardness indents illustrated in figure 2.6. One can expect that the hardness values are associated with errors like load dependence and the influence of the crystallographic orientation. Consequently comparison with other specific values should be considered carefully.

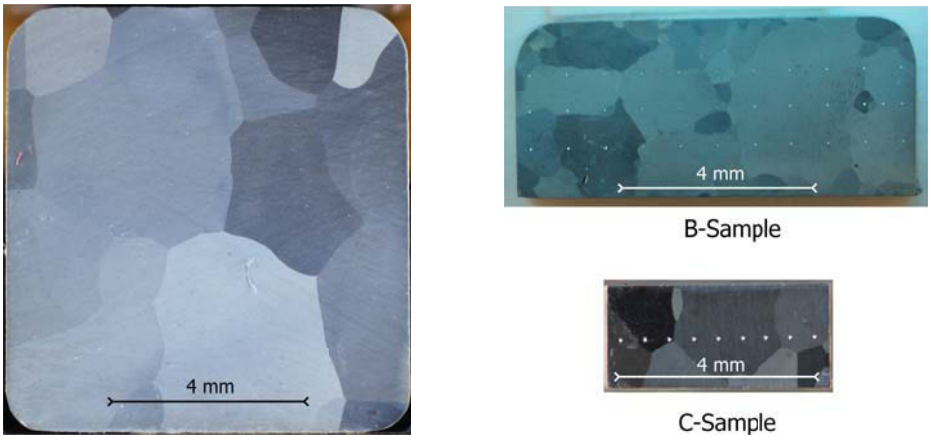

(a) (b)

Figure 2.8.: *Illustration of the grain structure of the raw material. (a) Polished and etched cross-section of a homogenized bar. (b) Images of a B sample and a C sample, etched after polishing and hardness measurement. The images were taken with a digital reflex camera.*

2.4. Pretest

For the first experiments A samples (figure 2.4(a)) were solution-treated and artificially aged at 190°C as described previously in Section 2.3. The resulting aging characteristic is shown in figure 2.9(a). Because of large scatter and the poorly defined peak the experiment was repeated with more consistently-shaped B samples and better defined placing of the hardness indents. In this case by mistake the oven used for aging was set to 180°C. Peak hardness is a little lower for the B samples but its approach is much better pronounced, while the scatter remains. The rule of thumb, predicting a doubled aging time for a 10°C reduction in temperature, seems to be well fulfilled.

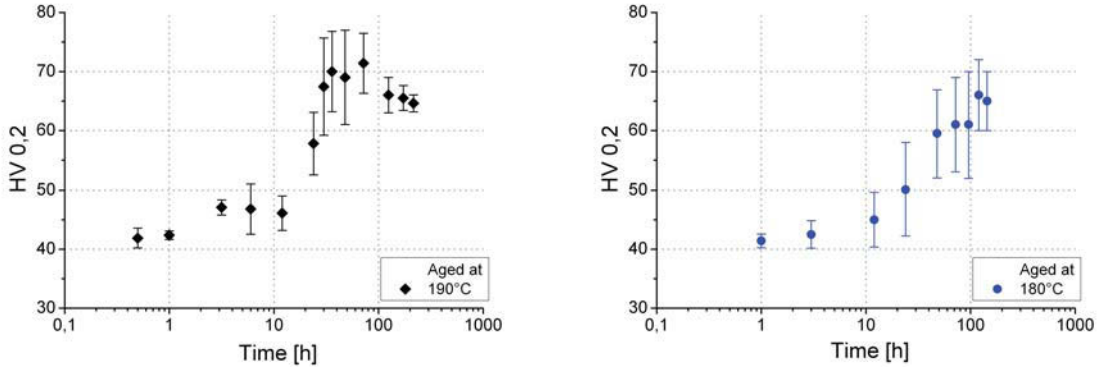

(a) A Samples (b) B Samples

Figure 2.9.: *Aging characteristic expressed as hardness vs aging time of (a) A samples aged at 190°C and (b) B samples aged at 180°C.*

A closer look at the hardness distribution on the surface of near peak aged B samples is given in figure 2.10 and reveals not a stochastic scatter but patterns in hardness values. Especially pronounced on the sample aged for 144h (figure 2.10(d)) is a decrease in hardness from the edges towards the center in X direction and similarly but less pronounced from top to bottom along the Y axis. The hardness distribution possibly reflects the grain structure as well as the transfer of heat during quenching. Assuming that higher cooling rates lead to finer dispersion of precipitates forming during aging, it appears that the 144h sample faced the water quench maybe with either the far right or left ridge. The 120h sample (figures 2.10(a) and (b)) might have hit the water with the top right edge first. The data points in figure 2.9(b) are mean value and standard deviation of the hardness measured along the X axis in the center of the samples. Hence the 120h and 144h values in 2.9(b) correspond to the black curves in figure 2.10(a) and (c). The remaining samples were handled in the same way, but only setting one line of indents as indicated by the thick crosses in figure 2.6(a). The full data set can be found in the appendix.

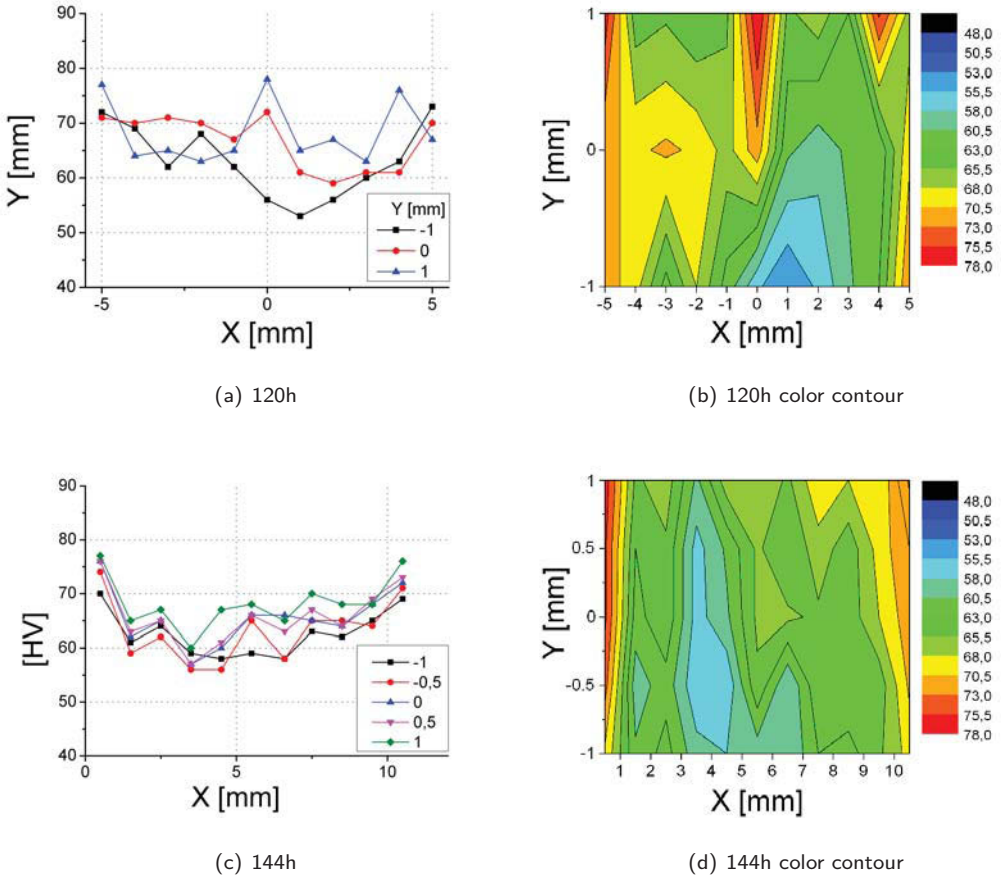

(a) 120h

(b) 120h color contour

(c) 144h

(d) 144h color contour

Figure 2.10.: *Microhardness distribution on the surface of near peak aged B samples, aged at 180° C for 120h (a) and 144h (c) and the associated color contours (b) and (d).*

2.5. Ageing Characteristic

The geometry of the C samples, shown in figure 2.4(b), was consequently chosen just small enough to place at least nine hardness indents along the larger face, as schematically depicted in figure 2.6(b). Due to more even distances for heat transfer and faster quenching, less scatter in measured hardness was expected. Naturally the process of aging starts instantly when taking the samples out of the furnace at solution-treatment temperature. Therefore all samples were quenched in air at room temperature for some seconds during transfer to the water quench, and naturally aged for the term of preparation. Hence for the far left starting point in figure 2.11(a), showing the natural aging behavior, a term of three hours for preparation was estimated. Figure 2.11(b), depicts the characteristic artificial aging behavior.

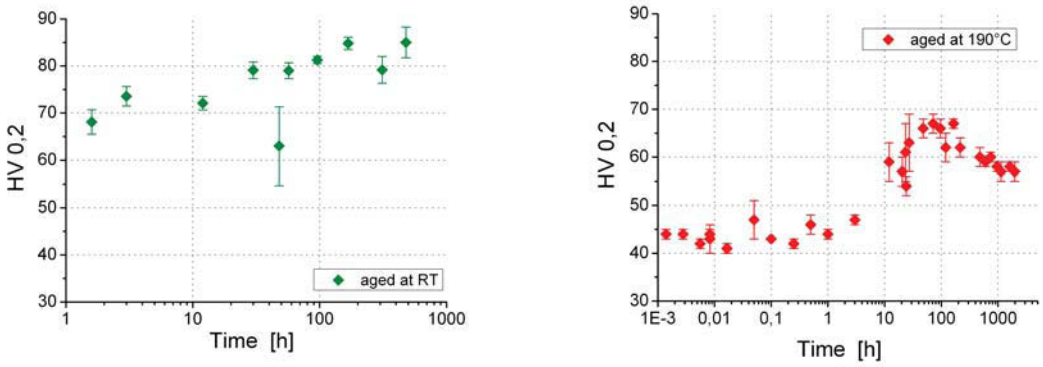

Figure 2.11.: *Aging behavior of C samples quenched and, aged at RT (a), aged at 190°C(b). Note the differing time scales.*

The high hardness of the naturally aged samples is a result of the formation of GP zones during quenching. Comparing the hardness of naturally and artificially aged specimens in figure 2.11(a) and (b), the process of zone formation is reversed within a few seconds by dipping as-quenched samples into oil heated to the typical aging temperature. The process of zone formation is governed by the concentration of vacancies retained to room temperature by quenching. Quenched-in vacancies are assumed to provide a clustering-rate of Cu atoms that is many orders of magnitude greater than calculations, using extrapolated data from diffusion experiments at higher temperatures, would predict. Energetically favored vacancy-Cu pairs may play a special role [1]. The increase in strength during natural aging is dominated by long-range stress fields surrounding solid solution atoms and coherent GP zones. Dislocations are forced to bow between the (coherency) stress fields as illustrated in figure 2.12(a). By deformation small particles are sheared by dislocations if the dislocations bowing stress exceeds the stress needed to cut a particle. Shearing of particles generates new particle-matrix interface, as schematically shown in figure 2.12(b). The bowing-radius depends on particle spacing.

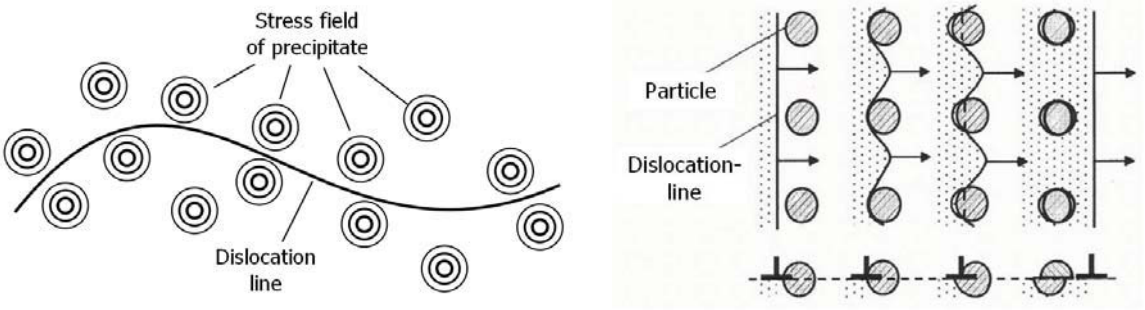

Figure 2.12.: *(a) Dislocation line between strain fields of particles. (b) Particles as obstacles for dislocation movement. The bowing radius depends on particle spacing. By cutting new interface is created.*

The strengthening mechanism changes because of growth and structural changes of the precipitates with preceding aging time. Increasing particle size increases the stress needed for cutting. With increasing particle spacing, the dislocation lines can bow further in between the precipitates. For large widely spaced particles, it is energetically favored to close the bending dislocation line behind the obstacle, leaving a dislocation loop behind, as sketched in figure 2.13. This is referred to as the Orowan-mechanism.

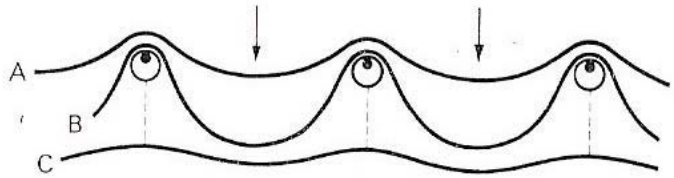

Figure 2.13.: *Schematic dislocation lines passing between widely spaced particles. When bypassing an obstacle, each dislocation leaves a dislocation loop behind.*

In the early stages of the aging process, starting with all copper in solid solution, precipitates continuously form and grow and thereby the hardness of the material increases. The primarily formed particles are small enough to be sheared by dislocations and the cutting mechanism governs the deformation behavior. For a certain volume fraction of hardening particles (when all copper is precipitated), at the point of optimal size to distance ratio hardness reaches a maximum. The material is then referred to be in peak-aged condition. For longer aging times beyond peak-strength, the increasing particle size and spacing allows further bending of dislocation lines in between particles. Bypassing of precipitates according to the Orowan-mechanism starts to dominate. The hardness henceforward decreases and the material is then in so called over-aged condition.

The shape of the aging characteristic can be explained by these two mechanisms, as outlined in figure 2.14(b) in comparison with selected data points of the aging characteristic determined for C-samples. The larger

scatter in hardness values around 24 hours in figures 2.11(b) and 2.14(a) possibly indicates the transition from shearing to bypassing of particles by dislocations.

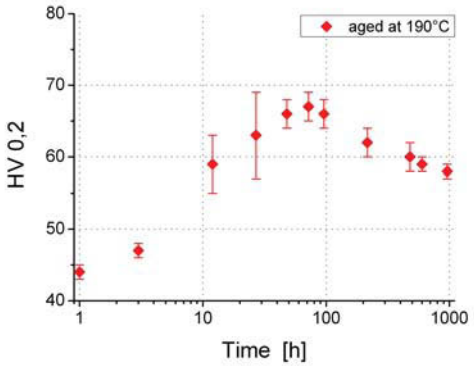

(a)

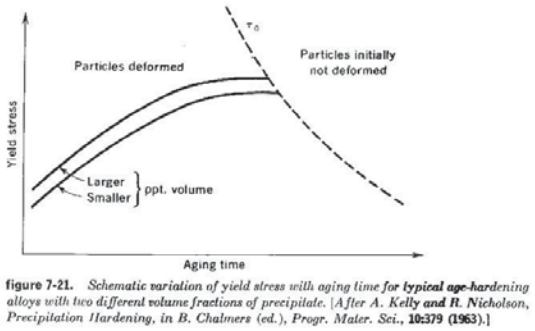

figure 7-21. *Schematic variation of yield stress with aging time for typical age-hardening alloys with two different volume fractions of precipitate. [After A. Kelly and R. Nicholson, Precipitation Hardening, in B. Chalmers (ed.), Progr. Mater. Sci., 10:379 (1963).]*

(b)

Figure 2.14.: *Comparison of measured variation of the hardness and the predicted behavior. (a) Selection of data points from Figure 2.11. (b) Schematic shape of the curve related to particle strength for two different volume fractions.*

The difference between surface and bulk hardness of a quenched sample, is illustrated in figure 2.15. Both profiles show a similar pattern.

The higher bulk-hardness may be related to the formation of GP zones. A slower cooling rate in the bulk of the sample may result in a higher rate of zone formation. The precipitates and their surrounding strain fields are strictly oriented and dislocation movement is correspondingly limited. A distinct anisotropic deformation behavior may explain the large scatter of values measured in the bulk.

A lower fraction of zones near the surface would add up to a higher copper-concentration in solid solution, providing more isotropic dislocation interaction. Thermally activated dislocation movement may facilitate balancing of the occurring thermally induced stress and strain fields.

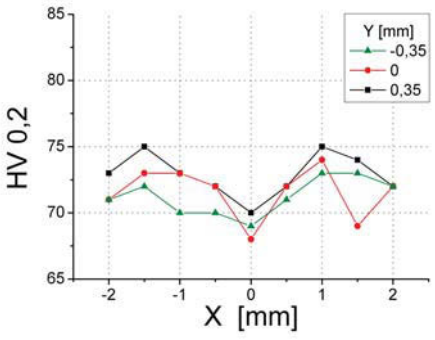

(a) Surface

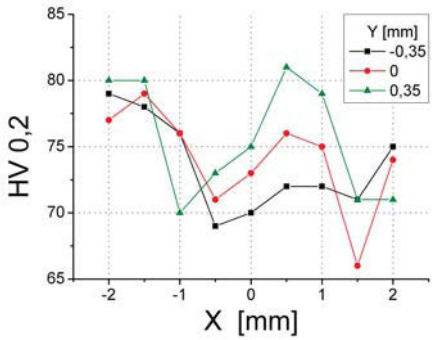

(b) Bulk

Figure 2.15.: *Hardness distribution on a quenched C sample along the surface (a) and in the bulk (b).*

2.6. Heat treatment for HPT experiments

Based on data obtained from C samples (shown in figure 2.16) three material conditions were defined. The corresponding heat treatments, that samples for the HPT experiments were subjected to, are summarized in table 2.1. In the following chapters the condition indexes in table 2.1 will be used for short designation.

Table 2.1.: *Heat treatment for three defined conditions.*

Condition Index	Heat treatment
S	• Solution treated at 550°C for 3 hours • Quenched in tap water at 15°C • (Aged at RT during preparation)
PA	• Solution treated like S • Aged at 190° for 3 days
OA	• Solution treated like S • Aged at 190° for 3 weeks

The colored inserts in figure 2.16 indicate the range of hardness of the three typical conditions. The S samples for HPT deformation were naturally aged for 1 hour minimum, required to set up the HPT equipment, and a maximum of 8 hours for the last specimen deformed on one working day. For PA and OA condition, solution treated specimens were transferred to the drying oven immediately after quenching.

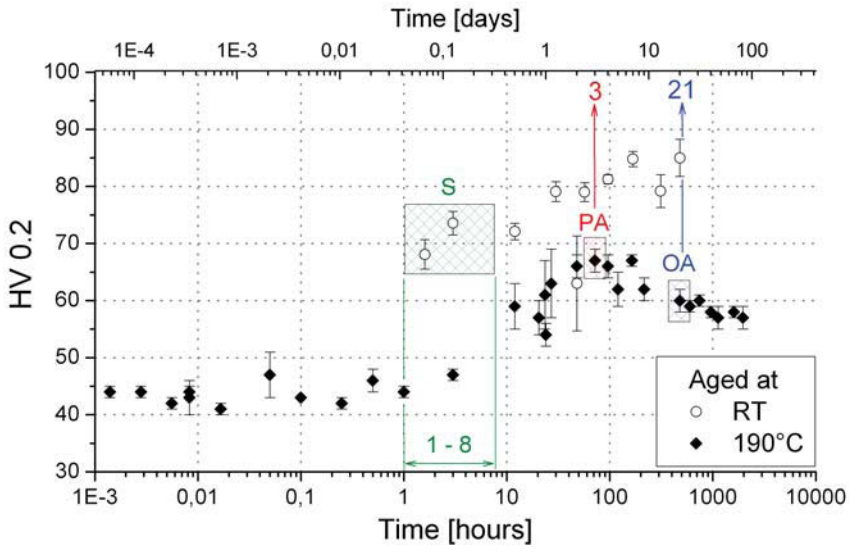

Figure 2.16.: *Aging characteristic of the raw material measured on C samples aged at 190°C and at room temperature and illustration of the samples used for the HPT deformation.*

Chapter 3.

HPT Experiments

3.1. About HPT

The principle of what is nowadays known as HPT, the effects of deforming materials by high shearing stress combined with high hydrostatic pressure, was already investigated very early by P.W. Bridgeman in the 1930s[10]. Methods under the term of severe plastic deformation (SPD) using simple shear under high pressure such as HPT and ECAP have been intensively investigated and developed since the 1990s[3]. HPT is especially attractive because it offers the highest deformation potential of all established SPD techniques for a large variety of materials. Even in geo-sciences HPT methods are used to simulate rock deformation on a laboratory scale.

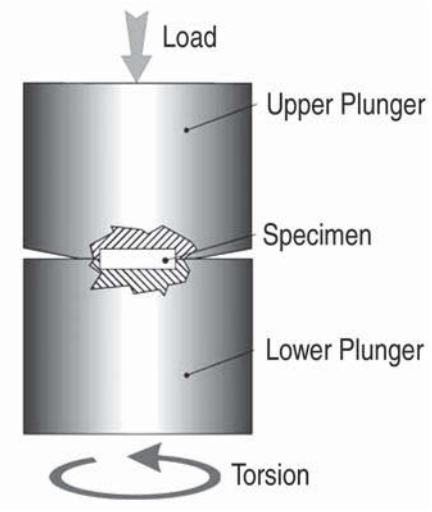

Figure 3.1.: *HPT tool with cavities in both anvils [3].*

A typical HPT device works basically as sketched in figure 3.1. The size of the usually disc-shaped samples lies in the range of 5 - 15 mm in diameter and 1 - 3 mm in thickness, while recently developed larger devices allow sample dimensions up to 40 mm in diameter and 10 mm in thickness. Between two dies or anvils made of high strength tool steel a sample, somewhat larger than the tools cavities, is compressed by up to 10GPa. One die is kept still while the other one is rotated around the axis along which the force is applied. Slippage depends on the material [11] but can be avoided by surface treating the cavities such as sand-blasting or nitriding. By comparison of markings on the upper and lower surface of the specimen before and after deformation the occurrence of slip can be easily estimated. During deformation the excess material flows out of the cavity, forming a burr in the gap between the anvils that prevents direct contact between the upper and lower tool. More recent experiments

also use ring-shaped geometries. Deformation happens by simple monotonic shear and can therefore be compared with route A ECAP processing. HPT also offers the opportunity to perform experiments with cyclic deformation by reversal of rotation.

The shear γ the sample experiences, outlined in figure 3.2, can be calculated according to equation 3.1, where u is the number of rotations, t is the thickness of the sample and r is the distance from the center.

$$\gamma = \frac{2\pi \cdot u}{t} \cdot r \tag{3.1}$$

Assuming a v. Mises yield locus the equivalent strain ϵ_v is given by:

$$\epsilon_v = \frac{\gamma}{\sqrt{3}} \tag{3.2}$$

Common directions for observation of the microstructure are shown in figure 3.2 and defined as axial, radial and tangential directions.

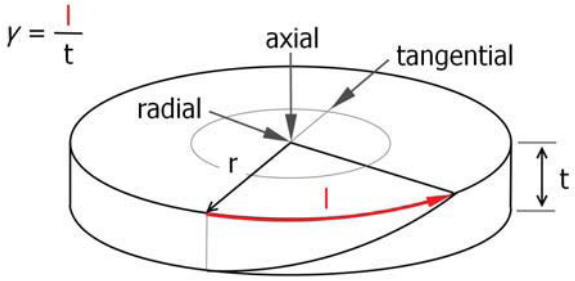

Figure 3.2.: *Schematic of the shear and directions of observation in an HPT sample.*

There is usually no problem to apply almost unlimited strain to such a sample but common experiments are conducted in the range up to 100. The gradient in strain and strain rate as a function of the radius offers the opportunity to observe a kind of deformation spectrum on one sample, but makes it hard to derive specific values from the applied torque during deformation, especially for strain rate sensitive materials.

The aim is to produce dense (non-porous) ultra-fine-grained materials in which the average grain dimensions approach the nanocrystalline regime[2]. Such materials have extraordinary properties. The remarkable increase in yield strength, sometimes paired with increasing ductility, is of special interest for future light-weight applications as well as for super-plastic shape forming.

The mechanisms of work-hardening and structural refinement during plastic deformation up to strain of about 1 - 2, have been intensively studied and are well described. In single-phase SPD materials deformed to very high strains (5 - 50) a saturation in refinement as well as a steady state in measured torque was observed. The most important parameters controlling structural refinement in saturation are alloying, temperature and the strain path[4]. The granular microstructure in the saturation regime mainly consists of high angle grain boundaries with average grain dimensions in the sub micron, often below 100nm, range.

Unfortunately the UFG structures are thermally not very stable. Recovery may start immediately after unloading the sample after deformation. One goal is to find ways to inhibit movement of grain boundaries by introducing dispersion to prevent recovery and increase the thermal stability. In SPD metal-matrix composite materials, produced by HPT powder consolidation, it was found that by powder treatment (and addition of dispersions), structural refinement as well as stability can be enhanced[5].

3.2. SPD of Aluminum and Aluminum Alloys

3.2.1. Pure Aluminum

HPT experiments on 99.99% purity level aluminum, performed at room temperature up to an equivalent strain of about 20, showed a deformation behavior that can be divided into three stages. In the first stage, for deformation up to an equivalent strain of 2, the material shows an increase in hardness that is related to rising dislocation density by generation and accumulation of dislocations to sub-grain boundaries. The second stage, for further deformation up to an equivalent strain of 6, is characterised by a decrease in hardness because dislocations annihilate at sub-grain boundaries, increasing the misorientation angle. The higher the misorientation, the more likely dislocations are to be absorbed. As a consequence, the dislocation density decreases while more high angle grain boundaries are formed. The third stage for strains >6 is characterised by a constant hardness, when generation and absorption of dislocations are in balance and the microstructure consists of high-angle grain boundaries[12]. Due to this dynamic recovery process at high strains, facilitated by the high stacking fault energy of pure aluminum providing easy cross slip of dislocations, hardness in the little deformed central region of an HPT-processed disc is higher than in the highly deformed outer region[13].

This effect was not observed in commercial purity (99.7%) aluminium, which clearly shows a saturation hardness in the outer highly deformed region of an HPT disc, which is much higher than for high purity aluminum. The hardness in the center stays initially lower and reaches the saturation level for very high total imposed strain. The saturation microstructure consists of high angle grain boundaries with a grain size of about 1 μm[14].

3.2.2. Aluminum Alloys

HPT deformation of supersaturated solid solutions of binary Al-Zn and Al-Mg alloys lead to grain structures below 100 nm, at which the Zn-rich solid solution decomposed completely, corresponding to the equilibrium at room temperature. A similar process was observed in the Mg-rich alloy, but was less pronounced due to the difference in equilibration kinetics. Grain boundary diffusion accelerated by fluxes of vacancies produced by SPD and sweeping of Zn and Mg atoms by moving grain boundaries are considered as the most probable

mechanism to obtain the equilibrium.[15].

The influence of deformation temperature and strain rate on the torque during deformation as well as the occurring microstructure and micro-texture was investigated on an Al-1wt%Mg and an Al-3wt%Mg alloy. HPT deformation experiments were performed for homologous temperatures from 0.1 to 0.8 and varying rotational speed between 0.05 and 0.5 rpm. Generally with increasing temperature the steady state level of the in situ torque decreases and is reached faster. The strain rate showed no influence at low temperatures while at high temperatures a distinct strain rate sensitivity was observed. In any case a saturation in structural refinement occurred. The structural size increases with temperature, and decreases with increasing Mg content. At higher temperatures the in situ torque rises with increasing strain rate, showing futher refinement during faster deformation. Microtextural investigations after 200 °C HPT processing showed a typical shear texture, getting more pronounced at 300°C deformation where the (111) glide plane is parallel to the torsional axis, and the [011] glide direction is aligned parallel to the shear direction. At 450°C the texture changes from the (111) to the (112) plane. Although there is a certain strain-rate sensitivity above $\approx$ 100 °C, the temperature and alloying are the major parameters influencing the onset of the steady state and the structural refinement. A process similar to dynamic recrystallisation is considered to be the reason for a steady state at high homologous deformation temperatures, while at low homologous temperatures the maintainance of steady state is facilitated by stress- and strain-induced boundary migration[16].

The deformation behavior of Al-Cu alloys was already studied by route A ECAP up to equivalent strains of $\approx$ 8. A supersaturated solid solution of an Al-1.7at%Cu alloy showed equiaxed grains of about 100 nm in size, separated by high angle grain boundaries. During deformation of the same alloy, heat treated to an $\alpha + \theta$' two phase microstructure, fragmentation and dissoluition of the θ' precipitates possibly forming a supersaturated solid solution, was observed by TEM and EF-TEM. Since plastic deformation occurs at θ' particles prior to grain refinement, eight ECAP passes lead to a larger average grain size in the two-phase material. During subsequent aging of the ECAP-processed single phase material, the precursor metastable phases (GP zones, θ", θ') are skipped, and only the equilibrium θ phase nucleates at grain boundarties[17].

ECAP deformation of a Al-4wt%Cu alloy, furnace cooled after homognization at 530 °C to obtain a two phase microstructure with large θ particles at grain boundaries, showed severe grain elongation and macroscopic shear patterns followed by internal fragmentation of the elongated grains by mainly low angle grain boundaries, while the misorientation increases with further deformation. The large Al_2Cu particles were fractured and aligned to the observed shear patterns[18].

Investigation of the mechanical properties of an age-hardening Al-Ag alloy, aged after cold rolling or ECAP processing, showed the potential of achieving strain hardening, remarkable uniform strain, high strength and good ductility. The same approach may be equally effective in other precipitation hardening alloys[19].

A recent work on an Al-4wt%Cu alloy also showed that enhanced stregth and reasonable ductility can be achieved by ECAP processing. Furthermore the phenomenon of work hardening was observed to decrease with decreasing size of grains and sub grains due to smaller distances between boundaries. The effect of work hardening was found to depend on the grain boundary structure, since dislocations are absorbed more easily at more highly misoriented boundaries[18].

3.3. HPT Equipment

3.3.1. Heating and Cooling System

The HPT equipment used for this work is schematically depicted in figure 3.3, which on the right hand side shows the setup for high temperature deformation and on the left hand side for deformation in liquid nitrogen. For high temperature deformation the anvils where heated by induction heating. For low temperature

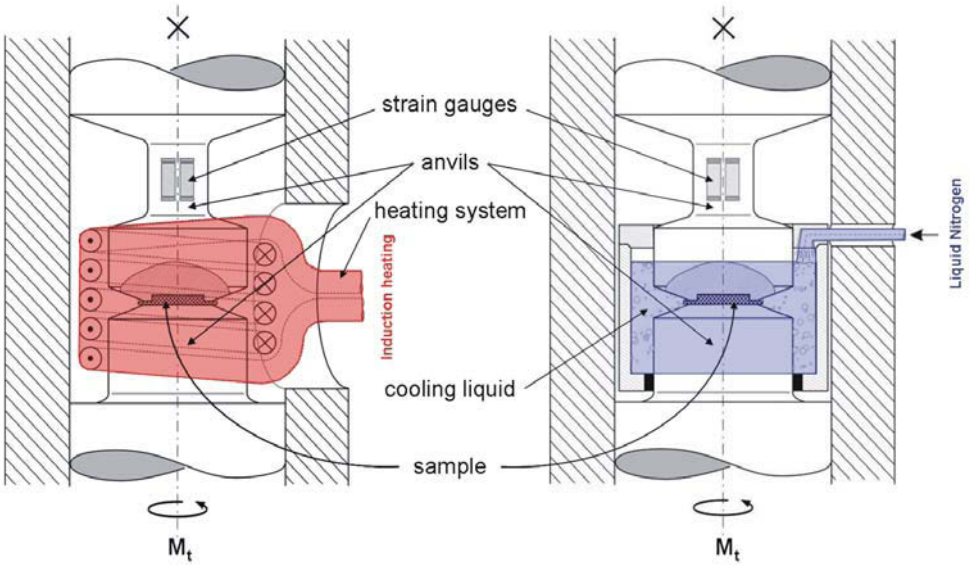

Figure 3.3.: *Schematic illustration of the HPT equipment used, which permits SPD deformation at temperatures between -196 and 500° C, variation of pressure, variation of rotation velocity and the direct measurement of the applied torque.*

deformation a container was fixed tight on the lower anvil, exceeding the sample level in height and filled with liquid nitrogen. The flow of liquid nitrogen during deformation was adjusted so that the container just spilled over slightly. To deform at 100 °C, the control of temperature for the induction heating was performed with a Ni/CrNi thermocouple, spot welded on the upper stationary anvil as illustrated in figure 3.4(a), since the effective range of the provided pyrometer is limited to temperatures above 160°C. For the 200°C experiments the temperature was controlled by the pyrometer focused on the lower anvil through one gap in the induction coil as shown in figure 3.4(b). The thermocouple was still used to compare the temperatures of the upper and lower anvil. The strain-gauge was cooled by pressurized air. The tempera-

ture on the upper anvil was found to depend on the air flow via the cooling system. Hence for deformation at 200°C, after the sample was pressurized and the lower anvil heated to constant temperature, the air flow was adjusted to equal temperature on both anvils and the specimen held for 2 minutes to heat through the anvils before starting rotation. Since there was no possibility of comparing anvil temperatures in the 100°C experiments, the air flow was set similarly to the 200°C adjustment.

(a) (b)

Figure 3.4.: *Illustration of temperature control of the HPT experiment. (a) Thermocouple on HPT anvil with a sample loaded. (b) HPT equipment with induction heating system. The pyrometer is focused on the red laser spot in the gab in the induction coil.*

3.3.2. HPT Anvils

For the HPT experiment in this study, anvils as sketched in figure 3.5 were used. The special shape of the anvils cavities, sketched in figure 3.5(a), was chosen primarily to have more material for preparation of TEM samples in radial view. A comparison of the sample-geometry with the standard calculated equivalent von Mises strain, is illustrated in figure 3.5(b). The strain increases linearly with radius r for constant thickness t. From the shoulder at r= 4.5 mm the shearing rises additionally with the reduction of the thickness, theoretically towards infinity at the tip.

In the majority of cases the recorded torque evolutions did not show a clear steady state regime. So the material was assumed to be near saturation in the area around r≈ 4.5 mm, if the hardness was comparably to the values measured in the narrowing part. To test whether the linear increase in strain is reflected by the measured micro-hardness, for comparison samples were deformed for 1.1 and 3.5 revolutions, corresponding to ϵ_v of ≈10 and ≈30 at r= 4.5 mm.

The cavities get slightly larger, due to frequent sand-blasting, so the actual strain for 3.5 revolutions at r= 4.5 mm varies from ≈32 for the first to ≈29 for the last experiments. The rotational speed varies a little with the material condition being deformed. To simplify illustration and comparison of the data, the recorded torque vs. time curves were normalized to an equivalent strain of 32 at r= 4.5 mm for 3.5 turns.

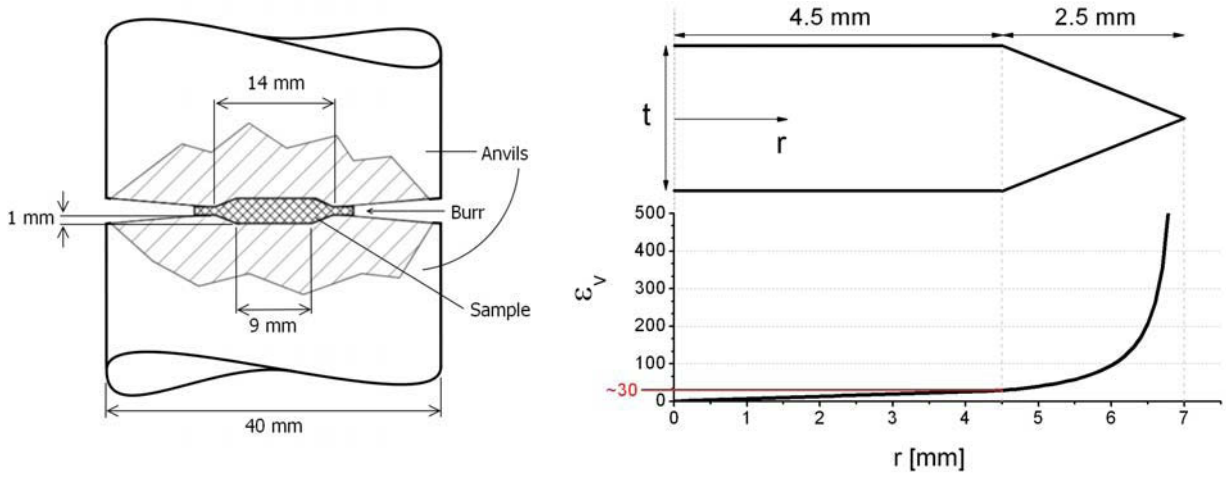

(a) (b)

Figure 3.5.: *(a) Sketch of the closed anvils used with a sample loaded. (b) Schematic cross section of an HPT sample with the corresponding strain vs. radius plot. The strain was calculated for 3.5 revolutions using equations 3.1 and 3.2.*

3.4. Sample Production and Preparation

The making of discs for the HPT experiment is illustrated in figure 3.6. Bars of the homogenized material were compressed with ≈2 GPa into cylinders of 14 mm in diameter, using the tool depicted in figure 3.6(a). Slices of ≈2 mm in thickness were cut off with a *Struers Secotom* and pre-shaped between the HPT-dies at 2 GPa without rotation.

(a) (b)

Figure 3.6.: *(a) Tool for compression of bars to cylinders. (b) Production steps of samples for HPT experiments. From left to right: cuboid of homogenized material → compressed to a cylinder → cut into slices → pre-shaped with HPT dies; 1 €-cent ∅ 16.25 mm.*

With applied pressure the excess sample material forms a burr in the gap between the anvils and there remains only a little space for the thermocouple. For the high temperature experiments the margins on the pre-shaped discs were ground off. So during processing the burr stayed small enough not to touch the induction coil or detach the thermocouple, as illustrated in figure 3.7 for comparison with figure 3.4. Finally the specimens were heat-treated to the conditions defined in Section 2.6.

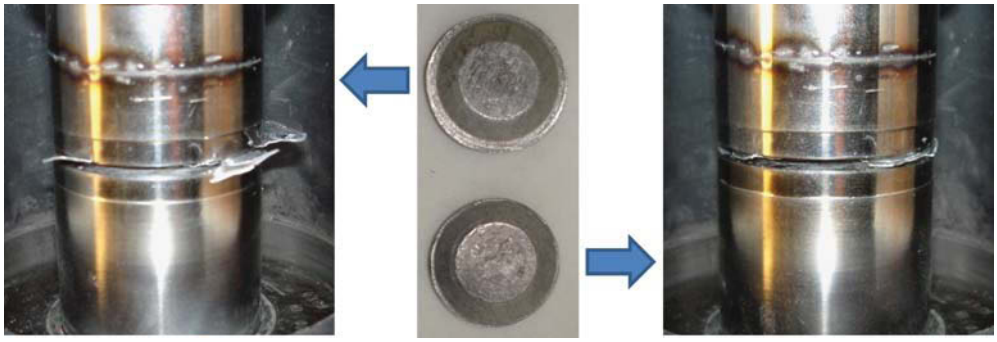

Figure 3.7.: *Comparison of the burr formed during 3.5 rotations for samples without and with margins ground off after pre-shaping.*

3.4.1. HPT Deformation

Most of the samples were processed for 3.5 turns at a pressure of 2.1 GPa at RT, 100°C and 200°C with a rotational speed of 0.2 revolutions per minute, using the equipment described in Section 3.3. For the pretests, of each typical condition one samples was deformed for 1.1 revolutions at RT. A simple strain-rate-jump test was performed with an S sample at RT, by switching the rotational speed during deformation from the lowest to the highest level, allowed by the equipment. Only two solution-treated samples were deformed in liquid nitrogen to get an idea of what happens at very low temperatures.

Because of the low speed of rotation the heat generated by deformation was presumed to have no significant influence. Since aluminum is very soft no slippage was observed. The burr formed in the gap between the anvils, as shown in figure 3.7, is very thin and breaks off easily during the RT and 100°C HPT processing. At 200°C deformation the excess material curled between the anvils and was smeared around the seam of the cavities and the anvil surface. The anvils were stuck together after unloading and it was hard to separate the deformed specimen from the tools. For comparison, figure 3.8 shows an anvil after deforming some samples at 200°C and a relatively new anvil that was only used at RT. To prevent recovery after deformation, the specimens were stored as far as possible in a fridge.

Figure 3.8.: *Anvil surface after deforming some samples at 200°C (left) compared with a recently machined anvil only used for RT deformation (right).*

3.4.2. Aging of HPT deformed samples

For the aging experiments, HPT deformed specimens were sectioned as depicted in figure 3.9 using the wire saw shown in figure 3.10(a). In the same way the artificial aging characteristic of the undeformed material was determined, the sections were aged in drying oven at 190°. With forceps the specimens were taken out of the oven and individually placed directly into small paper envelopes and allowed to cool off to room temperature. Although after aging (annealing), no more structural changes should occur at room temperature, the samples were also stored in a fridge. For the first pretests, deformed specimen were sectioned into six equal segments. For the further experiments the HPT processed discs were divided into eight pieces.

Figure 3.9.: *HPT deformed samples: as deformed (left) and one sectioned to be aged (right).*

3.4.3. Preparation for Microhardness Measurements

With a wire saw using 0.3 mm diameter diamond wire, the HPT processed samples were halved, as shown in figure 3.10(a). To keep the sections as cool as possible for the time of preparation and investigations, the samples were clamped in an aluminum sample holder, as depicted in figure 3.10(b). Proceeding as described in section 2.3.2, specimens and holder were ground and polished until a mirror-like surface was obtained.

(a) (b)

Figure 3.10.: *HPT deformed sample during cutting by diamond-wire saw(a). Sections clamped in an aluminum sample holder for grinding and polishing(b).*

3.4.4. Microhardness Measurements

Micro-hardness was measured with the equipment and the same parameters as described in Section 2.3. On all as-deformed samples, indents were made along the center line of a radial cross section at intervals of 0.5 mm, as represented by the thick crosses in figure 3.11. To check the homogeneity of deformation, on some samples a grid of indents was placed as represented by the thin crosses in figure 3.11.

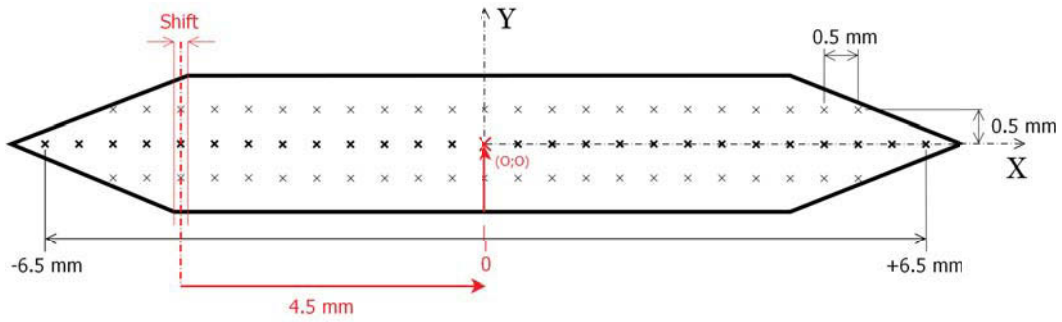

Figure 3.11.: *Schematic representation of micro-hardness indents grid on a HPT deformed sample in radial view.*

Since the HPT anvils are not perfectly aligned, the top and bottom of any deformed sample are slightly shifted, hardly visible to the naked eye but obvious in the light microscope. For better comparability of the hardness values, a sample based coordinate system was defined by the following procedure. The sample was aligned parallel to the X movement direction of the stage. As illustrated in figure 3.11, the center was defined as the point 4.5 mm in from the average of the shoulders position, at half of the thickness. Since the shift of the anvils was 0.3 mm at most and the edges could not be distinguished exactly, the real and estimated centers should lie within ± 0.5 mm. In the X direction, representing the sample radius, indents were made in the range of -6.5 ≤ X ≤ 6.5 mm at Y = 0 and between -5.5 ≤ X ≤ 5.5 mm at Y = ±0.5 mm.

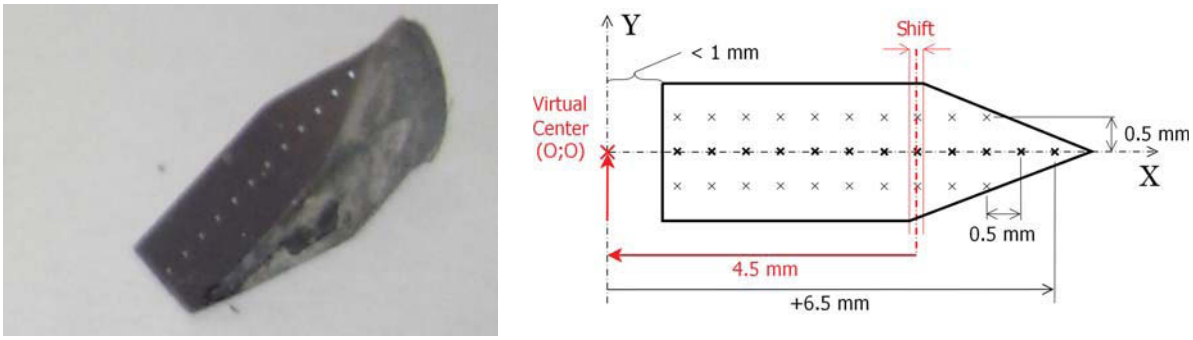

(a) (b)

Figure 3.12.: *(a) Polished section of an HPT deformed sample. (b) Schematic representation of micro-hardness indent grid. Distances were measured from a virtual center. Not more than 1 mm was cut and ground off with preparing.*

The aged sections were polished on one face and hardness indents were also made along the radius in the center as shown in figure 3.12(a). Since the real center of the sample is lost by cutting and grinding (but no more than 1 mm), indents were placed with respect to a virtual center as sketched in figure 3.12(b). One set of RT deformed S samples was aged together with B samples of the raw material at 180°C (instead of 190°C) by mistake. On these specimens, to get an impression of the overall hardness evolution, a grid of indents was measured as shown in figure 3.12(b). All other aged HPT samples were measured along the center line only.

3.4.5. SEM Sample Preparation

From HPT deformed discs, samples for SEM investigation were sectioned by diamond wire saw in radial and tangential view, as shown in figure 3.13 on the left. The slices so obtained were clamped in an aluminum holder for grinding and polishing (as described in Section 2.3.2) of the faces depicted in figure 3.13 on the right.

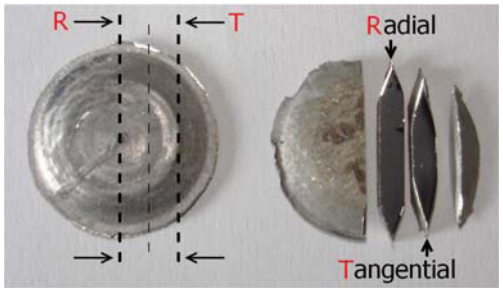

Figure 3.13.: *Illustration of samples from HPT deformed discs used for SEM investigations.*

To get rid of the deformation layer formed during polishing, subsequent electropolishing was performed with a *Struers LectroPol-5* using an *Struers A2* standard electrolyte, but this did not lead to any satisfactory results. Instead, samples and holder were additional polished with a *Minimet* using *Masterprep* 0.03 μm colloidal silica suspension on *Mastertex* polishing sheet until almost no structure and artifacts were visible in the light microscope at the highest magnification. It was found that a polishing time of one hour, reducing downforce every 20 minutes in steps of 5 from 15 to 5 N, led to comparable results for various material conditions. On surfaces so prepared, the deformed micro structure was partly visible in the SEM, but also many artifacts and a layer from polishing. The grain structure was only visible by using the QBSD detector, the largest aperture, slow scan speed and accelerating voltages above $\approx$15kV. Because of the low atomic number and density of aluminum the interaction volume with electrons is very large. Paired with the fast contamination with hydrocarbons under electron bombardment and the resulting drift, the images recorded with the QBSD detector (which needs at least 10kV electrons, high noise reduction and slow scan speed to get good contrast) appear blurred, especially above 10kx magnification. Using the more sensitive Inlens

detector (that detects backscattered (BSE) and secondary electrons (SE)) on only mechanically polished surfaces, the SE signal from the deformation layer exceeds the BSE signal. The deformation layer was removed by subsequent ion milling of the colloidal silica polished samples in a *BAL-TEC Res 100* for about 10 minutes, using 5 kV Ar-ions under an incident angle of 10° and a current of 2 mA. So image quality was improved, also at low accelerating voltages using the InLens detector. Since the ion milling device is exclusively used for preparation of TEM specimens and needs modifications to sputter other sample geometries, only a few SEM specimens were finally ion milled.

3.4.6. TEM Sample Preparation

Standard TEM foils were prepared from HPT samples, as sketched in figure 3.14. Deformed discs were ground and polished evenly from both sides to a thickness of 0.1 mm. Circular disks, 3 mm in diameter, were punched out with their midpoint in a distance of about 4.5 mm from the center as illustrated in figure 3.14. Of the raw material TEM samples were produced by the same procedure from undeformed pre-shaped discs, after heat-treatment to the three typical conditions. To obtain electron transparency the punched discs were ground, polished and electrolytically thinned with a *Struers Tenupol-5* using *Struers A2* electrolyte cooled to ≈ -20°C. The foils were investigated in a *Philips CM12* transmission electron microscope, equipped with a CCD camera for digital imaging, and an EDX system for chemical analysis.

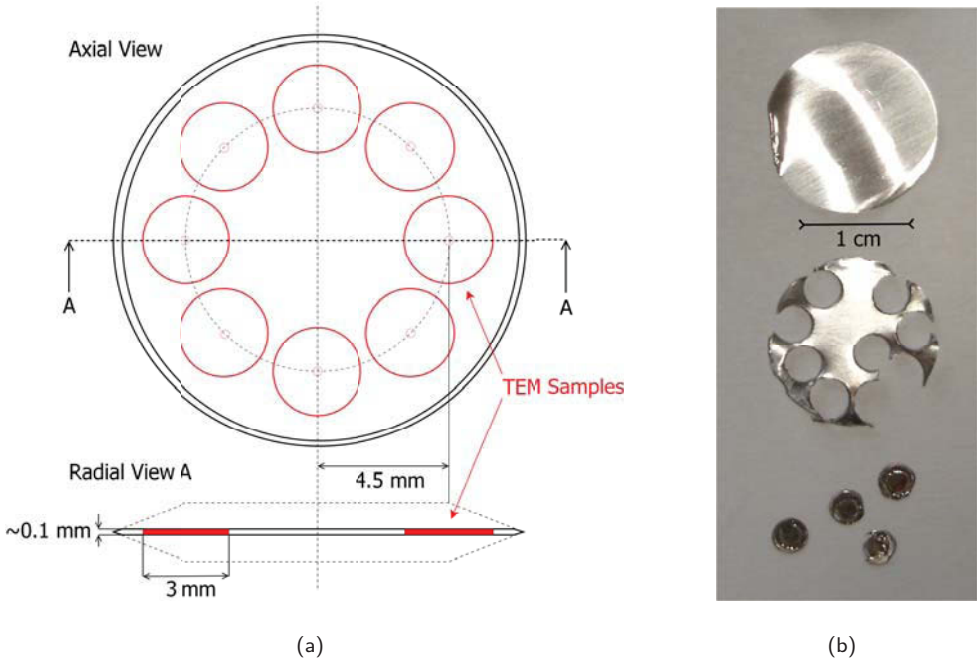

Figure 3.14.: *Schematic representation of TEM samples prepared in axial view from a HPT disc(a). Illustration of the preparation steps(b).*

Chapter 4.

HPT Pretests

4.1. Pretests HPT Deformation

The first HPT experiments may be seen as pretests, to get experience with the technical equipment and an impression of the materials behavior. Disks, produced as outlined in section 3.4, were solution treated and subsequently aged at 190°C as described in section 2.3. Because the difficulties associated with high temperature deformation were not known at this time the samples were not pre-shaped. The influence of plastic deformation by compression before rotation was considered to bee small. Specimens, artificially aged for 72h and 144h, were assumed to be peak-aged and over-aged respectively, according to the aging characteristic determined for A samples (Sections 2.3 and 2.4). Of each material condition specimens were deformed at room temperature for 1.1 and 3.5 revolutions, that represents an equivalent strain of ≈10 and ≈30 at radius r = 4.5 mm. To see if deformation occurs homogeneously over the thickness of the specimens, the hardness was measured in a grid of indents as described in Section 3.4.4. If the linearly increase of strain with the distance from the center is fulfilled for the high degree of deformation can be easily estimated: The hardness values at r = 4.5 mm after 1.1 turns and at r = 1.5 mm after 3.5 turns, should be of comparable order of magnitude.

4.1.1. Solution-treated Samples

The resulting hardness of a solution-treated sample after HPT deformation for 1.1 revolutions, depicted in figure 4.1(a), clearly shows a linear rise with increasing distance from the center and seems to be evenly distributed over the thickness. The hardness values after deformation for 3.5 revolutions are scattered over the thickness and asymmetrical about the center, illustrated in figure 4.1(b). It appears that deformation was localized to the top region at Y = 0.5 mm, where hardness seems to level off at around 200HV, represented by the green curve in figure 4.1(b). The lower black curve in figure 4.1(b) shows a similar profile to the 1.1 rev. deformed sample, indicating less deformation.

The claim for equal hardness at equal strain, at least on the right halve in figure 4.1(c), seems to be well fulfilled. The torsional moment recorded during deformation, depicted in figure 4.1(d), runs through a peak at about 0.6 rev. in both cases. The plateau between 1.1 and 2 rev. is followed by a significant decrease. The reasons for the abnormal deflection in the black graph at the beginning of the rotation and for the inhomogeneous deformation could not be determined.

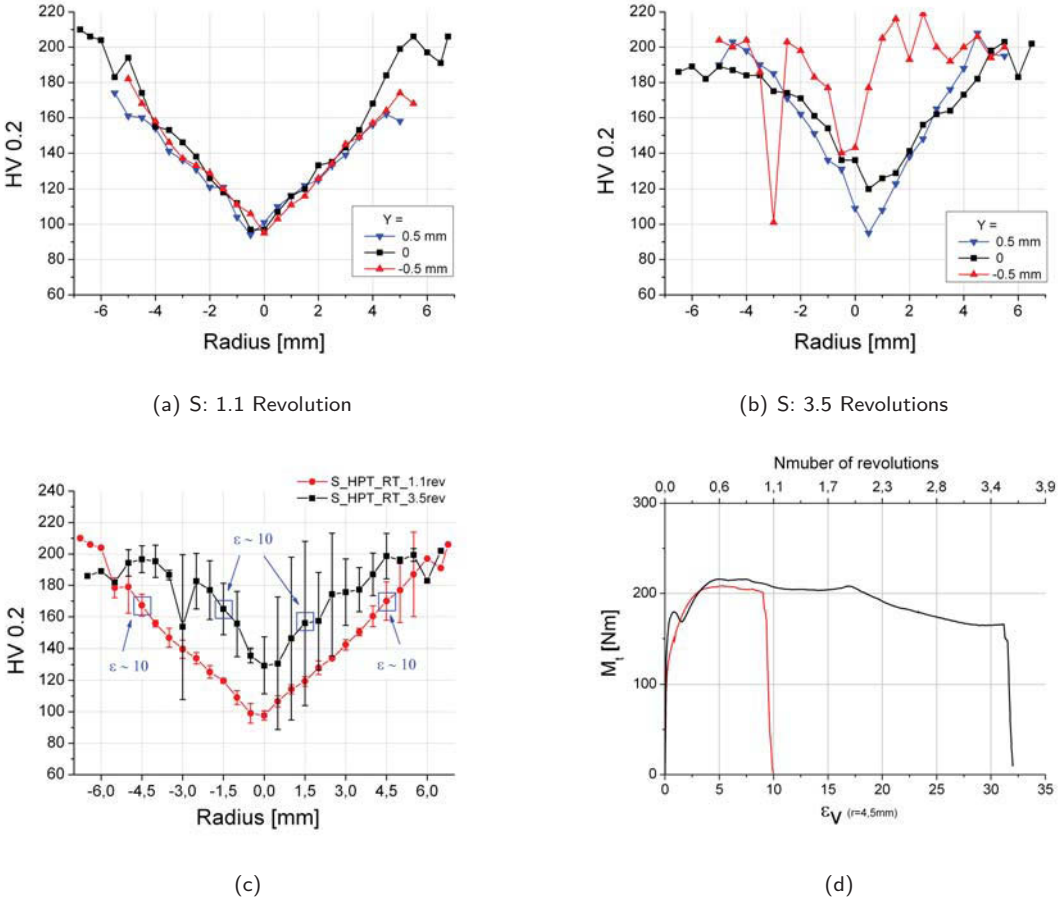

(a) S: 1.1 Revolution

(b) S: 3.5 Revolutions

(c)

(d)

Figure 4.1.: *Hardness distribution on the radial cross section, as described in section 2.3, of solution treated samples deformed at room temperature for (a) 1.1 and (b) 3.5 revolutions. Comparison of the mean hardness values(c). Torque measured during HPT deformation of solution-treated samples(d).*

4.1.2. Peak-aged Samples

On the peak-aged sample deformation appears more even over the thickness, illustrated in figure 4.2. Deformation becomes more inhomogeneous with increasing strain, as indicated by the shift in hardness between top and bottom at ± 4 mm in figure 4.2(a) and the asymmetrical evolution relative to the center in figure 4.2(b). Mean hardness at points of theoretically equal strain on little and highly-deformed samples, as illustrated in figure 4.2(c), differs much more than for the solution-treated condition in figure 4.1(c).

Hardness seems to approach a saturation level with increasing degree of deformation. For both S and PA conditions, the measured torque appears almost equal up to an equivalent strain of about 2. At higher degrees of deformation, the peak-aged sample does not show a significant drop but seems to level off somewhat below 200 Nm.

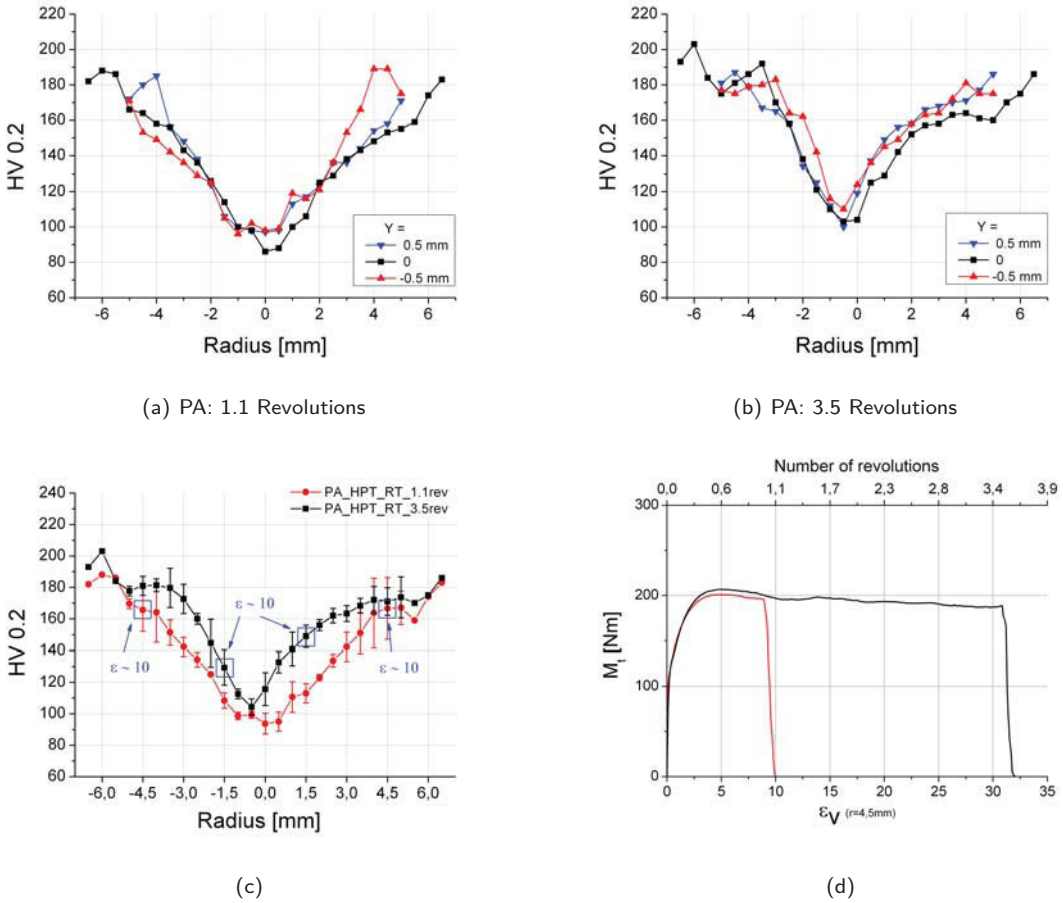

(a) PA: 1.1 Revolutions

(b) PA: 3.5 Revolutions

(c)

(d)

Figure 4.2.: *Hardness distribution on the radial cross section of peak-aged samples, deformed at room temperature for (a) 1.1 and (b) 3.5 revolutions. (c) Comparison of the mean hardness values. (d) Torque measured during HPT deformation of peak-aged samples.*

4.1.3. Over-aged Samples

Similar to the solution-treated and peak-aged condition the little deformed over-aged sample shows very homogeneous deformation behavior, but also seems to deform inhomogeneously at higher degrees of deformation, as figure 4.3 reveals. Symmetry relative to the center after 3.5 revolutions is slightly better pronounced than for the PA sample. Equal hardness at equal strain is shown at least on the right hand side in figure 4.3(c). The measured torque fits almost perfectly for both samples, except some unexplainable deviation at the beginning, depicted in figure 4.3(d). In general a similar torque level as at the S and PA

material conditions is reached after ≈0.6 revolutions. The over-aged sample showed no peak, but a small decrease after about 2.5 turns.

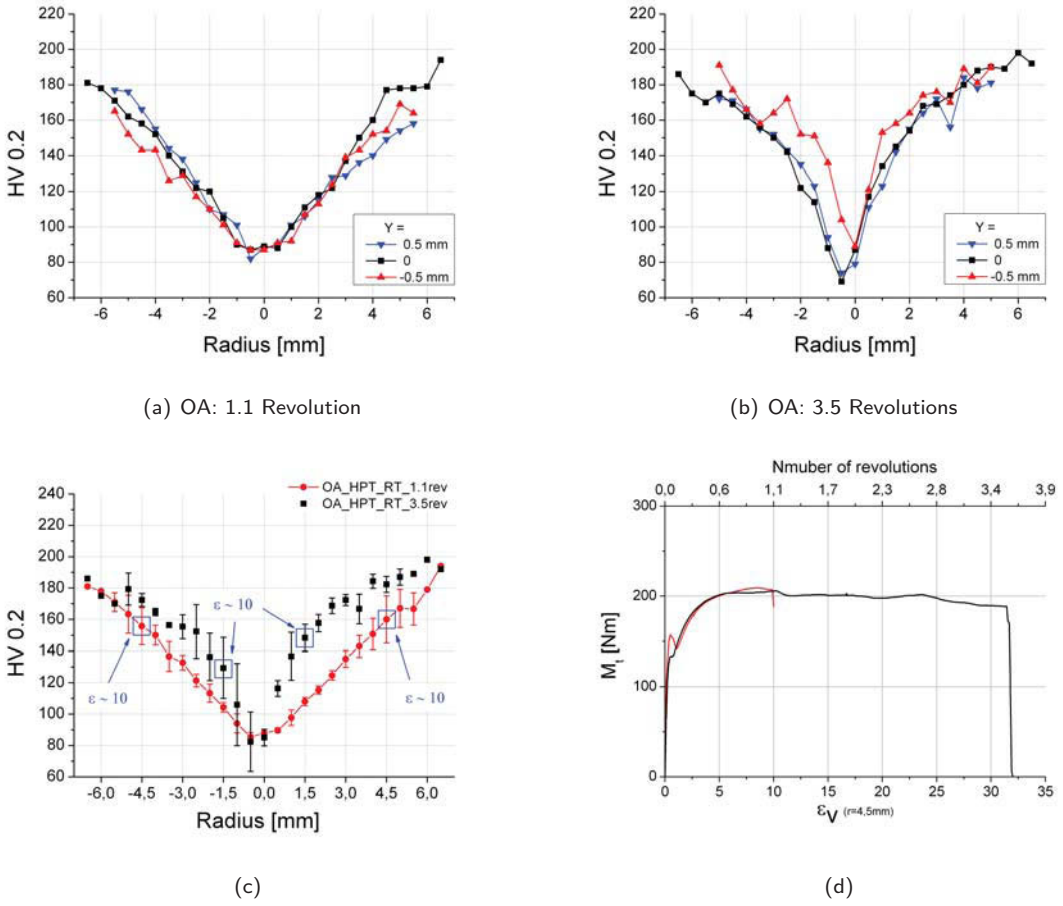

(a) OA: 1.1 Revolution

(b) OA: 3.5 Revolutions

(c)

(d)

Figure 4.3.: *Hardness distribution on the radial cross section of over-aged samples deformed at room temperature for (a) 1.1 and (b) 3.5 revolutions. (c)Comparison of the hardness in mean. (d) Torque measured during HPT deformation of over-aged samples.*

4.1.4. HPT Pretests Summary

There seems to be no great difference in the deformation behavior of the various material conditions up to an equivalent strain of about 10. The evolution of hardness on samples processed for 1.1 rotations is quite homogeneous. The values lie somewhat over 80 HV in the center, slightly higher for the over-aged sample, and reach up to about 180 HV towards the edge at r≈ 4.5 mm. At higher strains, deformation seems to occur more inhomogeneous, indicated by a loss of symmetry relative to the center and the variation of hardness versus the thickness direction on the samples processed for 3.5 turns. It appears that with further aging time the material deforms more evenly. Although hardness is scattered over thickness, the mean hardness is in good agreement with the hardness values along the center line, as shown in figure 4.4.

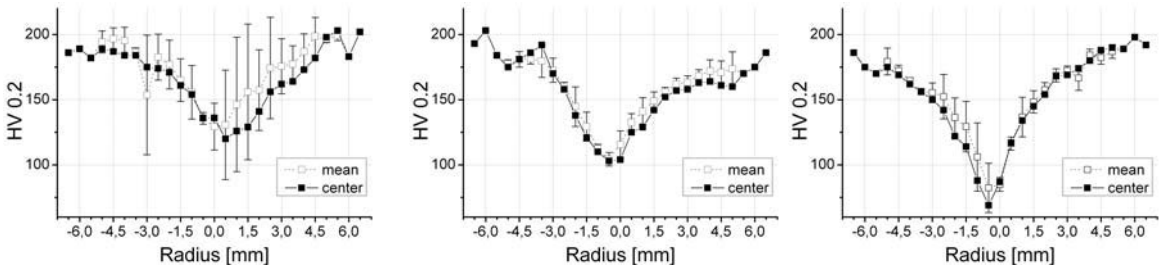

(a) Solution-treated (b) Peak-aged (c) Over-aged

Figure 4.4.: *Comparison of the mean hardness and hardness in the center on (a) solution-treated, (b) peak-aged and (c)over-aged samples, HPT deformed for 3.5 revolutions at room temperature.*

Concerning the torque, no significant differences between S and PA samples was observed up to about 1 revolution, running through a peak at ≈0.6 turns, while at higher strain after about 2 rev. the solution-treated sample showed a significant decrease in torsional moment. The over-aged sample has no peak in torque evolution and seems to reach a steady state after about 1 revolution.

4.2. Pretests for Aging of HPT Deformed Samples

The first aging experiments using HPT deformed samples were by mistake conducted at 180°C instead of 190°C, and may therefore be seen as pretests to explain the principle of the experiment and the exposition of the results.

Disks of the raw material were solution treated and HPT deformed at room temperature for 3.5 revolutions at 2.1 GPa. Figure 4.5 shows the in-situ torque during deformation of samples for the aging pretests. To determine the aging characteristic, the two discs, corresponding to graphs P5 and P6 in figure 4.5 were used. Sectioning of each disc into six segments as even as possible, delivered twelve samples.

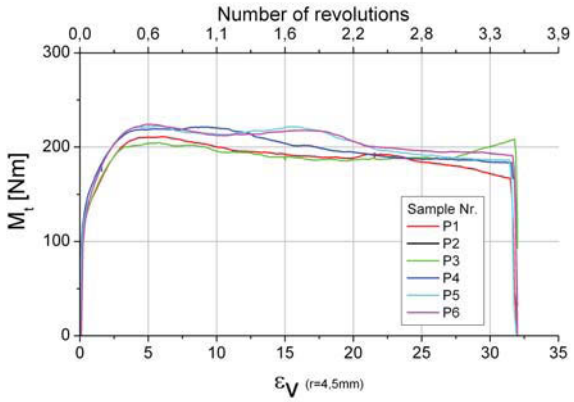

Figure 4.5.: *Torque during HPT deformation for 3.5 revolutions of various solution-treated samples. Specimens P5 and P6 were sectioned for subsequent aging.*

On one section the as-deformed hardness was measured, while the remaining elven were aged at 180°C. A grid of hardness indents was measured on each sample as described in Section 3.4.4 and illustrated in figure 3.12. The resulting hardness profiles for various selected aging times is depicted in figure 4.6. The as-deformed specimen (Fig. 4.6(a)) shows a distinctly inhomogeneous hardness distribution over thickness, as found in section 4.1.1, but the saturation level at 200 HV is clearly visible. Within the first minutes at

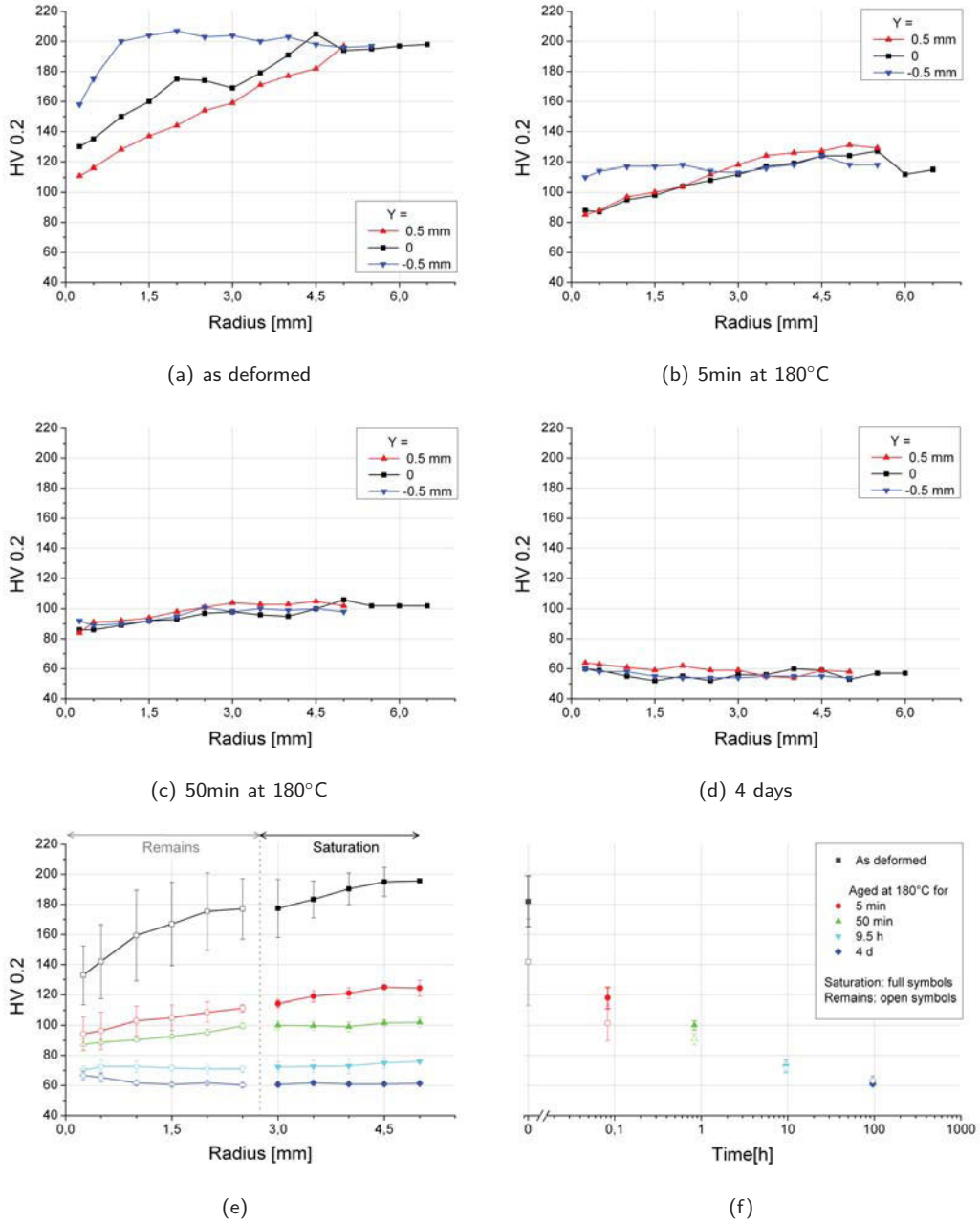

Figure 4.6.: *Comparison of the hardness profiles on S samples that were deformed for 3.5 revolutions at room temperature and subsequently aged at 180°C. (a) as deformed, (b) after 5 min, (c) after 50 min, (d) after 4 days. (e,f) Illustration of the construction of selected points for the characteristic hardness vs. time plot.*

the elevated typical aging temperature, the hardness drops very fast and becomes more even over thickness, as illustrated in figure 4.6(b). After 50 min (Fig. 4.6(c)), one can hardly distinguish between regions of higher and lower deformation. The summary of selected mean values in figure 4.6(d) shows that during further aging hardness gets more evenly distributed and decreases slowly.

The construction of the characteristic hardness vs. time plot for aged HPT-deformed material, as used to display the rest of the results, is illustrated in figure 4.6(e) and (f). The data of each sample was divided into a saturation regime for r≥3 mm and the remaining values towards the center. Mean values and standard deviation shown in figure 4.6(f) were calculated from the individual values measured in each region. Filled symbols represent the saturation regime, the open symbols the remaining data points.

The complete plot is illustrated in figure 4.7. For comparison, the aging characteristic of the undeformed raw material, measured on B samples as described in Section 2.3, was inserted, represented by the blue symbols. In the defined saturation regime the hardness drops constantly during the first hour, while during the same period of time in the remaining little deformed region (r≤3) the decrease in hardness appears less uniform. With further aging time the hardness gets distributed more even on each single specimen, but values are slightly scattered from sample to sample. After about 3 days at the typical aging temperature the hardness of the deformed material falls below the peak hardness of the undeformed material.

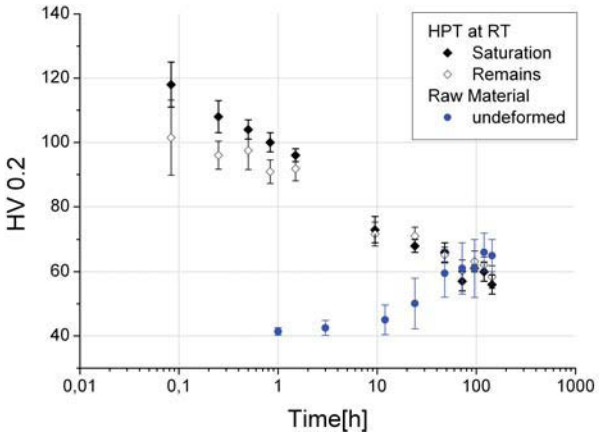

Figure 4.7.: *Aging characteristic determined from sections of S samples, HPT deformed at RT for 3.5 turns, compared with the the aging curve of the undeformed material, measured on B samples, for an aging temperature of 180° C.*

Chapter 5.

Results of HPT Deformation

5.1. Overview

For the HPT experiments, samples were produced as described in Section 3.4 and heat-treated to S, PA and OA condition, according to Table 2.1. The heat-treated samples were HPT deformed at various temperatures, for 3.5 revolutions at a pressure of 2.1GPa and a rotational speed of 0.2 rev/min. An overview of the conducted deformation tests, measurements and investigations is given in Table 5.1.

Table 5.1.: *Overview: HPT deformation experiments and the performed microstructural analyses*

		Material Condition		
		S	**PA**	**OA**
HPT at	**RT**	TM [1], MH [2], TEM [3], SEM [4]	TM, MH, SEM	TM, MH, SEM
	100°C	TM, MH	TM, MH	TM, MH
	200°C	TM, MH, SEM	TM, MH	TM, MH
	-196°C	TM, MH		

[1] Torsional Moment, [2] Microhardness, [3] TEM investigations, [4] SEM investigations

The results may either be sorted by material condition, or by deformation temperature. In this chapter the torque recorded during HPT processing at various temperatures and the resulting micro-hardness and some occurring microstructures will be described separately for each material condition. Further possible combinations and crosslinks will be drawn in the framework of the discussion. The first SEM micrographs derive from samples of the pretests, taken while trying to find a sufficient preparation method to bring the micro structure to light. TEM images of the undeformed raw material in the different typical conditions will be shown in this context.

5.2. Torque during HPT Deformation

In order to have enough material, for finding sufficient prepartion methods and to plan the scheduled experiments, many samples in S condition were deformed. With respect to cost and effort in PA and OA condition at most four specimens were deformed at each temperature. The figures in this section are composed of calculated mean curves as illustrated in Appendix C. Although there are peculiar deviations in the evolution of torque for the single specimens, the calculated means show the distinct differences and similarities. To point out some interesting phenomena the following descriptions will also refer to the associated figures in the appendix.

5.2.1. S Condition

The torque during deformation at various temperatures of samples in S condition is illustrated in figure 5.1. Except the magenta-colored graph for -196°C, which derives from one of only two samples deformed in liquid nitrogen, figure 5.1 is a summary of the mean curves in figure C.1 of Appendix C. At RT and 100°C

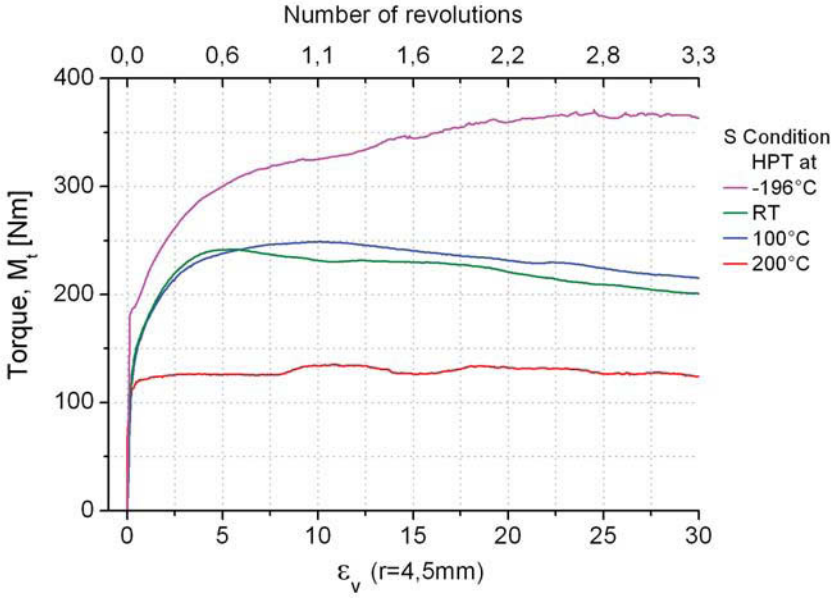

Figure 5.1.: *Comparison of in-situ torque during deformation of samples in S condition for 3.5 revolutions at 2.1GPa, at various temperatures.*

the evolution of the torsional moment appears very similar, showing a small peak and plateau, which is shifted to higher strains and less pronounced at 100°C relative to the RT graph, followed by a decrease to a level around 200 Nm in both cases. Strangely the torque at 100°C exceeds the RT values. Expectedly the torque during low-temperature deformation is significantly higher and may approach saturation slowly at about 350 Nm, while the distinctly lower torque at 200°C levels off immediately at about 100Nm.

5.2.2. PA Condition

The deformation behavior in the PA condition, illustrated in figure 5.2, appears similar to the S condition results. At RT and 100°C the torque evolution runs through a peak followed by a decrease to a level around 200 Nm. No clear plateau shows up at RT but is quite obvious at 100°C. Comparing individual RT graphs in figures C.2(a) and C.1(a) in the appendix show that a peak/plateau or only a peak is visible on S as well as on PA samples. During 200°C deformation, the torque levels off at about 125 Nm.

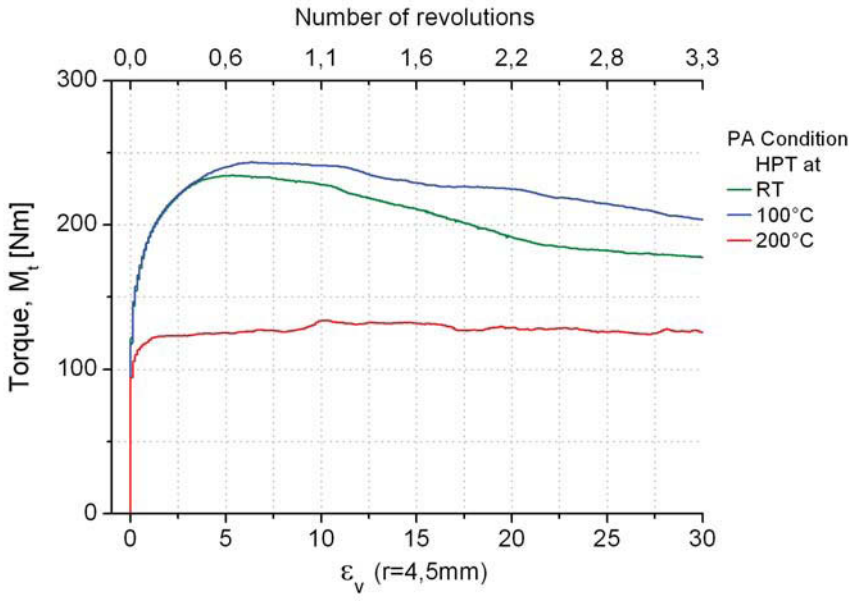

Figure 5.2.: *Comparison of in-situ torque during deformation of samples in PA condition for 3.5 revolutions at 2.1GPa, at various temperatures.*

5.2.3. OA Condition

The OA samples behave significantly different as figure 5.3 reveals. The recorded torsional moment appears very uniform, although measured on different samples, as depicted in figure C.3. As is common for single-phase fcc materials, the torque gets lower for higher deformation temperatures, and in this particular case reaches a steady state somewhat above 200 Nm for RT, slightly below 200 Nm for 100°C and around 100 Nm for 200°C deformation. Assuming that the uniform behavior at RT is also shown at higher temperatures, the deviations at 100°C and 200°C may not be caused by the material itself but by the equipment. Relative to the RT level the torque decreases about 25% for 100°C and 50% for 200°C.

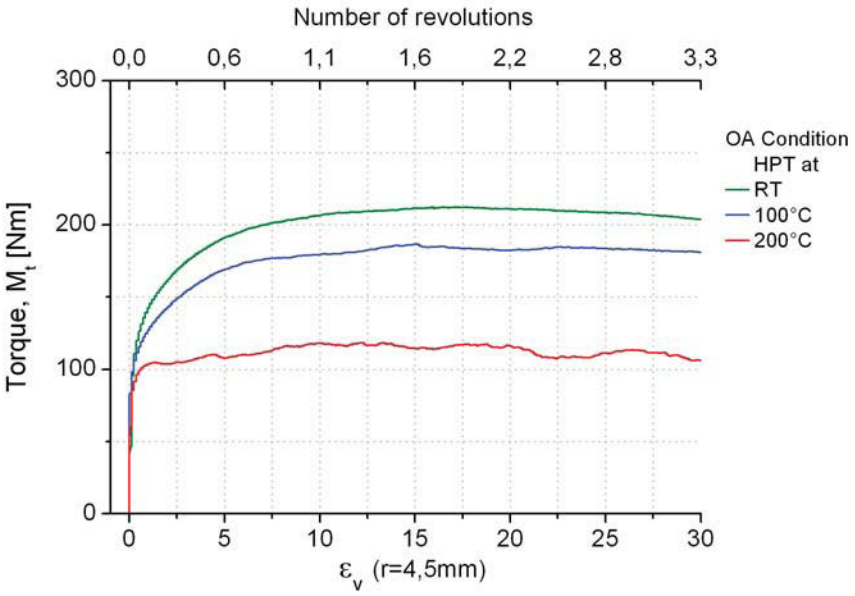

Figure 5.3.: *Comparison of in-situ torque during deformation of samples in OA condition for 3.5 revolutions at 2.1GPa, at various temperatures.*

5.2.4. Torque: Summary

For the S and PA condition the evolution of the torque during deformation at RT and 100°C appears very similar with a seamless transition between peak/plateau and peak characteristics. The deviations may be result of the inhomogeneous deformation behavior of the raw material or caused by the burr, disturbing the temperature control. For reasons described in section 3.3 at the higher processing temperatures the uncertainty of the HPT equipment may play a major role, especially for S specimens which were only partly pre-shaped before heat-treatment and deformation. At RT and 100°C the samples in OA condition show a distinctly different behavior that is similar to other fcc single-phase materials. Almost no difference in evolution of torque between the three material conditions was observed at 200°C. The torsional moment for the OA condition may be slightly lower than for S and PA material.

5.2.5. Strain-rate Sensitivity

A simple strain-rate-jump test was made with an S condition specimen at RT. After 4 revolutions (1200 seconds) at the typical 0.2 rev/min, the speed of rotation was switched during HPT processing between the upper and lower limit of 0.62 and 0.045 rev/min allowed by the equipment. The resulting torque evolution in figure 5.4(a) shows clearly the strain rate sensitivity of the material. A detailed view in figure 5.4(b) and (c) shows a jump in torque of about 25 Nm within 5 seconds when switching from low to high deformation speed and vice versa. The modulated oscillation is more likely caused by the drive system than an effect of the material, since the amplitude stays constant while frequency changes with rotational speed.

Generally the rise in torque, when switching from low to high rotation speed, is followed by a decrease, while conversely the drop in torsional moment jumping from fast to slow rotation slightly increases with further deformation. This effect may be caused by the heat arising from deformation, especially at the high rotation speed, by transition phenomena in the defect density at different strain rates and dynamic precipitation and re-dissolution processes.

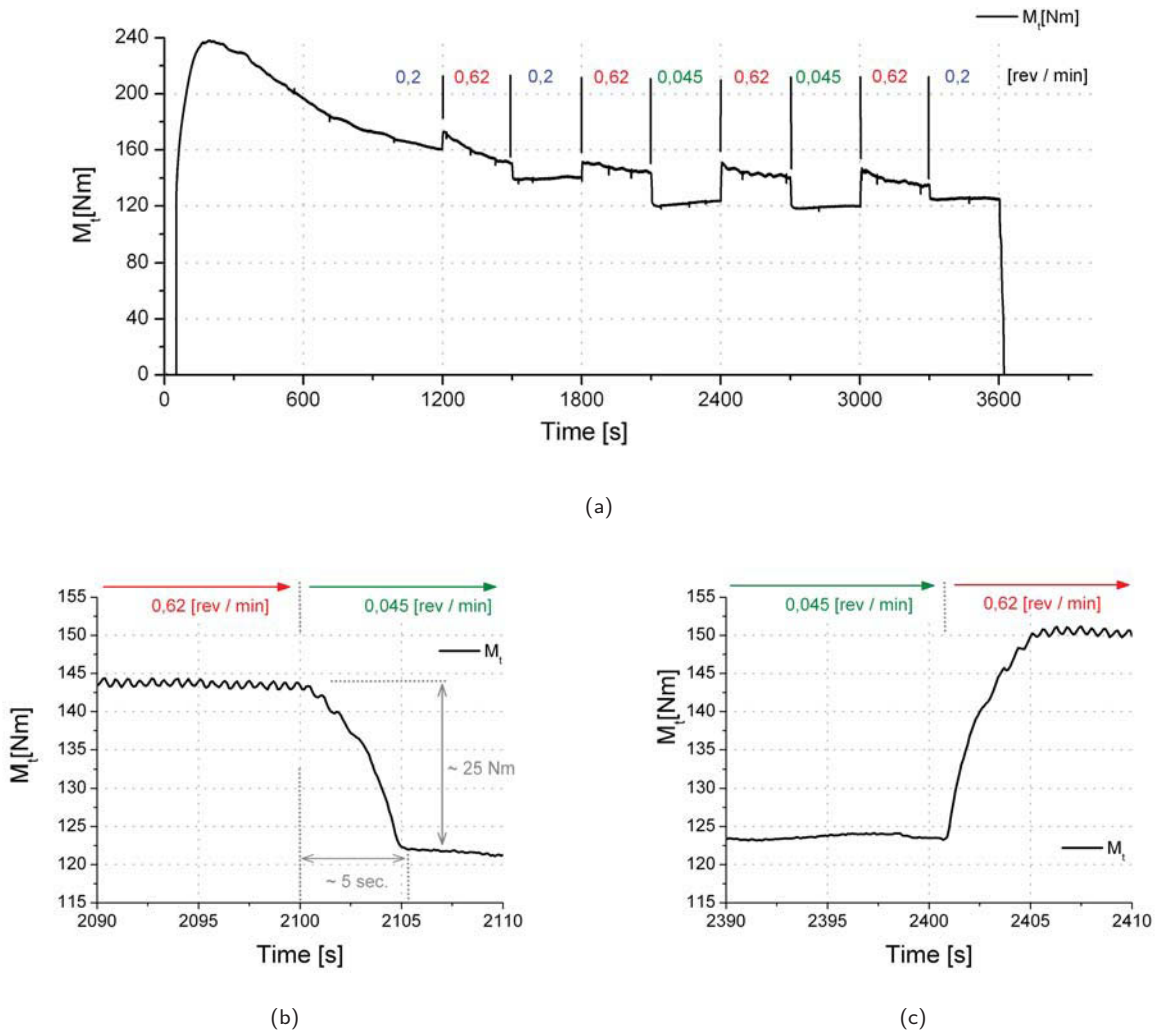

Figure 5.4.: *Illustration of the strain-rate-dependence of torque by switching rotation speed during deformation from the typical 0.2 rev/min to the limits of the equipment of 0.62 and 0.045 rev/min every 300 seconds(a). Detail of the transition from high to low(b) and from low to high(c) rotational speed during deformation.*

5.3. Microhardness after HPT Deformation

For each condition and temperature one sample was prepared as described in Section 3.4 and hardness was measured as outlined in Section 3.4.4. Supported by the results of the HPT pretests shown in figure 4.4, the hardness in the center of a typical cross-section was assumed to be representative of the overall condition. Therefore the following diagrams only show values measured along the center line as depicted in figure 3.11. For each condition the resulting micro-hardness due to the various deformation temperatures will be summed up in one diagram. For comparison with values measured on B and C samples of the raw material, hardness was measured on the cross-section on an undeformed disc of each typical condition.

5.3.1. S Condition

The resulting hardness on HPT-processed S samples for the typical deformation temperatures is depicted in figure 5.5. Deformation at -196°C appears very homogeneous showing almost perfect symmetry relative to the center and a saturation level of about 180 HV in the outer region. At room temperature, hardness looks unevenly distributed but seems to reach a saturation somewhat below 200 HV at high strains. For 100°C deformation hardness appears to level off at 160 HV. In the center for the temperatures up to 100°C hardness lies somewhere between 100 and 140HV.

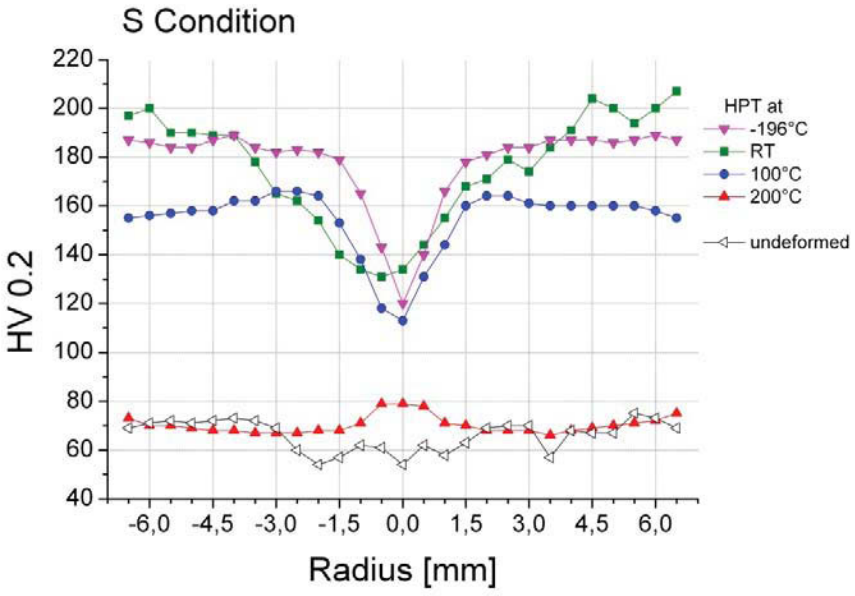

Figure 5.5.: *Microhardness on the radial cross section of S samples that were HPT deformed at various temperatures for 3.5 revolutions at 2.1GPa.*

After deformation at 200°C, at 80 HV hardness in the center is slightly higher than in the outer region (at about 70 HV). This may be due to a strain-rate-dependent dynamic restoration or recrystallization process,

which seem to start even at 100°C, indicated by the small peaks at a radius of ± 2 mm in the blue graph. Values of the black curve, representing an undeformed disc, are at least for r > 3 in good agreement with values measured on C samples as outlined in Section 2.4 and 2.5.

5.3.2. PA Condition

The hardness on HPT-processed PA samples is illustrated in figure 5.6. After RT deformation the evolution in hardness appears shifted relative to the center but increases almost linearly from around 70 HV, up to values between 180 and 200 HV towards the outer edges. HPT processing at 100°C leads to a center hardness of about 110 HV and seems to level off at 140 HV. After processing at 200°C the hardness shows a plateau of 70 HV and the center is slightly softer. Strangely, hardness of the undeformed PA disc is significantly lower than that determined with C samples of the raw material.

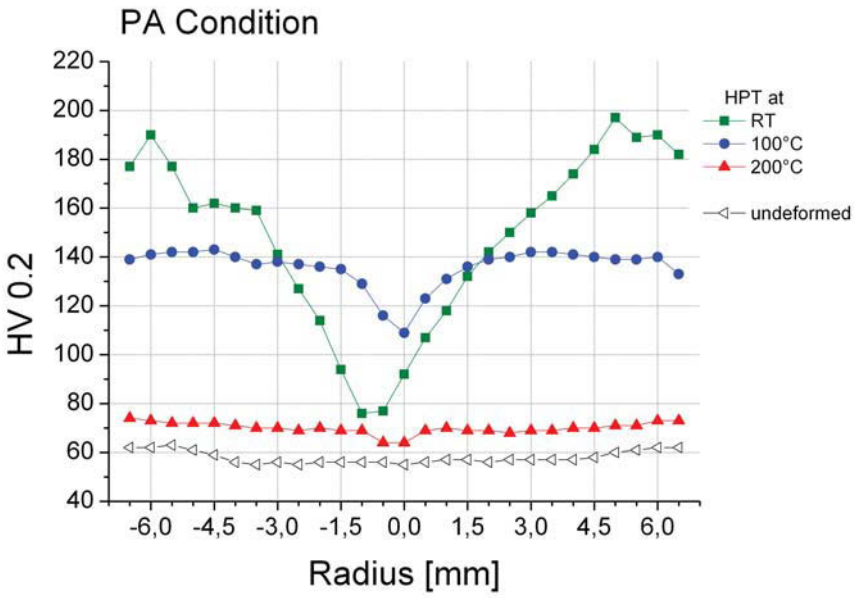

Figure 5.6.: *Microhardness over the radial cross section of PA samples that were HPT deformed for 3.5 revolutions at 2.1GPa, for various deformation tempertures.*

5.3.3. OA Condition

As observed on the S and PA conditioned specimens, the hardness profile after RT deformation is shifted away from the center. The values range from 70 HV in the least-deformed region at r = 1 mm, up to around 180 HV towards the edges.

HPT processing at 100 °C of the OA condition does not show a constant hardness level but rises up to 130 HV. The hardness in the center lies at about 70 HV after RT and 100 °C deformation. After 200°C HPT processing hardness levels off overall between 50 and 60 HV, somewhat lower than in the undeformed state.

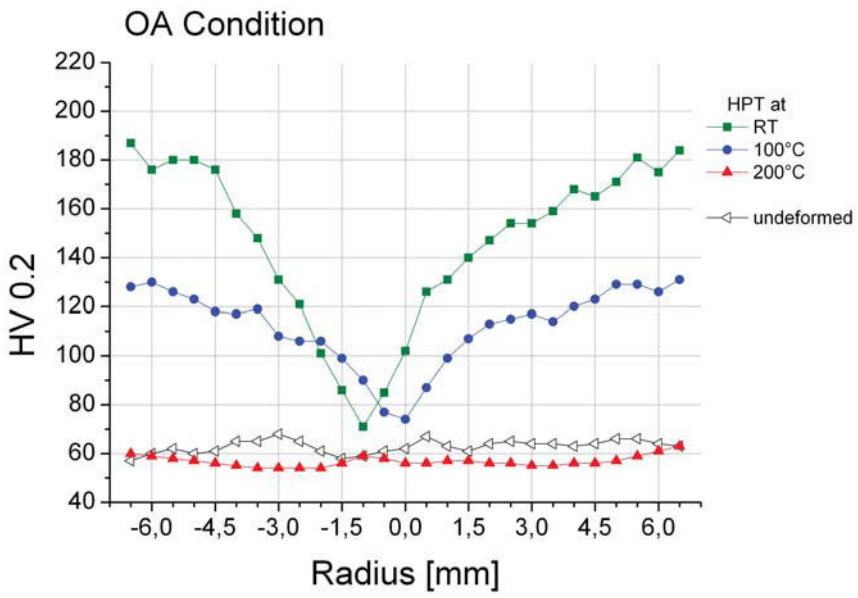

Figure 5.7.: *Micro-hardness over the radial cross-section of OA samples that were HPT deformed for 3.5 revolutions at 2.1GPa, at various temperatures.*

For the OA condition the central region keeps the hardness of the almost undeformed sample, for all the typical deformation temperatures. Hardness on the undeformed OA disc fits almost perfectly the values of the aging characteristic of the raw material outlined in Section 2.6.

5.4. Microstructure

The cast grain structure of the homogenized undeformed material is very coarse and visible to the naked eye on polished and etched samples, as depicted in figure 2.8 in Section 2.3.2. The precipitates formed during aging as well as the deformed material have a structural size in the sub-micron range and were therefore investigated by TEM and SEM. TEM observations were performed to identify the occurring phases and structural details as well as to facilitate interpretation of micrographs obtained with the SEM, which has poorer resolution but allows investigation of larger surface areas.

5.4.1. Raw Material TEM

Samples for TEM investigations were produced as described in Section 3.4.6. Since the original material has a very coarse grain structure with grain sizes in the millimetre range, the transparent area of the usable TEM samples lies within one grain and appears like a single crystal. For every defined condition one bright-field image and a [110] zone axis diffraction pattern will be presented.

Of the S condition a TEM bright-field image and the diffraction pattern of a [110] zone axis are depicted

in figure 5.8. The fine wavy structure is an artifact of electropolishing. No precipitates are visible in the bright field image and the diffraction pattern shows only the typical reflections of the fcc-Al lattice.

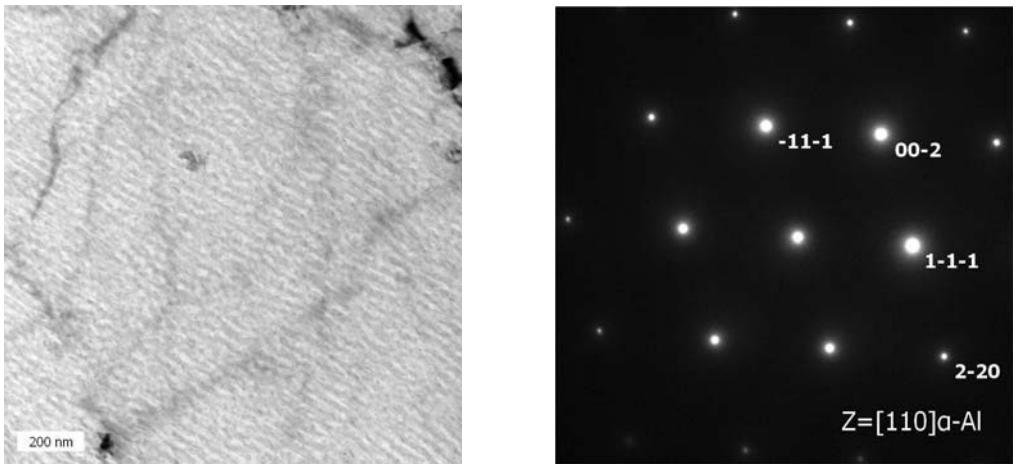

(a) S: BF (b) S: SAD pattern

Figure 5.8.: *(a) TEM brightfield image and (b) the diffraction pattern of a [110] zone axis of S raw material.*

The TEM bright field micrograph of a PA condition sample in figure 5.9(a) shows clearly the oriented precipitates. Additional reflections appear in the diffraction pattern in figure 5.9(b). Length as well as mean distance of the particles are about 200 nm, their thickness is about 20 nm.

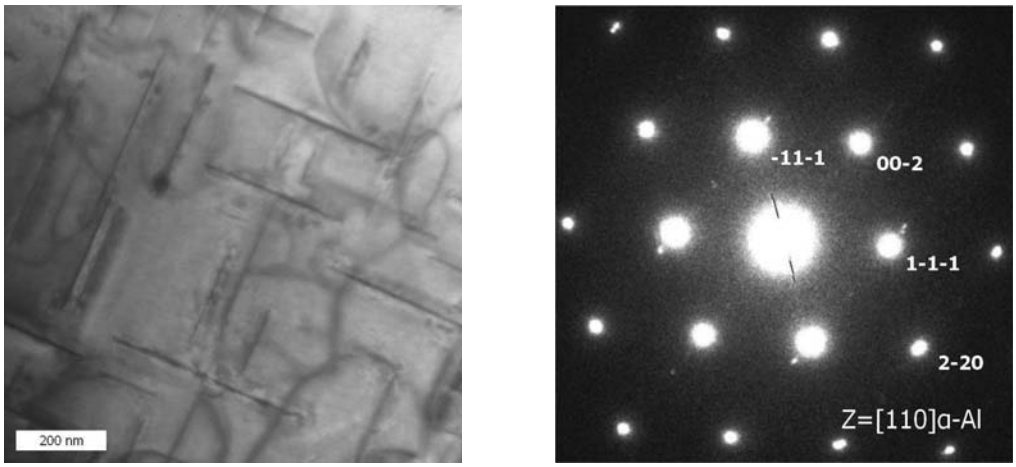

(a) PA: BF (b) PA: SAD pattern

Figure 5.9.: *(a) TEM brightfield image and (b) the diffraction pattern of a [110] zone axis of PA raw material.*

In OA condition the precipitates are larger as shown in figure 5.10(a). The major latitude of the particles is in a range of 0.5 to 1 μm while the mean distance is about 0.5 μm. The same additional diffraction spots show up more clearly separated from the basic fcc (α-Al) pattern, illustrated in figure 5.10(b). Indexing the additional reflections (oblique indices in figure 5.10(b)) revealed θ' precipitates in OA and PA condition.

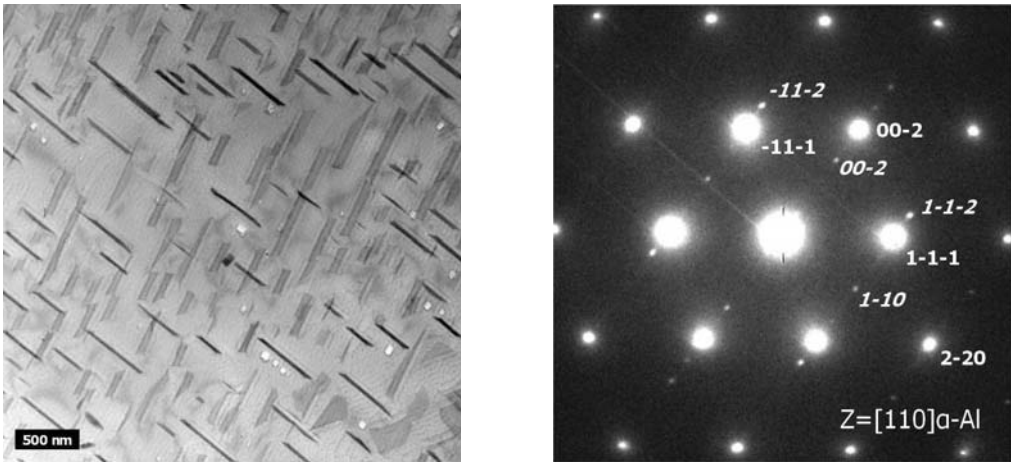

(a) OA: BF

(b) OA: SAD pattern

Figure 5.10.: *(a) TEM brightfield image and (b) the diffraction pattern for a [110] zone axis of OA raw material. The additional spots are indexed oblique and apply to θ' plates of the orientation: [001]θ' || [001]α-Al.*

5.4.2. Raw Material SEM

Figures 5.11(a-d) show some SEM (InLens) images of a mechanically ground/polished and subsequently electro-polished solution-treated undeformed sample. Images on the right give a more detailed view of the triple junctions depicted on the left.

Although electro-polishing delivered good TEM samples in the *TenuPol* device, no satisfactory results could be obtained with the *LaboPol* on SEM samples of HPT deformed material. A very finely structured artifact layer as well as etched cavities seem to form during electro-polishing dependent on the crystallographic orientation. Whilst providing good grain contrast on the coarsely structured undeformed material, this preparation method makes no sense on HPT deformed material with a structural size in the sub-micron range. So the more elaborate method of extensive mechanical polishing and subsequent ion milling was used to prepare deformed samples for SEM investigation.

Figures 5.11(e,f) show a SEM InLens micro-graph and for comparison the corresponding QBSD image of a grain boundary in an over aged (OA) sample, ground and polished as described in Section 3.4.5 but not ion milled. The image is a stroke of luck for it was taken in the almost undeformed central region of an OA disc that was RT HPT deformed for 1.1 revolutions in the framework of the HPT pretests. The oriented θ' precipitates inside the grains, the large incoherent θ particles on the grain boundary and the precipitation-free-zone are clearly visible.

(a) S condition-A: 1kx

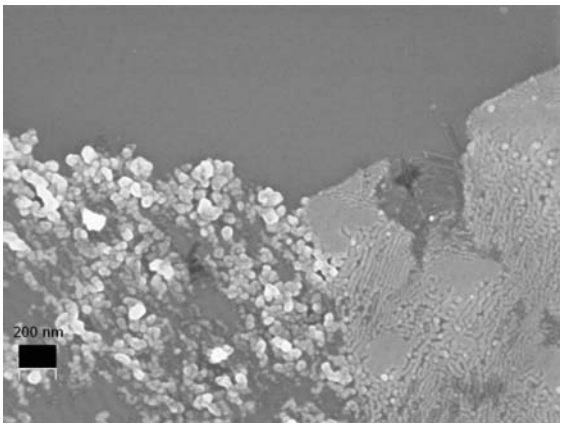

(b) S condition-A: 8kx

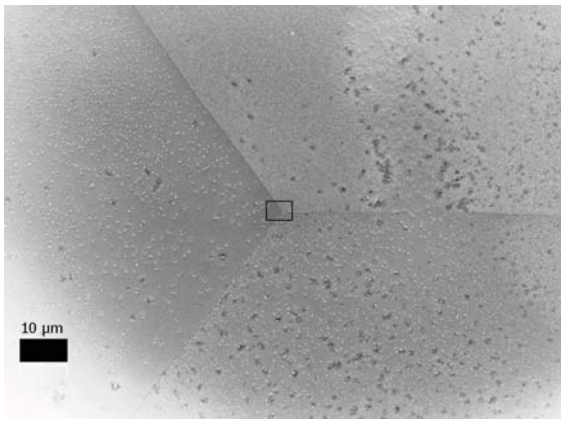

(c) S condition-B: 1kx

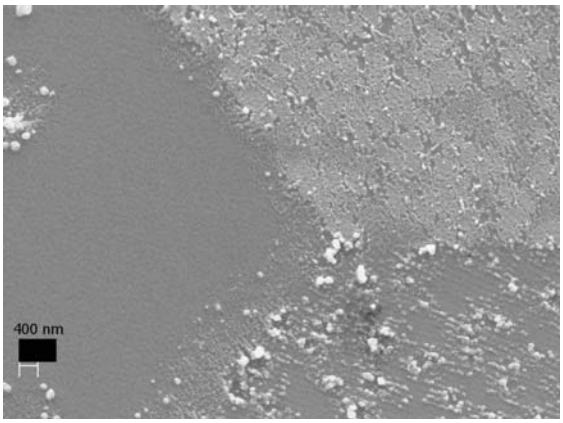

(d) S condition-B: 40kx

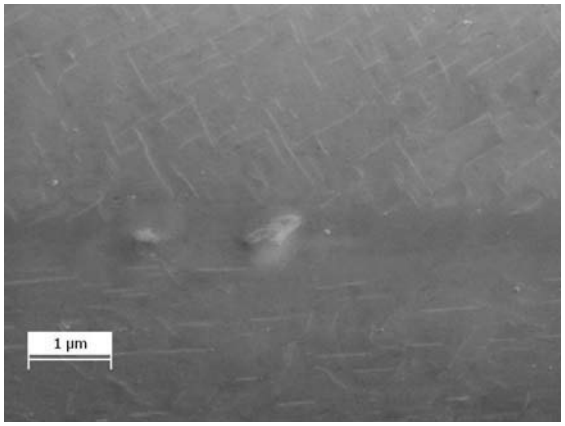

(e) OA condition: InLens

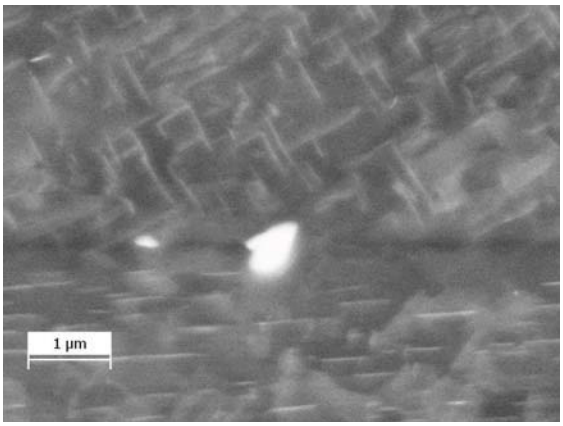

(f) OA condition: QBSD

Figure 5.11.: *Figures (a-d) are SEM InLens images of an electropolished S condition sample. Figures (b) and (d) are detailed views of the triple junctions in (a) and (c). Figures (e,f) are SEM InLens and QBSD images of a grain boundary in the almost undeformed central region on the radial cross section of an OA sample, HPT deformed at RT for 1.1 revolutions.*

5.4.3. HPT Deformed S Condition

Deformation at RT

From an S condition disc, HPT deformed at RT for 3.5 turns, TEM foils were prepared at a distance of 4.5 mm from the center in axial view as described in Section 3.4.6, representing an equivalent strain of 30. The TEM brightfield images in figure 5.12(a) and (b), reveal a structure consisting of high-angle grain boundaries with a grain size between 50 and 200 nm and incoherent θ phase particles $\leq$ 50 nm at triple junctions and along grain boundaries. A TEM (SA) brightfield overview is given in figure 5.12(c) besides a

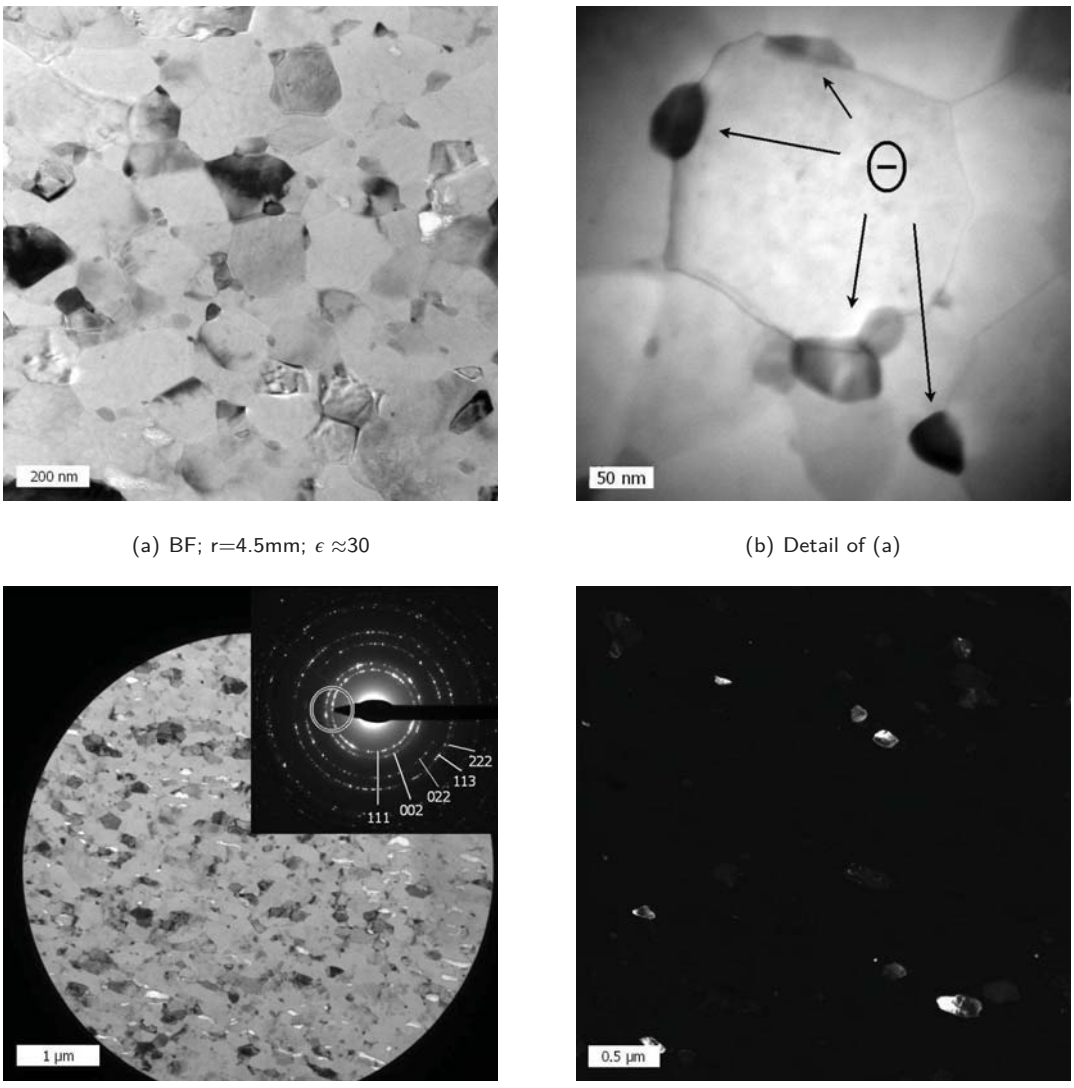

(a) BF; r=4.5mm; $\epsilon \approx$30

(b) Detail of (a)

(c) SA BF

(d) DF

Figure 5.12.: *TEM brightfield images obtained from an S conditioned sample after HPT deformation at RT for 3.5 revolutions at $\approx$ 4.5 mm from the center, matching an equivalent strain of $\approx$ 30, showing θ precipitates at grain boundaries and triple junctions. The darkfield image in (d) corresponds to the marked reflections in the SAD pattern, inserted in the SA brightfield image in (c).*

darkfield image in figure 5.12(d) corresponding to the reflections marked in figure 5.12(c). At this point it is appropriate to anticipate some results of aging and annealing after HPT deformation. The precipitates depicted in figure 5.12 grow large enough during aging at the typical temperature of 190°C, to be identified clearly by diffraction as well as by EDX measurements.

To have enough specimens to adjust the parameters for electro polishing with the TenuPol device, eight TEM discs were made from one HPT sample. To check quality for selection of the best foil as well as to compare the appearance of the occurring phases, TEM samples were investigated in the SEM. Figure 5.13 shows a TEM brightfield image and a SEM-QBSD image of the TEM sample the figures in this Section stem from. The orientation of the grains in axial view is clearly visible.

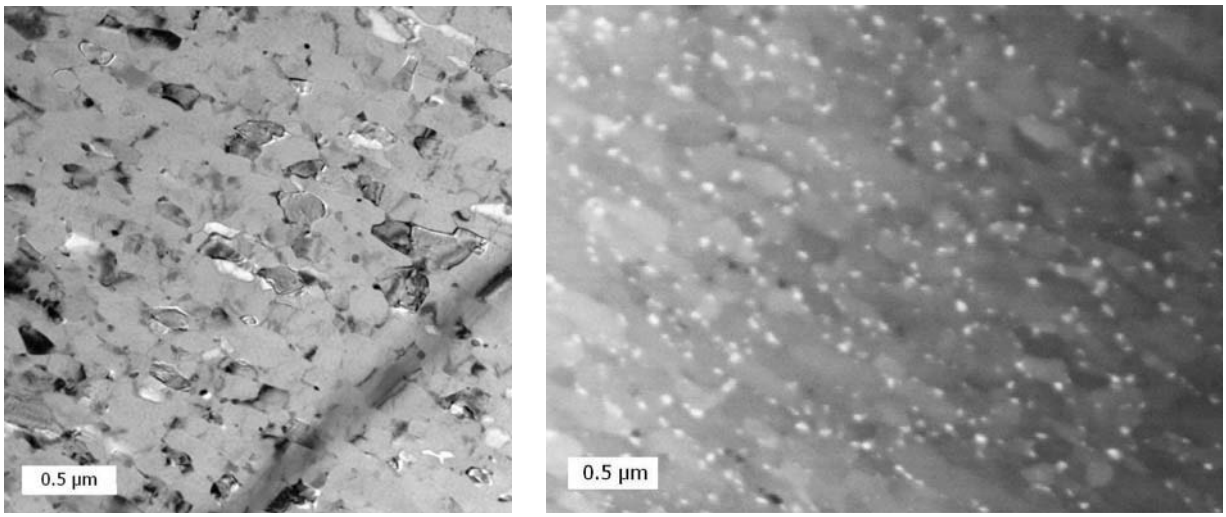

(a) TEM (b) SEM-QBSD

Figure 5.13.: *Comparison of TEM and SEM micrographs: TEM brightfield image (a) and SEM-QBSD image(b) of the same TEM foil of an S conditioned sample after HPT deformation at RT.*

The bright appearance of the precipitates in the SEM-QBSD image means a high intensity of back-scattered electrons due to the higher atomic number of copper relative to aluminum, according to the Rutherford scattering cross section, which is proportional to the atomic number squared. Figure 5.14 shows a series of SEM-QBSD images from the radial cross section of an S conditioned specimen, after HPT deformation at RT for 1.1 revolutions. The surface was mechanically polished and subsequently ion milled as described in Section 3.4.5. The sample was deformed within the framework of the pretests and the corresponding micro hardness and torque graphs are depicted in figure 4.1 in Section 4.1. It appears that up to an equivalent strain of about 6, illustrated in figures 5.14(a-c), a granular structure forms. Only a few small precipitates show up, that may have its source in the initial grain boundaries. A higher degree of deformation, depicted in figure 5.14(d), leads to further grain refinement and many precipitates. Compared with the previously shown TEM images, these should lie along grain boundaries and triple junctions.

Comparing figure 5.13(b), representing an equivalent strain of ≈30 and figure 5.14(d), apart from the differing direction of observation and magnification, the structure appears more or less the same and further structural refinement can hardly be obtained. This matches the resulting micro-hardness, illustrated in figure 4.1, which is of a comparable order of magnitude for the 1.1 and the 3.5 revolution deformed specimen at r = 4.5 mm. The torque during deformation at RT, depicted in figure 4.1, also matches the results, since the torsional moment levels off after about 1 revolution (an equivalent strain of about 10).

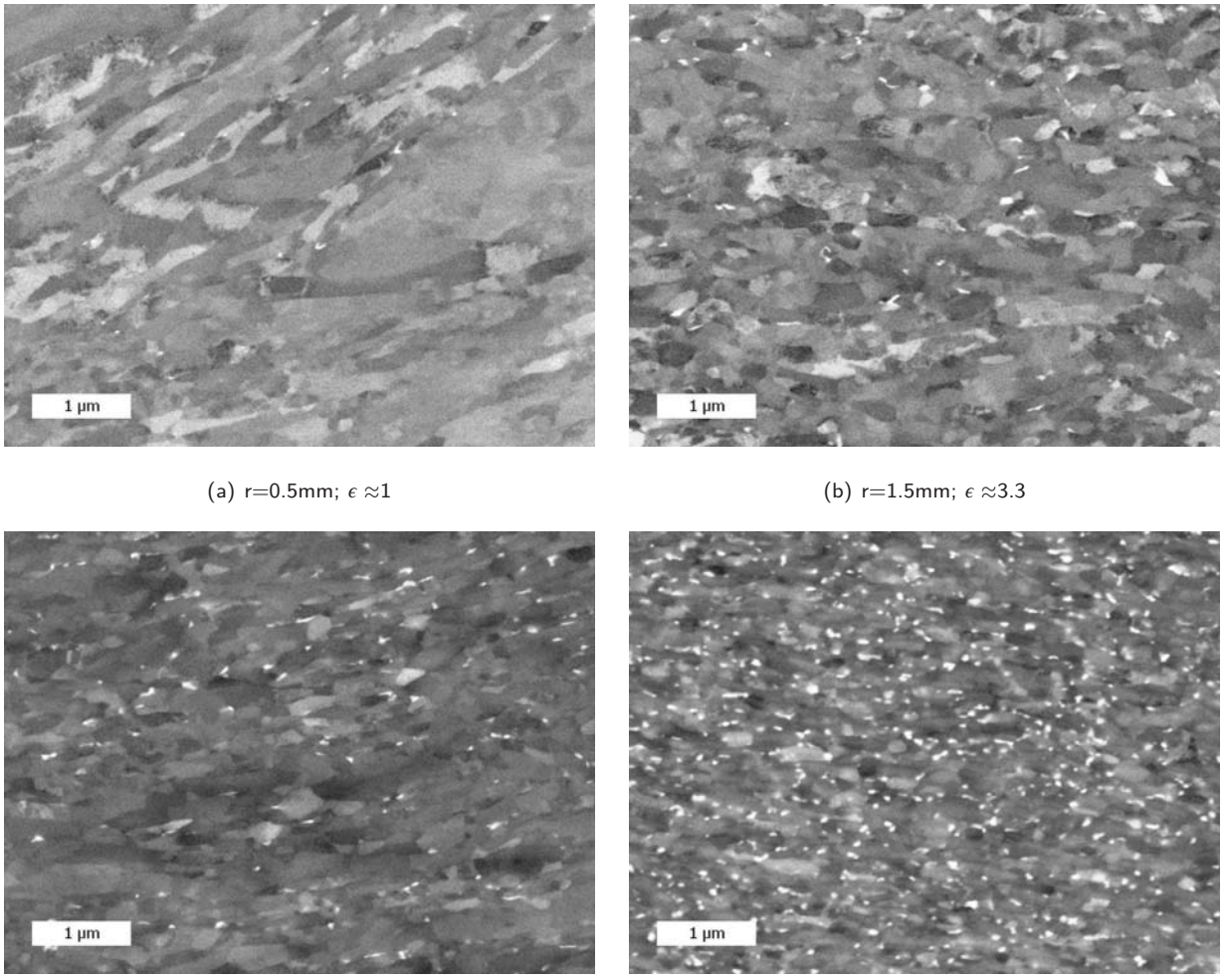

(a) r=0.5mm; $\epsilon \approx 1$

(b) r=1.5mm; $\epsilon \approx 3.3$

(c) r=3mm; $\epsilon \approx 6.6$

(d) r=4.5mm; $\epsilon \approx 10$

Figure 5.14.: *Series of SEM QBSD images in radial view on a S conditioned sample, HPT deformed for 1.1 revolutions, in various distances r from the center representing different equivalent strains ϵ.*

S: Deformation at 200°C

An S conditioned specimen, deformed at 200°C for 3.5 revolutions at 2.1 GPa, was polished and ion milled as described in Section 3.4.5. The microstructure in radial view in the central little deformed region is depicted in figure 5.15. It is hard to specify the corresponding radius and strain for each image, since the

center can not be determined exactly, and the images were recorded within a radius between ≈ 0.2 and 0.5 mm. The sequence may represent an increasing degree of deformation, which possibly varies locally in the vicinity of the theoretically undeformed center. Two initial grain boundaries, decorated by small precipitates, as well as a sub-grain structure in between, are clearly visible in figure 5.15(a). The figures (b) and (c) show the original grain boundaries disrupted and disintegrated.

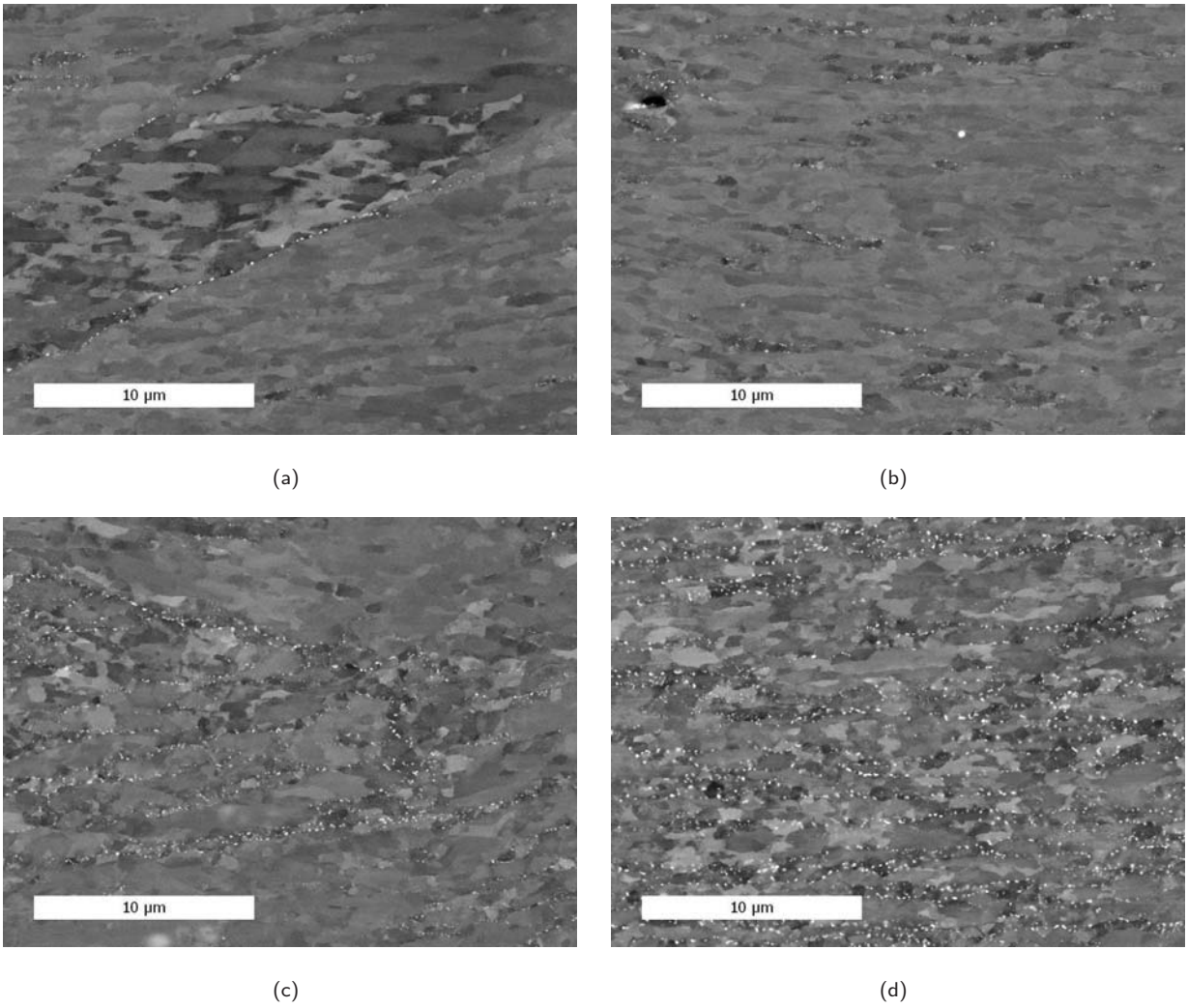

Figure 5.15.: *Series of SEM-QBSD images in radial view of an S conditioned sample, HPT deformed at 200° C for 3.5 revolutions, at a distance from the center between 0.2 and 0.5mm, representing an equivalent strain of about 1 to 3.*

The structure in figure 5.15(c) may be seen as a transition to the saturation structure depicted in figure 5.16. Compared with the resulting micro-hardness after 200°C deformation shown in figure 5.5, it is not surprising that the microstructure looks virtually the same at radii of 1.5 and 4.5 mm, illustrated in figure 5.16(a) and (b).

The small blurred white spots in figures 5.16(a-c) are sub-surface precipitates, visible due to the generally large interaction volume of aluminum, which in this case, using an accelerating Voltage of 20kV, might be in the micrometre range. For comparison, the image in figure 5.16(b), recorded with 1kV electrons, shows no blurred sub-surface particles, but only in-surface precipitates with curtailed grain contrast. All SEM-InLens images are practically first scans of the depicted area. The surface contaminates very fast under electron bombardment, especially at higher magnifications, making it impossible to get two usable scans of the same area at different accelerating voltages. The horizontal lines and the black spots in figure 5.16(c,d) and 5.17 may stem from fast overview scanning at low magnifications to orient oneself on the specimen or from rough adjustment of stigmation and alignment of the apertures.

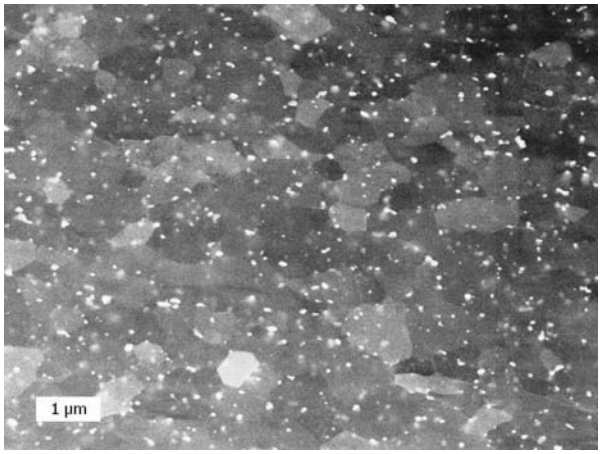

(a) r=1.5mm; $\epsilon \approx 10$

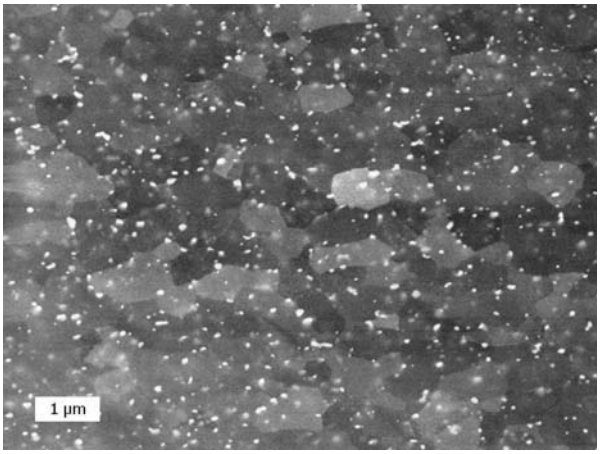

(b) r=4.5mm; $\epsilon \approx 30$

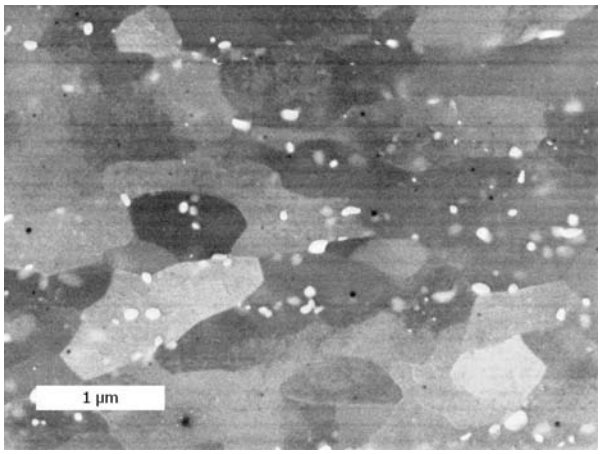

(c) r=3mm; $\epsilon \approx 20$; 20kV

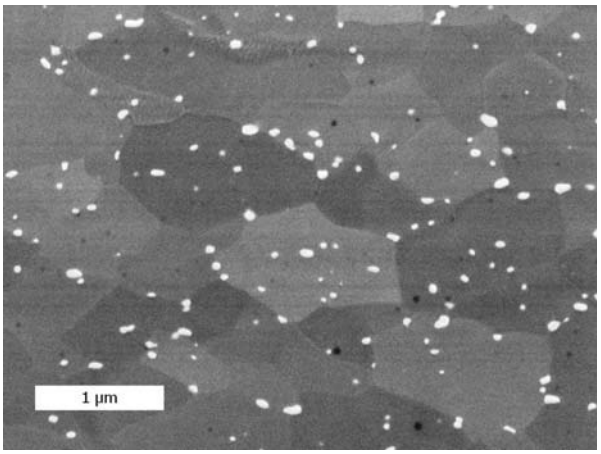

(d) r=3mm; $\epsilon \approx 20$; 1kV

Figure 5.16.: *SEM-InLens images in radial view of an S conditioned sample, HPT deformed at 200°C for 3.5 revolutions, at a distance of 1.5 mm(a) and 4.5mm(b) from the center, representing an equivalent strain of ≈ 3.3 and ≈ 10 respectively and two SEM-InLens images at r = 3 ($\epsilon \approx 20$), using an accelerating voltage of 20kV(c) and 1kV(d).*

The apparent size of the precipitates, because of their strong contrast relative to the aluminum matrix, depends on brightness and contrast adjustment as well as on the magnification, and can therefore not be determined exactly but can be well estimated. In figures 5.16(c,d) and 5.17, large particles, with a size of about 50 to 100 nm, lie at triple junctions and along grain boundaries while very small particles also appear inside the grains, possibly at dislocations and/or sub-grain boundaries. Because of their morphology and the formation at interfacial-energy- minimizing sites, the particles are considered to be incoherent θ phase precipitates. The grains are between $\approx$ 200 nm and 1 μm in size.

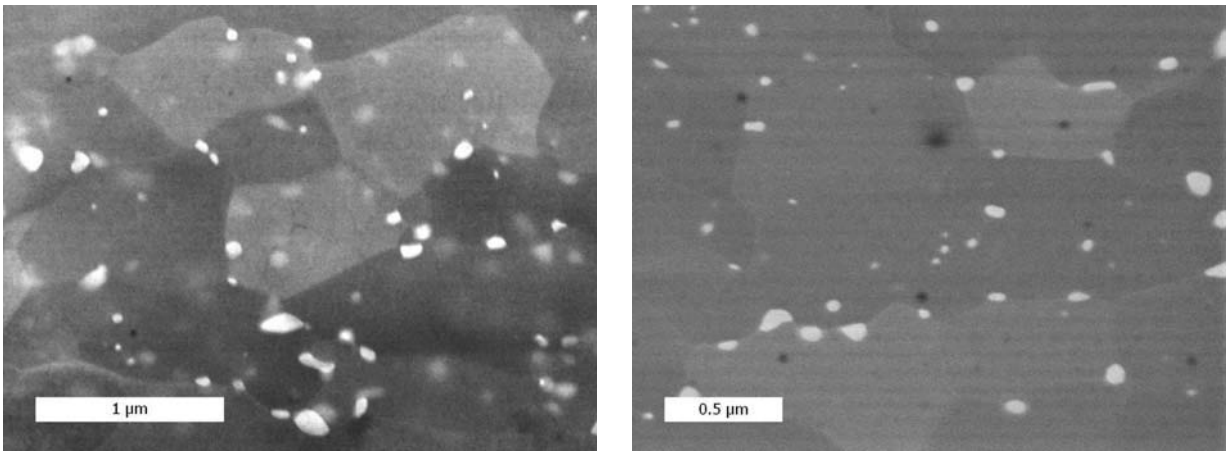

(a) (b)

Figure 5.17.: *SEM-InLens images in radial view of an S conditioned sample after HPT deformation at 200° C for 3.5 revolutions, with an accelerating voltage of 20kV(a) and 1kV(b).*

5.4.4. HPT Deformed PA Condition

The images in figure 5.18 are from a PA specimen, that was RT HPT deformed for 3.5 revolutions as described in Section 3.4.5 but not ion milled. Each area was firstly scanned with low noise reduction using the InLens detector, illustrated by the images on the left, and subsequently scanned slowly with high noise reduction using the QBSD detector. The InLens images show the grain structure and precipitates just slightly covered by a thin layer and some bubbles, possibly silica particles, left from polishing. Nevertheless comparing the QBSD images on the right with micro-graphs obtained from sputtered S condition samples, gives an idea of what happens when HPT processing PA material. The precipitates appear as white streaks that are disrupted and maybe dissolved with increasing degree of deformation. At very high strain in the narrowing part of the HPT disc (r $>$ 4.5 mm), illustrated in figure 5.18, the structure looks similar to the HPT deformed S condition.

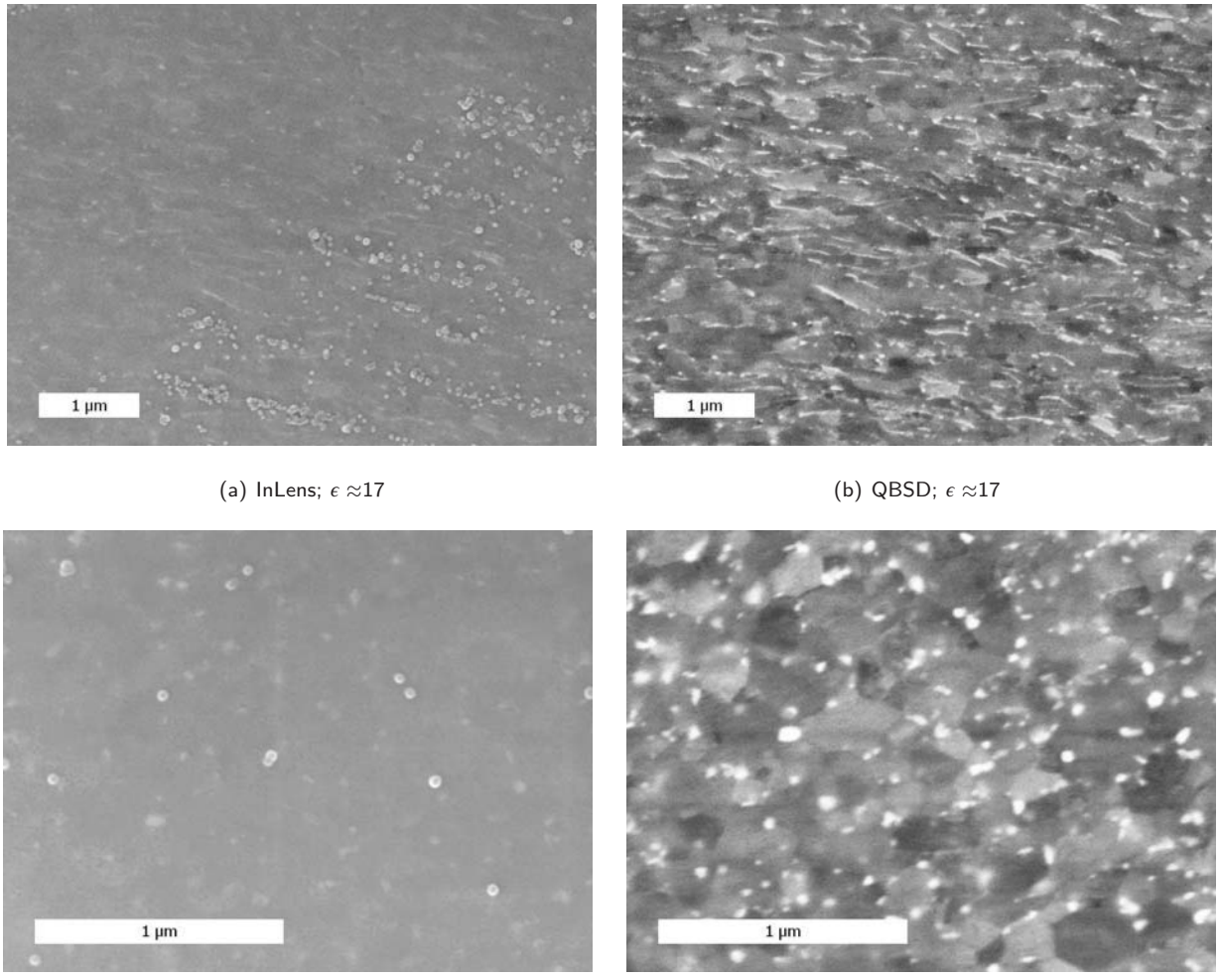

(a) InLens; $\epsilon \approx 17$

(b) QBSD; $\epsilon \approx 17$

(c) InLens; $\epsilon > 30$

(d) QBSD; $\epsilon > 30$

Figure 5.18.: *Comparison of SEM-QBSD and -InLens images in radial view of a PA conditioned sample, HPT deformed at RT for 3.5 revolutions, at distances of 2.5 mm(a,b) and < 4.5mm(c,d) from the center, representing an equivalent strain of ≈17, ≈23 and >30, respectively.*

5.4.5. HPT Deformed OA Condition

Following the sequence of images in figure 5.19(a) to (f), representing different equivalent strain the sample experienced, the structure appears similar to the PA condition. With increasing degree of deformation the precipitates get more and more disrupted. For the OA condition the precipitates seem to disintegrate slower during deformation. Comparing figure 5.19(a) and (f), fragments of the particles get smaller and more homogeneously distributed with increasing strain. The horizontal precipitation-free strip in figure 5.19(c) apparently stems from an initial grain boundary, indicated by the large precipitate on the right.

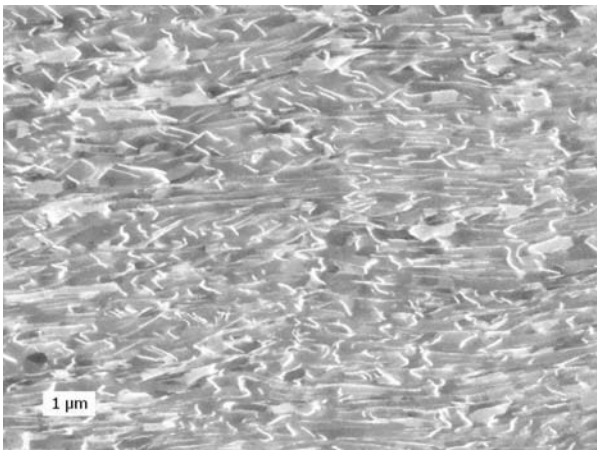

(a) r = 1 mm; $\epsilon \approx 7$

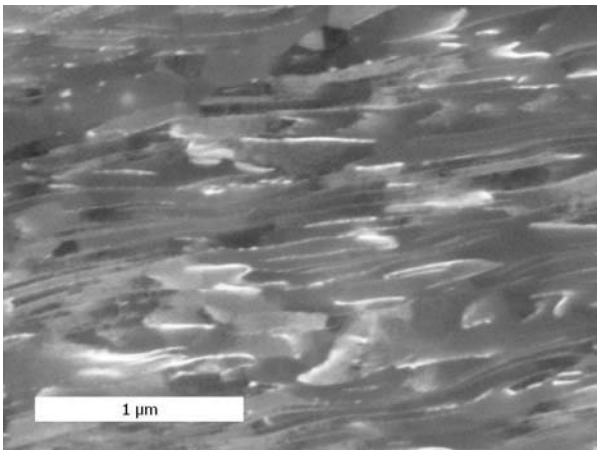

(b) r = 2 mm; $\epsilon \approx 13$

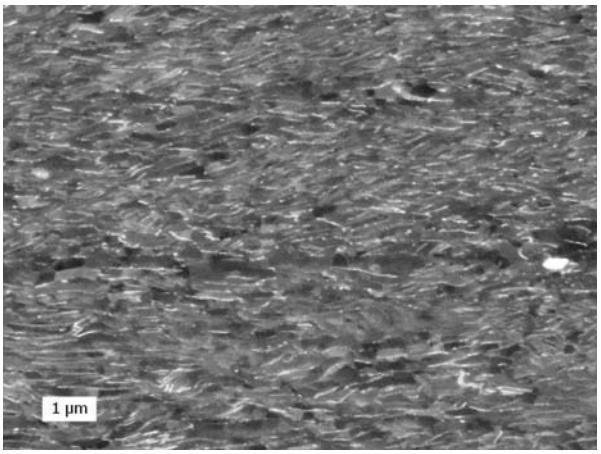

(c) r = 2 mm; $\epsilon \approx 13$

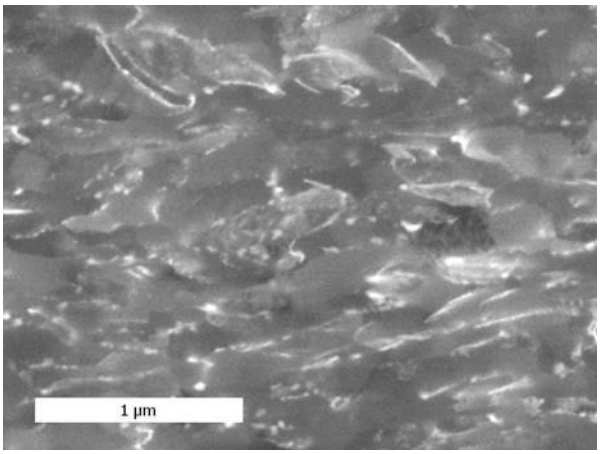

(d) r = 3 mm; $\epsilon \approx 20$

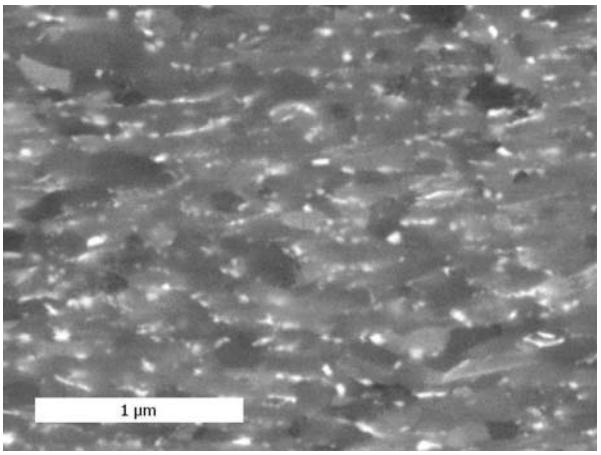

(e) r = 4 mm; $\epsilon \approx 26$

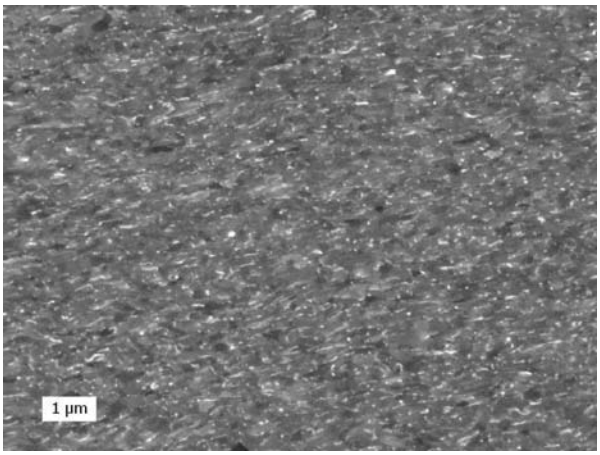

(f) r = 4.5 mm; $\epsilon \approx 30$

Figure 5.19.: *SEM-QBSD images in radial view of an OA conditioned sample, HPT deformed at RT for 3.5 revolutions, at distances of 1 mm(a), 2 mm(b,c), 3 mm(d), 4 mm(e) and 4.5mm (f) from the center, representing an equivalent strain of $\approx$13, $\approx$20, $\approx$26 and $\approx$30, respectively.*

Chapter 6.

Aging after HPT Deformation

6.1. Overview

The aging and annealing characteristic of the deformed material was determined as described in Section 4.2 using samples that were produced as outlined in Section 3.4. In this chapter only the resulting aging characteristics measured in the saturation regime will be presented, while the full dataset with the definition of the saturation regime and a more detailed illustration of the aging curves can be found in Section D of the appendix. An overview of the conducted measurements and investigations is given in Table 6.1.

Table 6.1.: *Overview: Aging experiments after HPT deformation and the performed microstructural analysis*

		Material Condition		
		S	**PA**	**OA**
HPT at	**RT**	MH [1], AC [2], TEM [3], SEM [4]	MH, AC	MH, AC
	100°C	MH, AC, SEM	MH,AC	MH,AC
	200°C	MH, AC, SEM	MH,AC	MH,AC
	-196°C	MH, AC		

[1] Micro Hardness, [2] Aging Characteristic
[3] TEM investigations, [4] SEM investigations

For each material condition and temperature at least two samples were sectioned for further aging and annealing. One HPT disc was sectioned into eight parts. A second one was halved and one half of it quartered to get twelve specimens for each single aging curve. The radial cross section of the remaining half was prepared for SEM investigations. From a separate HPT disc TEM foils were prepared, as described in Sections 3.4.6 and 3.4.6.

6.2. Aging Characteristics of HPT Deformed Material

6.2.1. S Condition

The resulting aging characteristic after HPT deformation at the typical temperatures, is shown in figure 6.1. Aging S samples after RT and 100°C deformation shows almost the same evolution of hardness with aging time, notwithstanding the difference in initial as-deformed hardness. After deformation in liquid nitrogen, hardness drops more slowly within the first day, while after HPT processing at 200°C hardness seems stagnate within the first 6 min, followed by a slow decrease. For all the typical deformation temperatures, after about one week at the typical aging temperature, hardness appears to level off somewhat above 40 HV.

For comparison, the aging characteristic of the undeformed material as measured using C samples is inserted, represented by small black symbols. During aging and annealing HPT deformed specimens, hardness levels off even below values of the aged undeformed material.

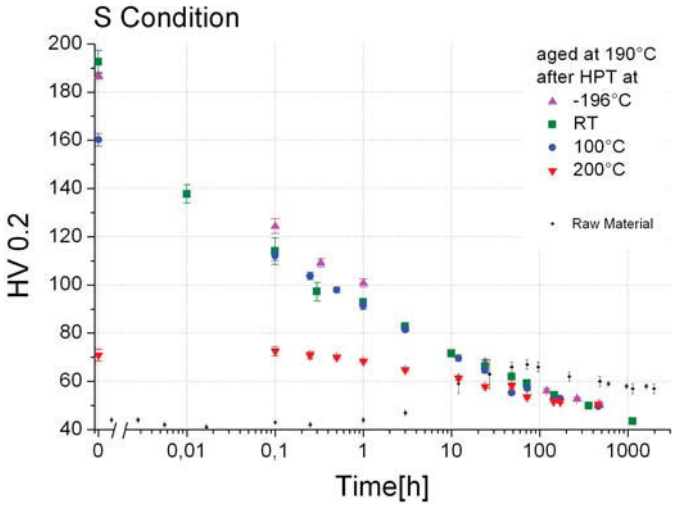

Figure 6.1.: *Summary of aging characteristics after HPT deformation at various temperatures of specimens in S condition, from values measured in the saturation regime.*

6.2.2. PA Condition

The aging characteristic of PA samples after HPT processing appears to be virtually the same as for the S condition. The difference in as-deformed hardness after RT and 100°C deformation is equalised after a few minutes at the typical aging temperature of 190°C. During aging after 200°C deformation, hardness stagnates for ≈6 min and then decreases slowly. Just as for the S condition, hardness levels off about 40 HV after long aging times. Although, according to the pretests, the deformation behavior was considered to be inhomogeneous, at least in the saturation regime the aging and annealing behavior appears very uniform.

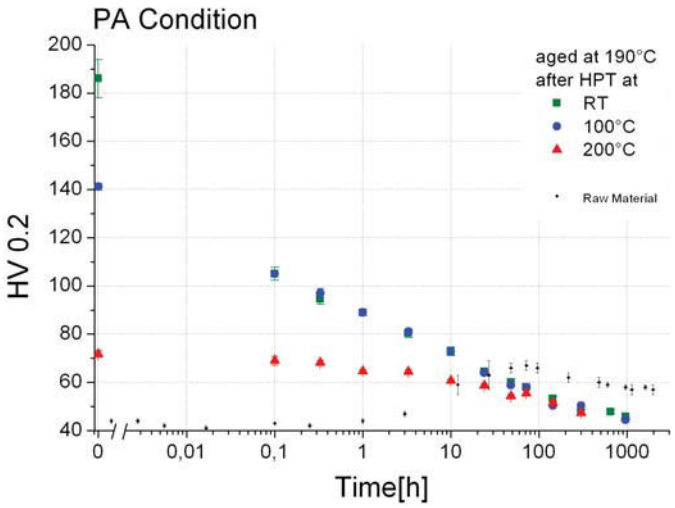

Figure 6.2.: *Summary of aging characteristics after HPT deformation at various temperatures of specimens in PA condition, from values measured in the saturation regime.*

6.2.3. OA Condition

Aging of HPT deformed OA samples, illustrated in figure 6.3, appears similar to that for the S and PA condition. Hardness of RT and 100°C deformed specimens equals within a few minutes somewhat below 120 HV. Aging after 200°C HPT leads to a clearly visible rise within the first 6 minutes. In general the OA material seems to be softer, but during aging hardness decays with the same slope as the S and PA conditions, and after about three days shows the same hardness level.

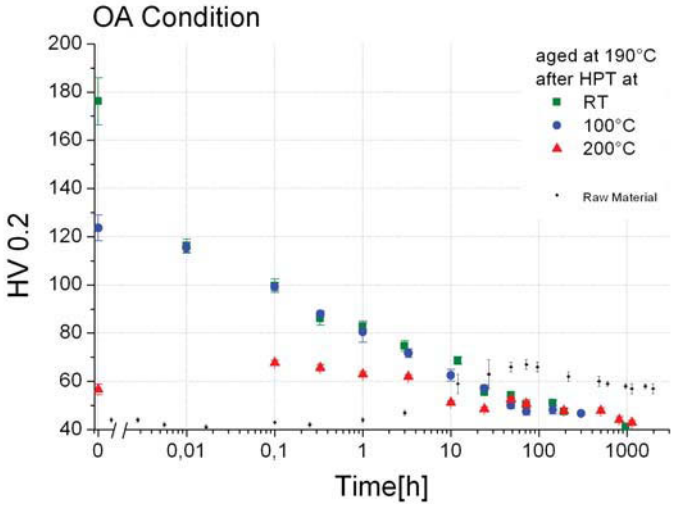

Figure 6.3.: *Summary of aging characteristics after HPT deformation at various temperatures of specimens in OA condition, from values measured in the saturation regime.*

6.2.4. Summary: Aging after HPT

for S and PA material condition the aging behavior after RT and 100°C HPT deformation appears to be virtually the same. The initially differing hardness becomes equal within minutes at about 110 HV and further decreases below peak hardness of the undeformed material after about 2 days, leveling off somewhat above 40 HV. A more specific look shows that values for the PA condition lie slightly lower than for S material but decrease with the same slope. The RT and 100°C HPT-processed OA material is slightly softer, but shows a very similar behavior.

The aging characteristic after 200°C HPT deformation appears noticeably different from that after deformation at the typical lower temperatures. For S and PA conditions the almost equal yield strength after 200°C HPT processing stagnates in the early stages of aging. The distinctly lower as-deformed hardness of the OA material apparently rises within the first minutes. After ≈6 minutes, hardness decreases slowly to an equal level for all three material conditions.

Comparing the shape of the hardness evolutions, the OA 100°C and PA 200°C processed material may be considered somewhere in transition between these two characteristics. Nevertheless for all material conditions and deformation temperatures, during aging at 190°C for very long times the hardness appears to level off at about 40 HV.

6.3. Microstructure after Aging

The the aging and annealing characteristic after HPT processing seems to be very similar for the various processed material conditions. Since sample preparation is laborious and costly, only S conditioned specimens were investigated in detail. Comparing the microstructure as deformed and after aging near to an equilibrium level, may give an idea of what happens in between. Discs of HPT-deformed S condition were aged at 190°C for 144 hours (6 days). That is, looking at the aging characteristics in the previous section, approximately the point where the graphs meet at about 50 HV, and further aging shows just small changes in hardness. The structure of the aged HPT-processed S conditioned specimens, shown in this section, was assumed be representative also for PA and OA condition, especially for long aging times, because of the general similarity of the aging characteristics.

6.3.1. Aged after RT Deformation

The microstructure of a RT deformed S condition specimen, aged for 144 hours at 190°C, is illustrated in figure 6.4 and shows equiaxed grains of about 1 to 2 μm in size and many precipitates. The image in figure 6.4(a) was obtained in a very thin area of the TEM foil, while 6.4(b) was taken in a thicker region. A more detailed look is given in figure 6.5. EDX measurement, showing 64.9 at% Al and 35.1 at% Cu (which

matches the chemical composition of Al_2Cu), and the inserted SAD pattern, clearly identifies the marked particle in figure 6.5(c) as an icoherent equilibrium θ phase precipitate. Large precipitates, between 50 and 200 nm in size, occur at triple junctions and at grain boundaries, while smaller particles appear inside the grains, as shown in figure 6.5(b). The fine wavy structure is an artifact from electro-polishing.

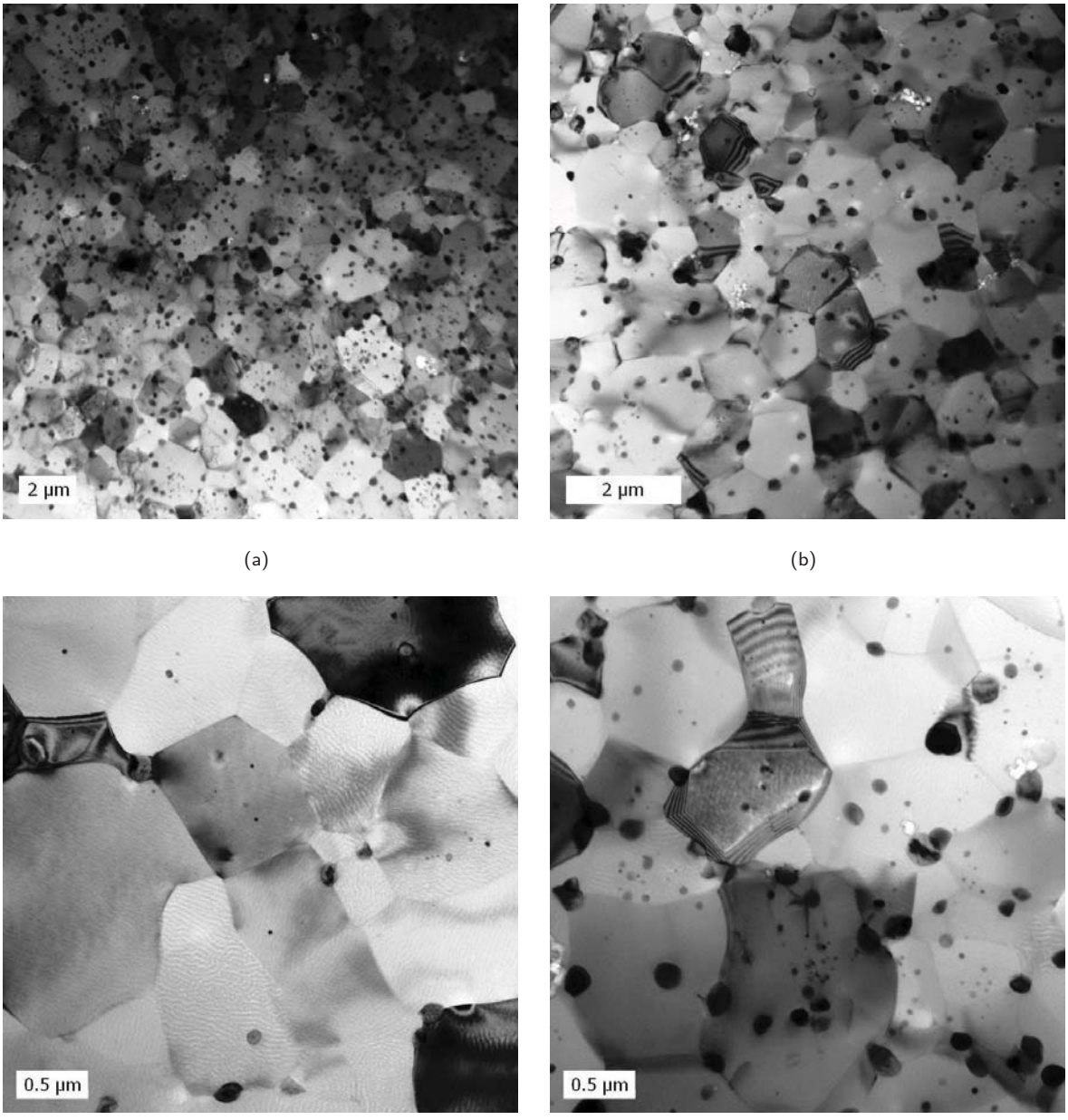

(a) (b)

(c) thin area (d) thick area

Figure 6.4.: *TEM brightfield images of an S conditioned sample, HPT deformed at RT for 3.5 revolutions, in a distance from the center of about 4.5 mm, representing an equivalent strain of ≈30, after subsequent aging for 144h at 190°C.*

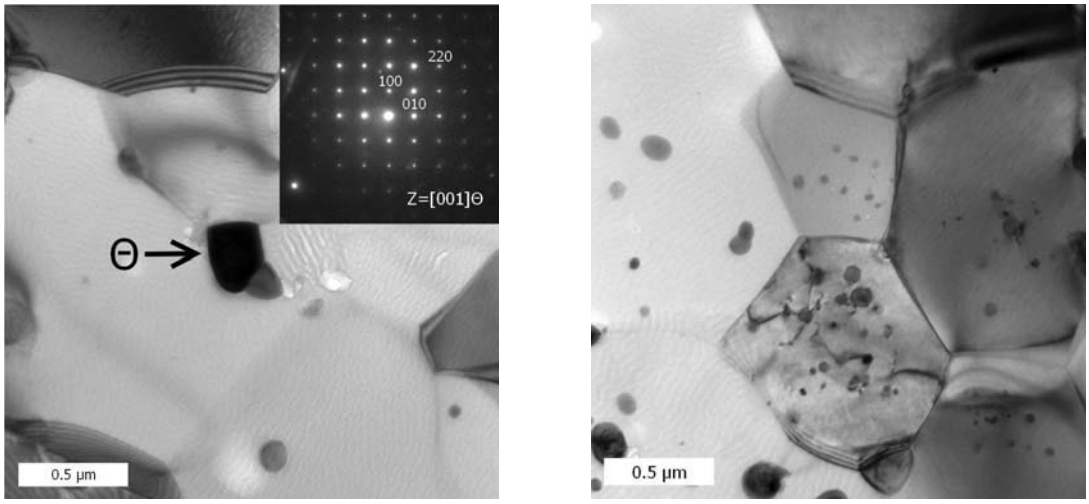

(a) (b)

Figure 6.5.: *TEM brightfield images in axial view of an S conditioned sample, RT-HPT deformed for 3.5 turns and subsequently aged at 190°C for 144h. The inserted diffraction pattern in (a) stems from the marked θ precipitate.*

6.3.2. Aged after 100°C Deformation

Specimens of S material aged for 144 hours at 190°C after 100°C and 200°C HPT deformation, were prepared for SEM investigations as described in Section 3.4.5. The SEM images in figure 6.6 depict the microstructure after aging the 100°C HPT deformed S material for 144 hours at 190°C. For better grain contrast the QBSD detector at 20kV accelerating voltage was used. Furthermore the grey-scale was inverted for better comparison with the TEM micrographs and to get a better view of the precipitates that do not outshine the grain background so intensely. It seems that a higher degree of deformation results in larger grains as well as more and larger precipitates during aging and annealing.

In the little deformed central region, θ phase precipitates appear presumably at the initial grain boundaries, besides small oriented, possibly θ' precipitates, in the regions in between, as illustrated in figure 6.6(e,f).

EDX measurements on two large precipitates were carried out, using 6kV accelerating voltage to reduce the interaction volume. Because of strong drift the beam stayed focused on the particle only for about 20 to 30 seconds to record EDX spectra. Nevertheless the results in table 6.2 reflect clearly the Al_2Cu composition.

Table 6.2.: *Results of EDX measurements on two precipitates*

	at% Al	at% Cu
Precipitate 1	67.07	32.93
Precipitate 2	66.20	33.80

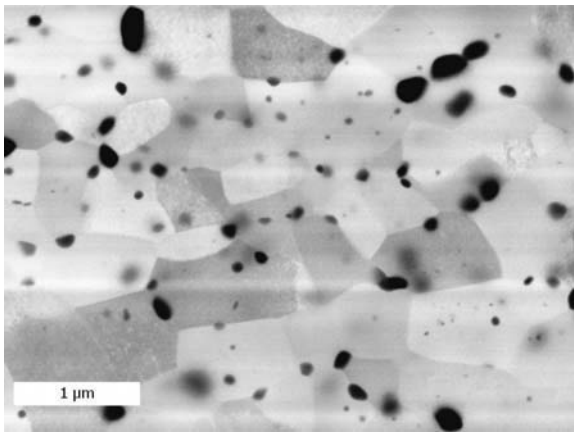

(a) r = 1 mm

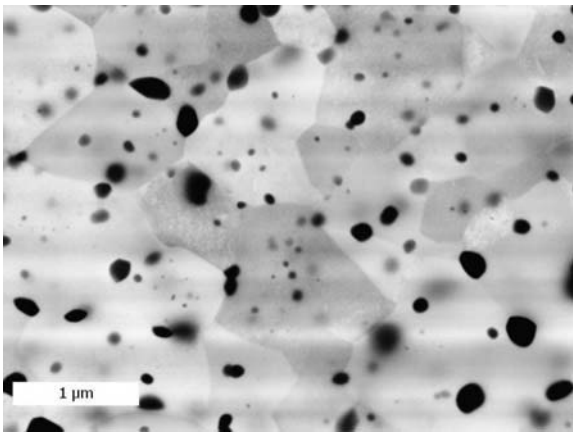

(b) r = 3 mm

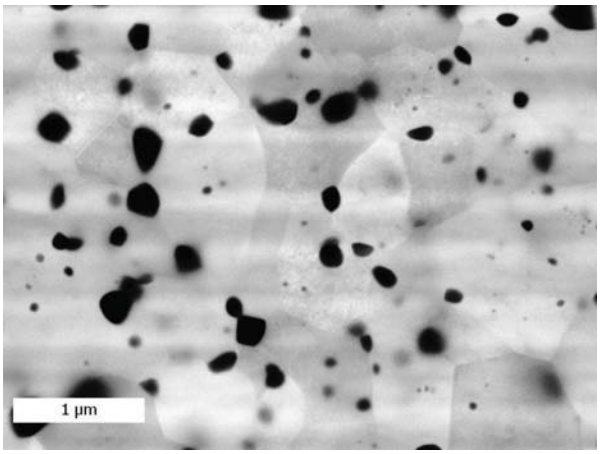

(c) r = 4.5 mm; radial

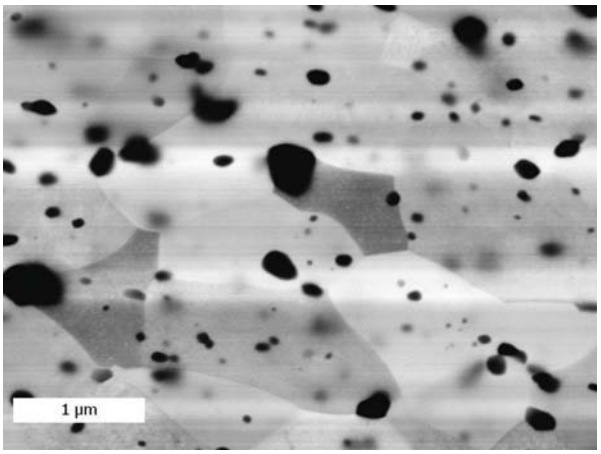

(d) r = 4.5 mm; tangential

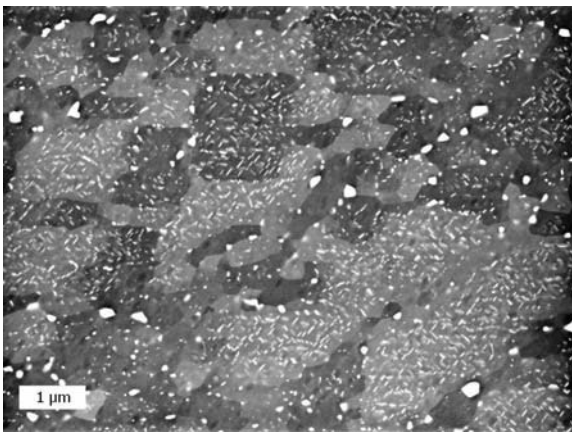

(e) Center, r ≈ 0

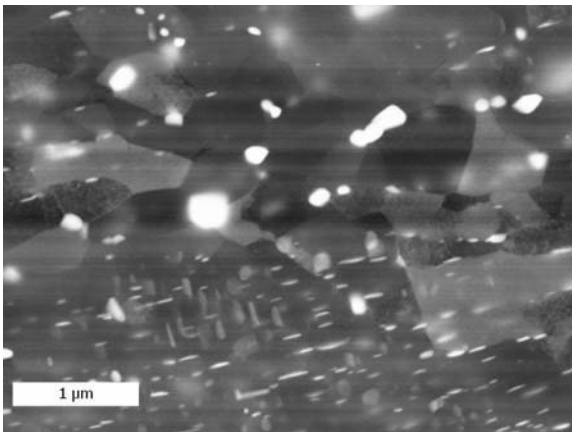

(f) Center, r ≈ 0

Figure 6.6.: *Greyscale-inverted SEM-QBSD images of an S conditioned sample aged after HPT deformation at 100°C for 3.5 revolutions, at a distance from the center of 1 mm(a), 3 mm(b) and 4.5 mm(c) in radial, and at 4.5 mm in tangential(d) view. (e,f) SEM-QBSD images in radial view in the central low deformed region.*

6.3.3. Aged after 200°C Deformation

The structure formed during aging a 200°C HPT deformed S condition specimen, is depicted in figure 6.7. The sample surface was ion milled after mechanical polishing. In the central region, shown in figure 6.7(a) and (b), the grain structure is less pronounced. The highly deformed areas in figure 6.7(c) and (d) look very similar to that formed during aging after RT and 100°C deformation. Comparing figure 6.7(c) and (d), at r = 4.5 mm the grains appear coarser with fewer but larger precipitates than at r = 3.5 mm.

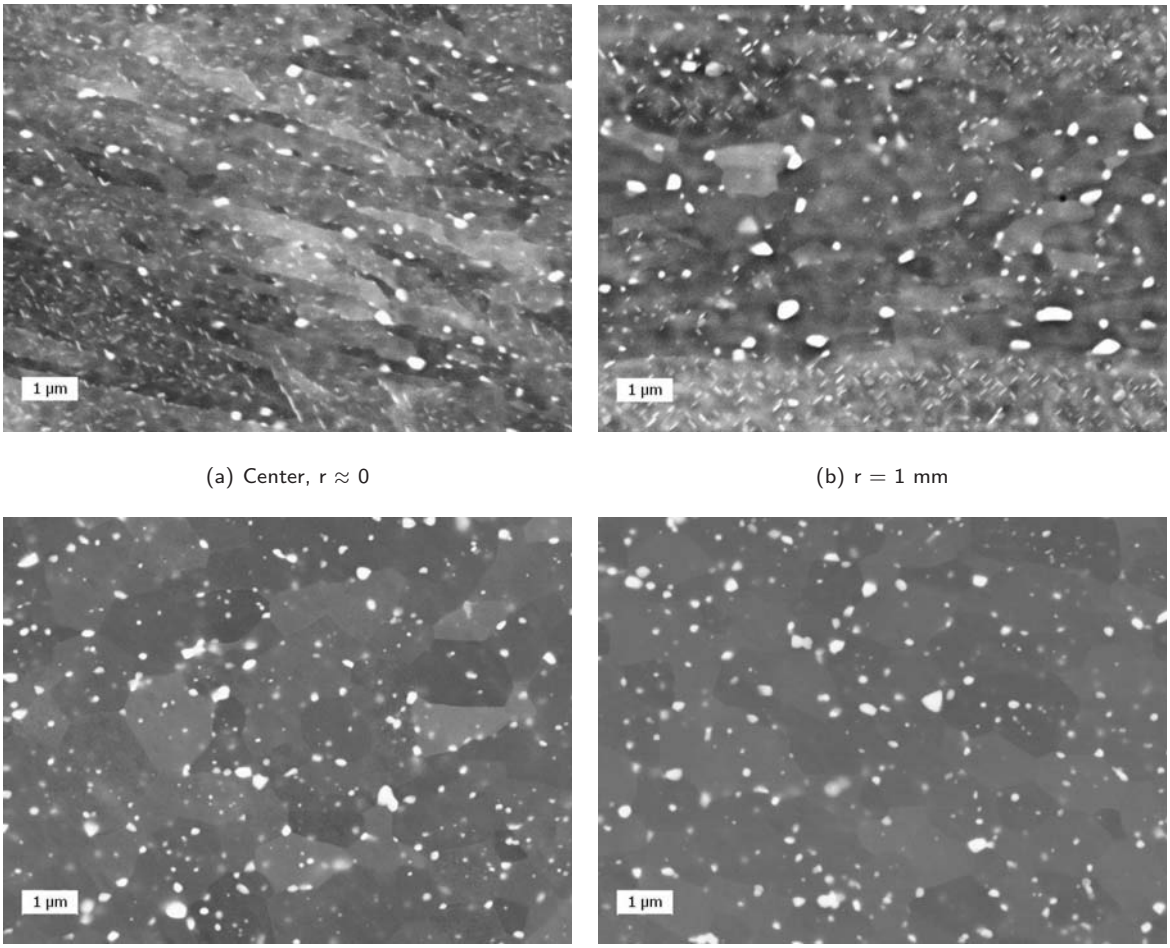

(a) Center, r ≈ 0

(b) r = 1 mm

(c) r = 3.5 mm

(d) r = 4.5 mm

Figure 6.7.: *SEM-InLens images in radial view on a S conditioned sample aged for 144 hours at 190°C after HPT deformation at 200°C for 3.5 revolutions, in the center(a) and in a distance of 1 mm(b), 3.5 mm(c) and 4.5 mm(d).*

Chapter 7.

Discussion

For HPT experiments, the feasiblity of a saturation in structural refinement and the mechanisms facilitating its maintenance during deformation are of special interest. For a constant torsional moment during HPT, the generation and annihilation of defects must be balanced. To miantain a saturated microstructure consisting of mainly high-angle grain boundaries, the total amount of interface has to keep constant by annihilation and generation of grain boundaries by boundary migration. A process similar to dynamic recrystallisation at high deformation temperatures, and stress- and strain-induced boundary migration at low temperatures, are the suggested mechanisms to maintain a steady-state torque and a saturated microstructure[16]. Results of SPD experiments by ECAP-A, which also uses simple monotonic shear, may be compared with the results obtained by HPT processing. ECAP-A-processed age-hardening binary Al-Cu alloys, heat-treated to conditions containing various types of precipitate, showed fracturing and dissolution of the particles during deformation[13, 17, 20]. During HPT the solubility of copper in aluminum may slightly rise due to the applied pressure[21]. Nevertheless a driving force for precipitation is assumed to exists as long as some copper is in solid solution. Hence, to maintain a steady state of torque and a saturated microstructure during HPT of Al-Cu alloys, in addition to a constant defect and boundary density, dynamically balanced formation and dissolution of precipitates should be taken into account. Such processes are thought to be a complex interplay of minimizing interfacial and strain energies[20], governed by diffusion and therefore temperature-dependent. Generally, beside alloying and the strain path, the deformation temperature was found to be an important parameter influencing the limits of refinement[4]. Therefore in this chapter the results will be compared for the typical processing temperatures.

Direct correlation of the in-situ torque with the results of investigations after HPT processing must be considered carefully. The far-from-equilibrium boundary and dislocation structure produced by SPD has a strong tendency to recover. SPD-introduced vacancies are assumed to provide enhanced mobility of copper atoms. Consequently the investigations after HPT processing can never exactly reflect the structure occurring during deformation.

7.1. HPT Deformation

HPT in Liquid Nitrogen

The evaporation temperature of liquid nitrogen (-196°C), for aluminum, represents a homologous temperature of ≈0.1, at which diffusion is assumed to be widely suppressed. Compared with RT processing, during HPT at -196°C the torsional moment is much higher, as shown in figure 7.1(a), and the occurring microstructure should be finer with a higher defect density. Despite the distinctly different in-situ torque, the resulting micro-hardness appears almost equal for both temperatures, as depicted in figure 7.1(b). This contradiction may be explained by recovery after HPT. A huge amount of defects, produced during deformation at the very low temperature, may facilitate a certain coarsening and the formation of a structure which is similar to that developed at RT processing.

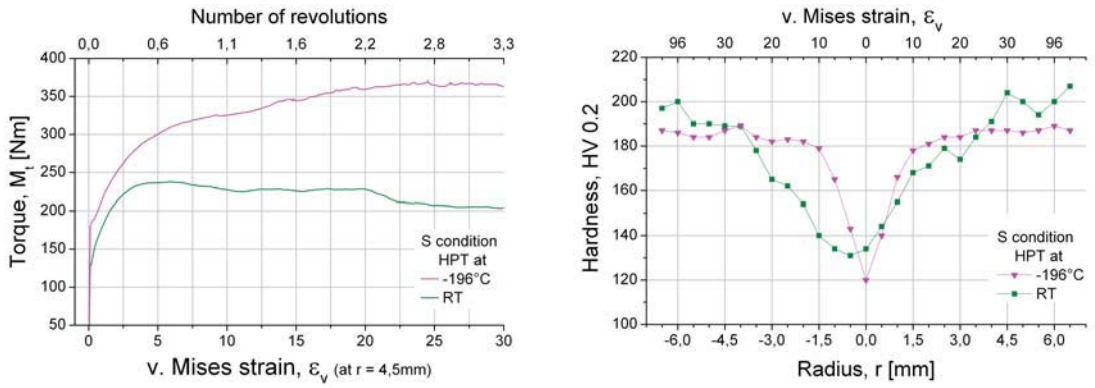

(a) (b)

Figure 7.1.: *Torque during -196 °C and RT HPT deformation(a) and the resulting micro-hardness(b) for S condition material.*

HPT at Room Temperature

The in-situ torque during RT-HPT for the various typical material conditions and the resulting hardness profiles are illustrated in figure 7.2. The inhomogeneous deformation behavior observed within the framework of the pretests may explain the differing central hardness between the S and PA/OA conditions, illustrated in figure 7.2(b). A similar hardness level for all three material conditions of about 180 HV in the highly deformed region possibly indicates an equilibrium structure formed due to recovery at RT during preparation until measurement.

The distinctly different evolution of torque for the S and PA conditions compared with the OA material, as illustrated in figure 7.2(a), may be related to differing interactions between precipitates and dislocations. While the GP zones in S condition material and the θ' particles in PA condition are small enough to be cut by dislocations, the larger θ' precipitates in OA condition are bypassed by the Orowan mechanism.

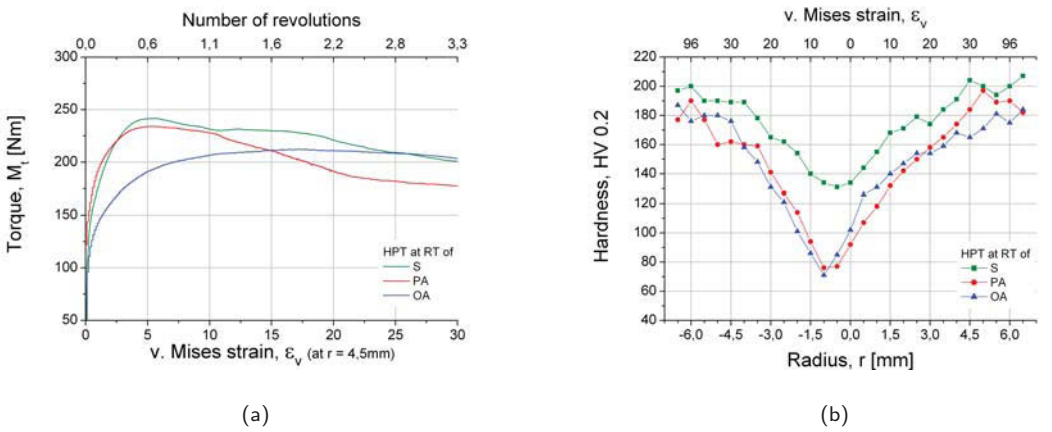

(a) (b)

Figure 7.2.: *Torque during deformation at RT(a) and the resulting micro-hardness(b) for the typical material conditions.*

All three torque curves seem to approach, but do not clearly show, a steady state. This behavior may result from processes of dissolution and formation, possibly transformation of precipitates during HPT, despite the presumption that such phenomena should not occur at RT (homologous temperature ≈0.3). When jumping the speed of rotation (≡strain-rate) during processing, the torque evolution may therefore be interpreted as illustrated in figure 7.3. Additionally the effect may be influenced by the heat generated at the high strain rate and re-cooling at the lower strain-rate. Similar experiments with Al-Mg alloys did not show such pronounced strain-rate sensitivity at RT[16].

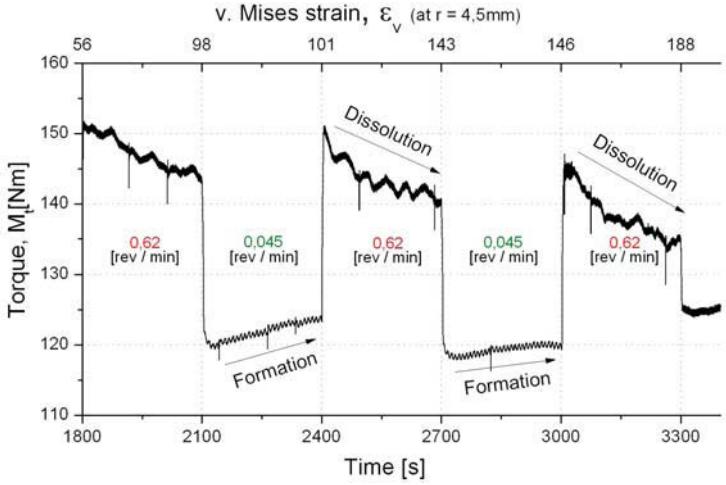

Figure 7.3.: *Detail of the in-situ torque evolution, jumping strain-rate between 0.045 and 0.62 rev/min during RT deformation of an S condition specimen.*

For RT-HPT up to an equivalent strain of ≈10 (≈1 revolution) the microstructural evolution and the resulting hardness are in good agreement with results reported for similar Al-Cu alloys processed by ECAP-A[13, 17, 20]. For the three typical material conditions investigated in this work, the microstructure seems to equalize with further deformation, as illustrated in figure 7.4. The application of very high strain possibly

leads to a structure independent of the initial material condition. A chemical equilibration process, as reported for HPT-processed supersaturated solid solutions of Al-Mg and Al-Zn alloys[15], could explain such behavior.

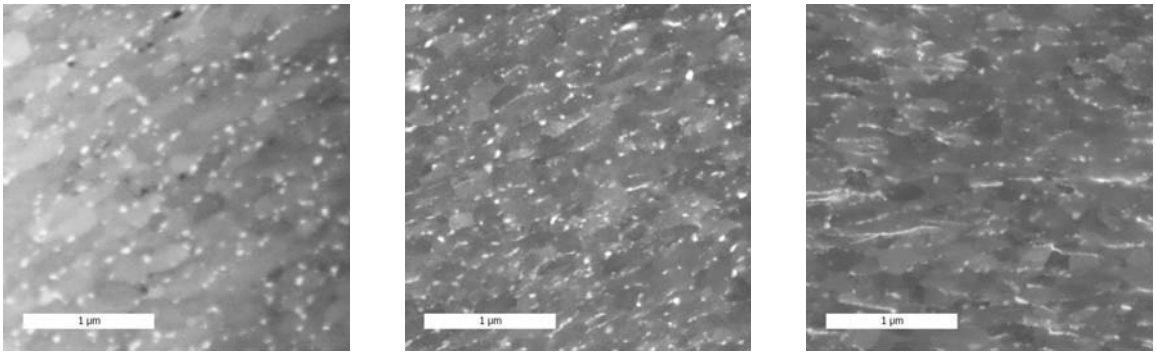

(a) S (b) PA (c) OA

Figure 7.4.: *SEM micro-graphs after HPT at RT for 3.5 revolutions of S condition in axial view(a), PA and OA condition in radial view(b,c), from regions deformed to an equivalent strain of ≈ 30.*

HPT at 100°C

The in-situ torque during 100°C-HPT, and the resulting hardness profiles for the three typical material conditions, are depicted in figure 7.5. A small peak is clearly visible in the hardness profile of the S specimen at r = ± 2 mm, which also appears, less pronounced, on the right-hand side of the PA samples profile. This may indicate the beginning of a strain-dependent dynamic restoration process due to thermally enhanced mobility of dislocations and boundaries at 100°C (homologous temperature of ≈0.4). During RT-HPT the in-situ torque seems to approach a steady state, while during 100°C deformation of S and PA condition the torque shows a continuous decrease, illustrated in figure 7.5(a). In this case the evolution of the torsional moment agrees well with the resulting micro-hardness (figure 7.5(b)), which also shows softening with increasing deformation, pointed out by the dashed boxes in figure 7.5. Although the torque of the OA condition seems to level off in a steady state, the hardness profile does not clearly show a saturation regime, but may have potential to rise with further deformation.

Assuming the grain structure getting finer with decreasing particle size of the second phase, this inverse behavior may be explained by dissolution and precipitation processes. For the S and PA condition, after fragmentation and (partial) dissolution of the small hardening phase particles, softening during deformation may result from continuous growth of precipitates and with it, coupled grain coarsening. In contrast, for the OA condition material, fragments of the initially large particles may continuously shrink, leading to further structural refinement and therefore increasing hardness with increasing degree of deformation.

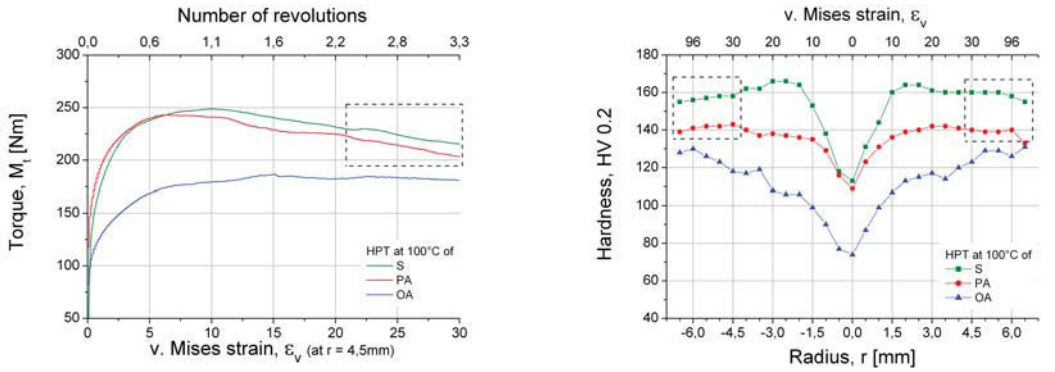

(a) (b)

Figure 7.5.: *Torque during deformation at 100° C(a) and resulting micro-hardness(b) for the typical material conditions. The dashed boxes point out that softening during deformation is reflected by the hardness profiles.*

HPT at 200°C

In figure 7.6 the in-situ torque curves and the micro-hardness profiles after deformation at 200 °C (homologous temperature ≈0.5) are summarised. For S and PA specimens, with respect to the undeformed condition, the hardness in the center is sightly higher, while for radii > 1 mm, hardness is almost equal for both conditions. Similar hardness profiles were found at RT-HPT-processed high purity aluminum[12]. A strain-dependent process, similar to dynamic recrystallisation, is supposed to be responsible for this behavior. For the OA condition, after 200°C HPT, the hardness is slightly lower than that measured on the undeformed specimen. A distinct raise in the outer narrowing part may also suggest a strain-rate-dependent process. The difference between the OA and the S/PA hardness profiles may be related to differing interactions of precipitates and dislocations, but may also result from differing processing temperatures due to the uncertainty of the temperature control. At 200°C the solubility of Cu in Al is significant and solid-solution hardening may also contribute to the as-deformed strength.

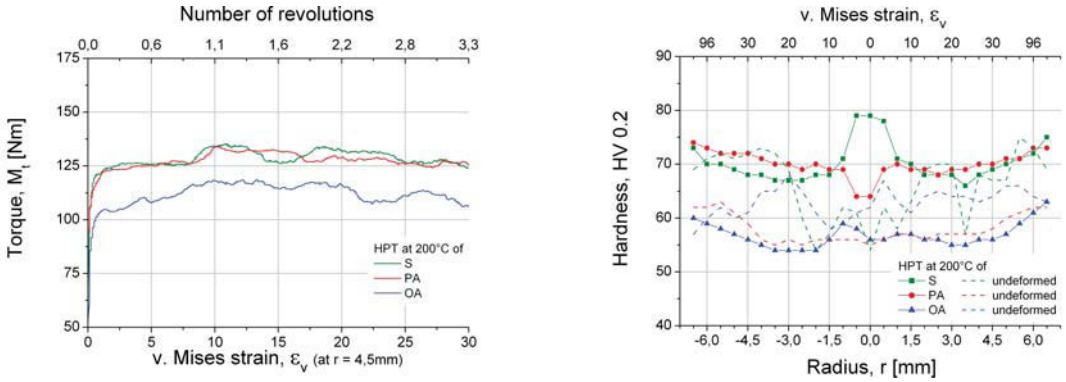

(a) (b)

Figure 7.6.: *Torque during deformation at 200° C(a) and resulting micro-hardness(b) for the typical material conditions.*

7.2. Aging after HPT Deformation

For RT and 100°C HPT-deformed material, the evolution of hardness during aging appears to be nearly the same, as illustrated in figure 7.7. The values of the OA material are slightly lower, but decrease with the same slope. Faster recovery at 100°C, in the period needed to separate the specimen from the heated HPT anvils, may contribute to the distinctly different as-deformed hardness between the different processing temperatures. After 6 minutes at 190°C, hardness becomes equal for both deformation temperatures. Further investigations of 100°C HPT-processed specimens can possibly clarify this behavior.

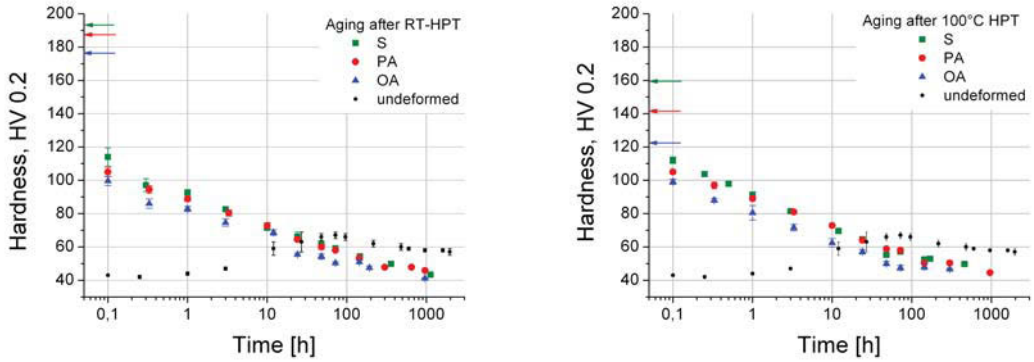

(a) Aging after RT-HPT

(b) Aging after 100°C-HPT

Figure 7.7.: *Hardness evolution during aging at 190 °C after RT HPT(a) and after 100 °C HPT(b) for the typical material conditions. The arrows represent the initial as-deformed hardness values.*

For RT-HPT, from the TEM micrographs in figure 7.8, the average as-deformed grain size can be estimated somewhere around 100 nm; after aging at 190°C for 144h, somewhere around 1 μm. Plotting the grain sizes against the associated hardness values of 1.8 and 0.5 GPa, agrees well with a Hall-Petch plot for SPD-processed customary aluminum foil and Al-Mg alloys done by A. Bachmaier, shown in figure 7.9. Hence,

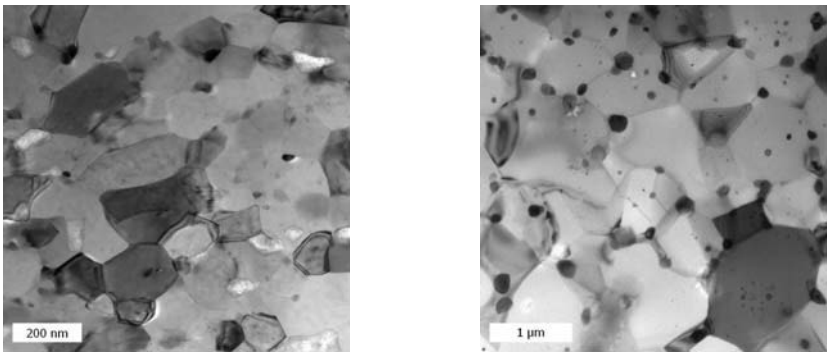

(a) S after RT-HPT

(b) S aged after RT-HPT

Figure 7.8.: *TEM micrographs in axial view: (a) after HPT of S condition at RT for 3.5 revolutions, (b) aged for 144h at 190°C(b), both from a region deformed to an equivalent strain of ≈ 30.*

after RT deformation, the influences on the yield strength of copper in solid solution, precipitates and the dislocation density are supposed to be small. During aging, growth of precipitates at grain boundaries and triple junctions is assumed to be governed by interfacial diffusion of copper[22].

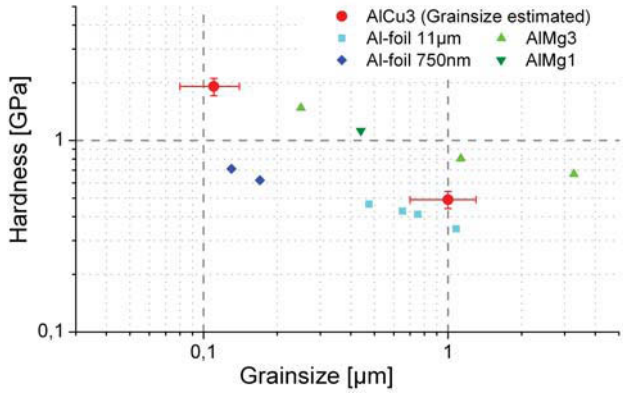

Figure 7.9.: *Chart of the estimated grain size after RT-HPT and after subsequent aging at 190°C for 144h with the associated hardness values, in a Hall-Petch plot for SPD-processed customary Al-foil and Al-Mg alloys, done by A.Bachmaier.*

Aging of the S condition after 200°C HPT shows the approach of a hardness level at about 50 HV, which is not clearly developed for PA and OA material, as illustrated in figure 7.10(a)and (b). The different behavior of the OA condition, showing a rise in the hardness in the early stages of aging, illustrated in figure 7.10(b), may have two possible reasons. On one hand, because of the inaccuracy of the temperature control, the specimen (sectioned after HPT), on which the initial as-deformed hardness and the values for the marked data points were measured, was possibly deformed at a somewhat higher temperature. On the other hand,

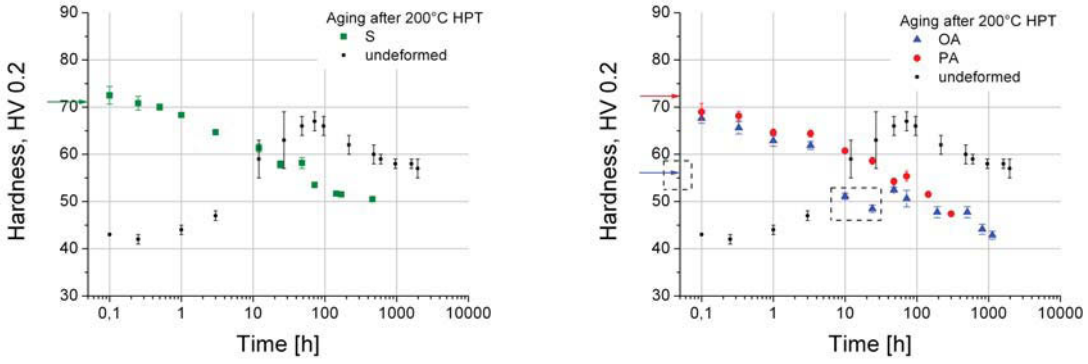

(a) (b)

Figure 7.10.: *Hardness evolution during aging at 190°C after 200°C HPT deformation of: (a) S material, (b) PA and OA material. The arrows indicate the initial as-deformed hardness. Each curve was measured on two (sectioned) samples. The OA sample, on which the as-deformed hardness and the values for the marked data points in (b) were measured, was possibly deformed at a somewhat higher temperature due to inaccuracy of the temperature control.*

the grain size of the OA material after 200°C-HPT may be large enough for hardening precipitates to form in the grain interior in the early stage of subsequent aging.

For comparison figure 7.11 shows SEM images of the precipitate-free-zone in almost unstrained OA raw material, and the grain structure of an S condition specimen after 200°C deformation. The width of the precipitate-free-zone and the grain size after 200°C-HPT (S condition) are of comparable order of magnitude. According to the differing hardness profiles in figure 7.6(b) the grain size of the OA condition is possibly larger than that of the S condition.

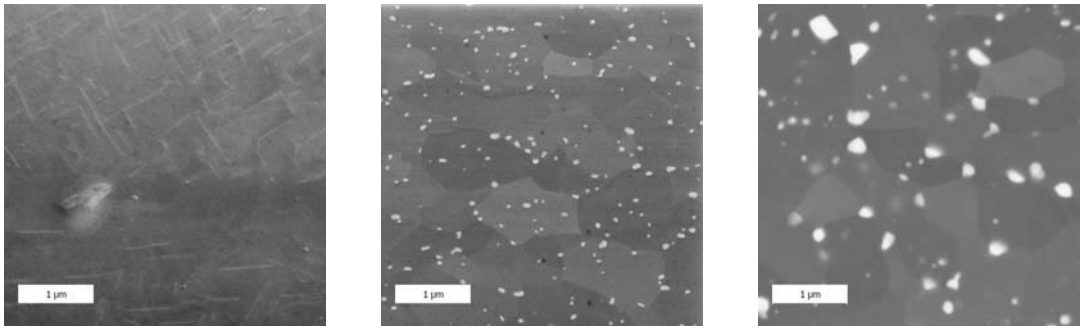

(a) (b) (c)

Figure 7.11.: *SEM images of: (a) the precipitate-free-zone of the OA conditioned raw material, (b) the microstructure of 200° C-HPT-processed S condition material, (c) aged for 144h at 190° C after 200° C-HPT.*

The images in figure 7.12 show the microstructure of S condition material, after HPT-processing at the various typical temperatures and subsequent aging at 190°C for 144h . For very long aging time the grain size appears to level off at ≈2 μm. Because of very similar hardness values after long aging times, a similar microstructure is expected to form when aging PA/OA material after HPT processing.

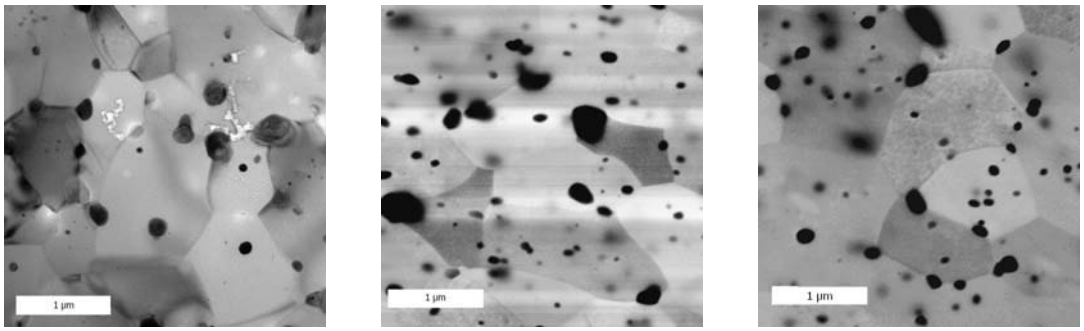

(a) aged after RT-HPT (b) aged after 100°C-HPT (c) aged after 200°C-HPT

Figure 7.12.: *TEM brightfield(a) and gray-scale-inverted SEM(b,c) micro-graphs of HPT-processed S condition material, aged at 190° C for 144h after: RT-HPT(a), 100° C-HPT(b), 200° C-HPT(c). All images were recorded in areas initially deformed to an equivalent strain of approximately 30.*

By comparing the hardness evolution of the undeformed material, represented by the small black symbols in the figures 7.7 and 7.10, with that of the HPT-deformed material, two interesting phenomena can be noticed. Firstly, during aging the hardness of the HPT deformed material falls below the peak hardness of the raw material. Secondly, the hardness of the raw material for very short aging approximately equals hardness of HPT-processed material aged for very long time. The effect of solid-solution hardening in the undeformed material seems to equal approximately hardening according to the Hall-Petch relation, due to a grain size of ≈1-2 μm.

7.3. Summary

By HPT-processing in the investigated Al-Cu alloy, an UFG structure was obtained. The hardening precipitates in S and PA condition are disrupted and possibly dissolved during deformation up to an equivalent strain of ≈10. Further deformation leads to a microstructure consisting of high-angle grain boundaries and incoherent grain-boundary precipitates. The structure produced by SPD up to very high strain is possibly independent of the initial material condition, due to a process of chemical equilibration.

A definite saturation structure and a clear steady-state of the torque were not observed within the investigated deformation range, presumably due to dissolution and precipitation of second-phase particles during HPT. Sheared GP-zones in S condition and small fragments of θ' precipitates in PA condition may dissolve due to increasing surface free energy with decreasing particle size. Large fragments of the precipitates in OA condition seem to congregate at grain boundaries, possibly reducing the grain interfacial energy and the grain boundary mobility.

The grain size appears to increase with increasing deformation temperature and to decrease with decreasing particle size of the second phase. The strength of the HPT-processed material, according to the Hall-Petch relation, is mainly governed by the grain size, which was found to be between ≈100 nm after RT-HPT and ≈1 μm after 200°C-HPT.

When aging the HPT-processed material at 190°C, hardening (metastable) phases could not be found. Only incoherent grain-boundary precipitates were found to grow, supposedly by interfacial diffusion of copper. Grain growth during aging seems to be limited by the grain-boundary precipitates. For all the investigated material conditions and deformation temperatures, after ≈2 days at the typical aging temperature, the hardness of the HPT-processed material falls below the peak hardness of the undeformed material to a level between 40 and 50 HV.

APPENDIX

A. Aging of B Samples

The scatter of the hardness values in the aging characteristic for an aging temperature of 180 °C determined for B samples is not stochastic but originates from patterns of hardness due to grain structure and quenching conditions. The hardness measured for each sample is shown in figure A.1. For clarity at maximum three graphs showing similar patterns were combined in each diagram.

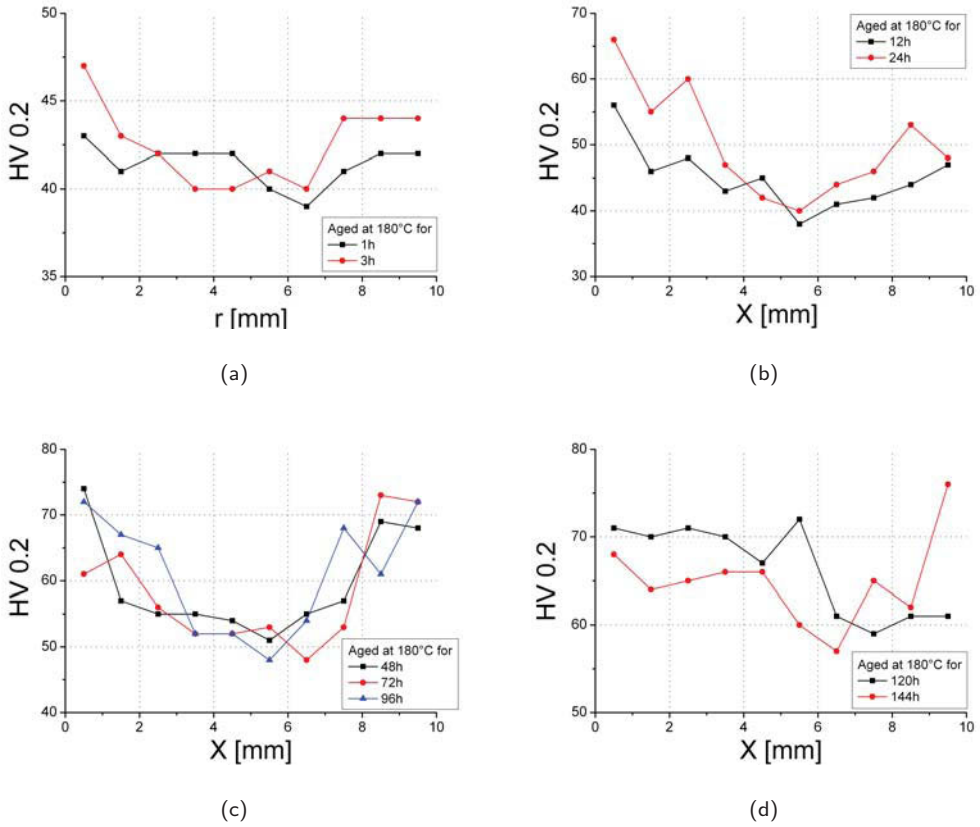

Figure A.1.: *Patterns of micro-hardness measured on B samples to determine the aging characteristic for 180 °C. Note the different hardness scales.*

B. Aging of C Samples

The micro-hardness values in the aging characteristic of the raw material measured for C samples, shown in sections 2.5 and 2.6, are not randomly scattered but show distinct patterns. The hardness measured on the naturally aged samples is illustrated in figure B.1, the values depicted in figures B.3 and B.2 were measured on artificially aged specimens. For each plot a different hardness scale was chosen to point out the patterns more clearly.

Natural Aging

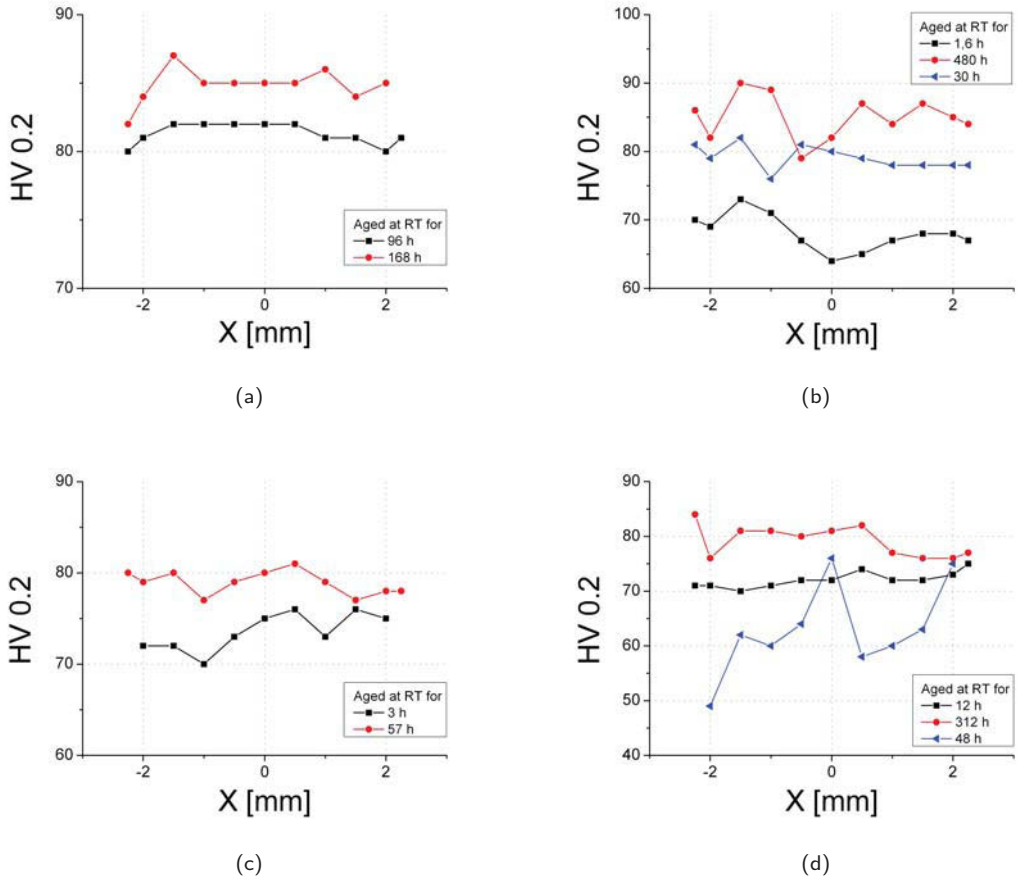

Figure B.1.: *Patterns in micro-hardness measured on C samples to determine the natural aging characteristic.*

Artificial Aging

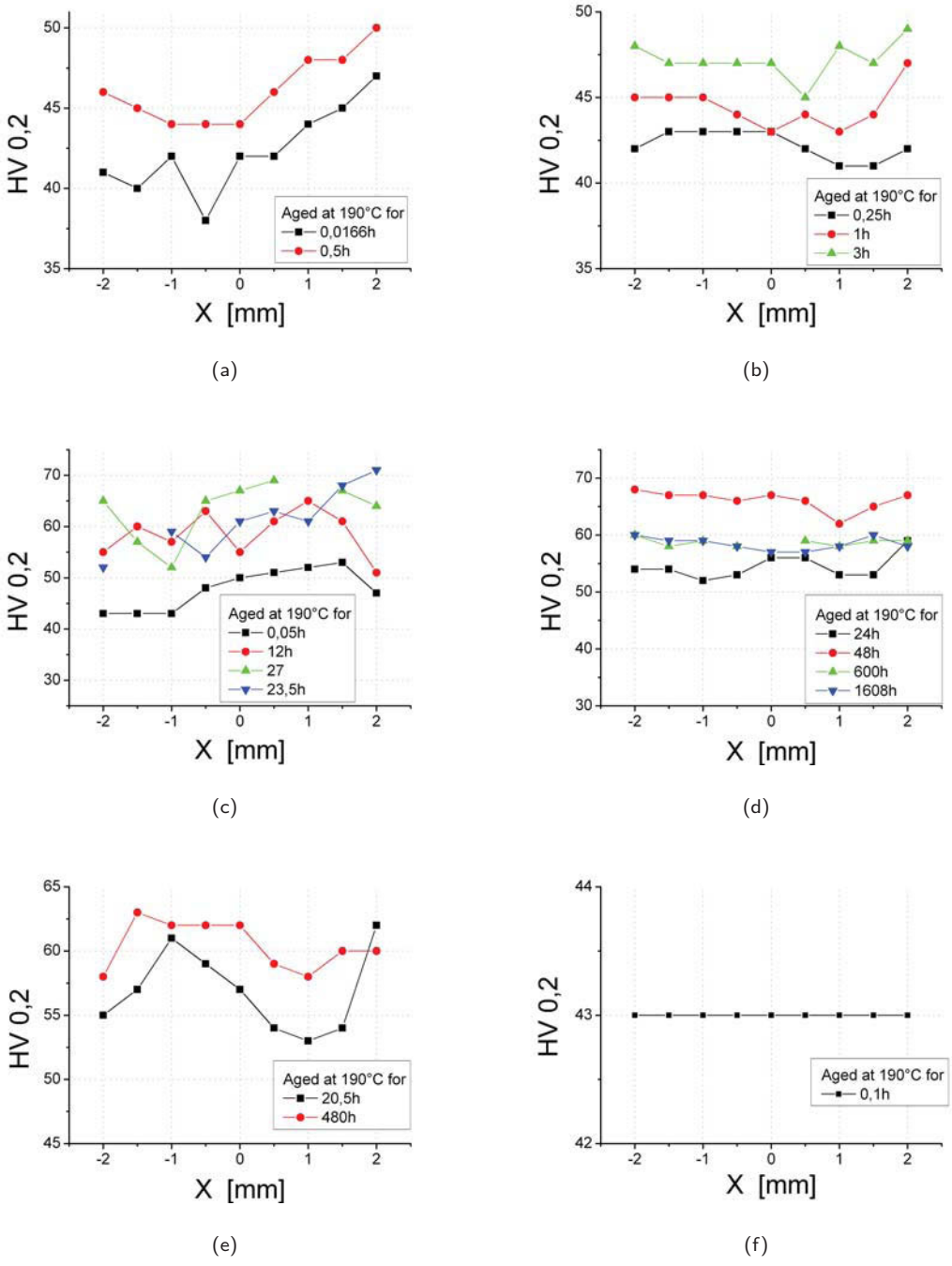

Figure B.2.: *Patterns in micro-hardness measured on C samples to determine the artificial aging characteristic.*

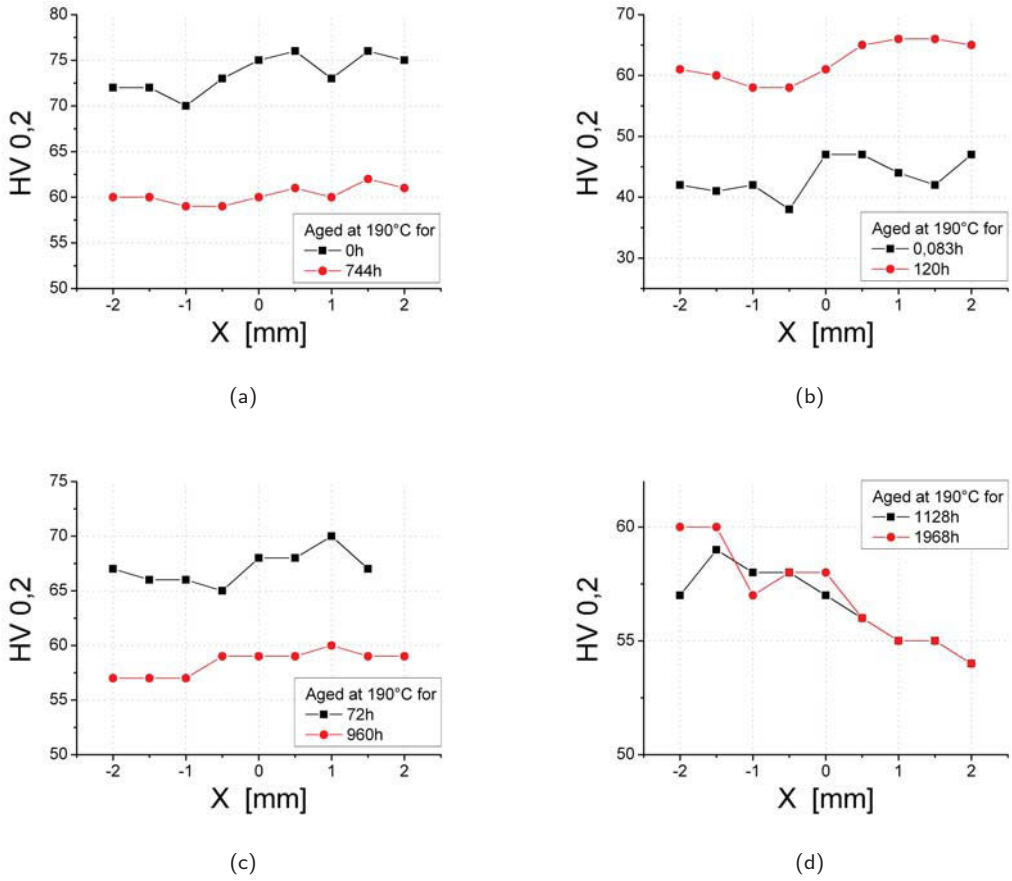

Figure B.3.: *Patterns in micro-hardness measured on C samples to determine the artificial aging characteristic.*

C. Torque during HPT Deformation

The individual torque curves recorded during deformation are shown in figures C.1, C.2 and C.3 on the left hand side. For the S condition a peak or peak/plateau characteristic was observed at RT and 100°C processing. To point out more clearly the tendency for each temperature in figure C.1, the dotted graphs were omitted from the calculation of mean and standard deviation, depicted on the right.

S Condition

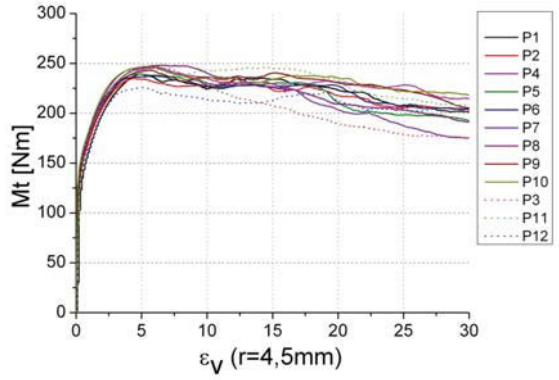

(a) S: RT

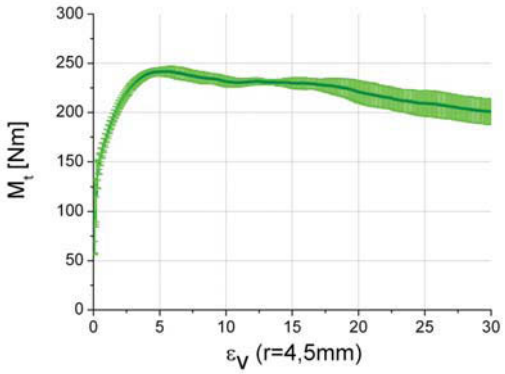

(b) S: RT Mean

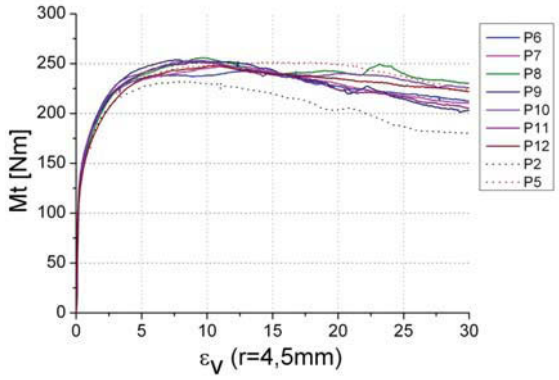

(c) S: 100°C

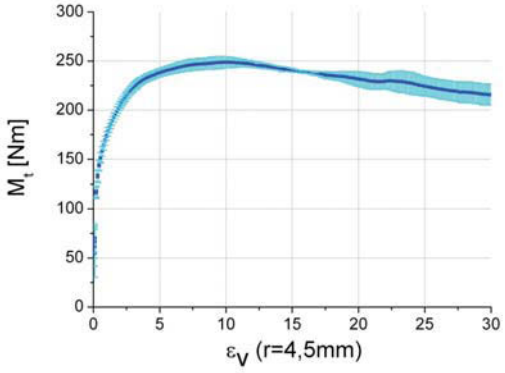

(d) S: 100°C Mean

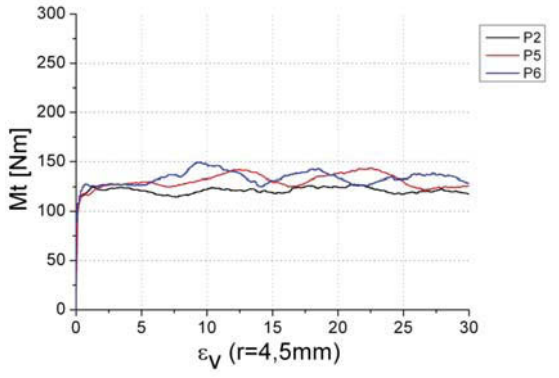

(e) S: 200°C

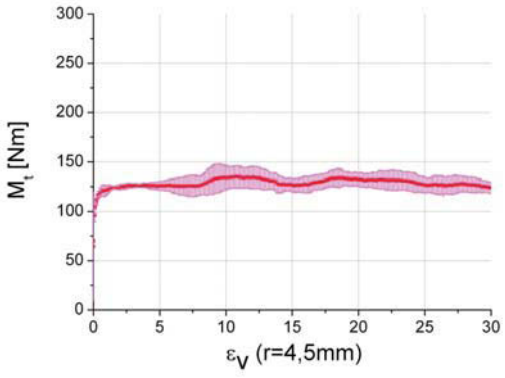

(f) S: 200°C Mean

Figure C.1.: *Torsional moment measured on S conditioned samples, in situ during HPT deformation for 3.5 turns, at RT, 100°C and 200°C. The single curves measured at each particular temperature are shown in (a), (c) and (e). The graphs in (b),(d) and (f) are calculated mean value and standard deviation of the associated values on the left, with the dotted lines excepted.*

PA Condition

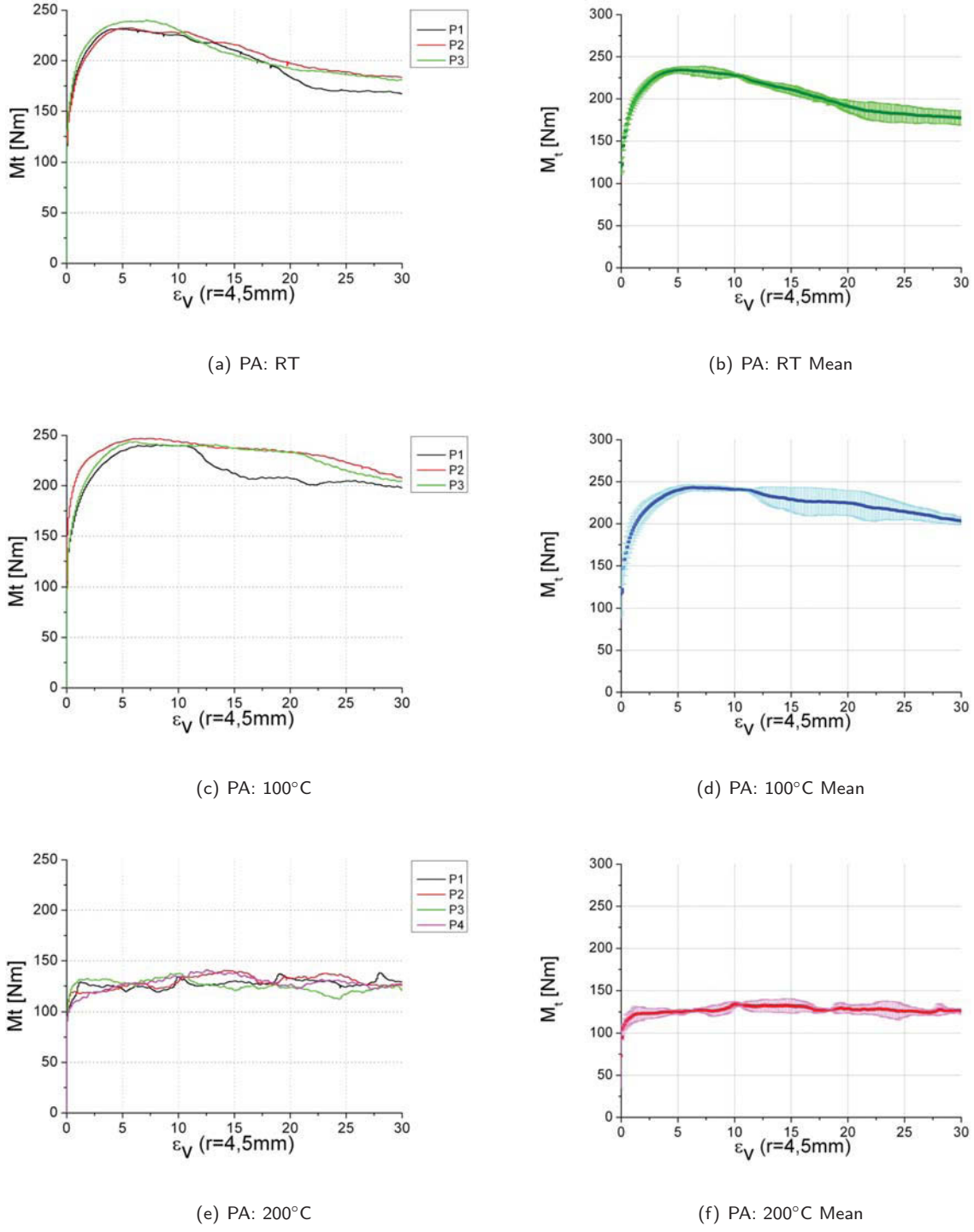

(a) PA: RT

(b) PA: RT Mean

(c) PA: 100°C

(d) PA: 100°C Mean

(e) PA: 200°C

(f) PA: 200°C Mean

Figure C.2.: *Torsional moment measured on PA conditioned samples, in situ during HPT deformation for 3.5 turns, at RT, 100°C and 200°C. The single curves measured at each particular temperature are shown in (a), (c) and (e). The graphs in (b),(d) and (f) are calculated mean value and standard deviation of the associated values on the left.*

OA Condition

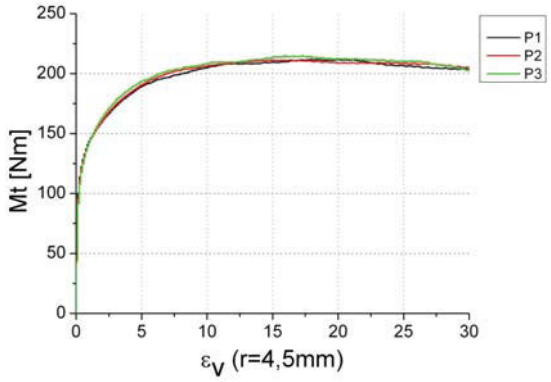

(a) OA: RT

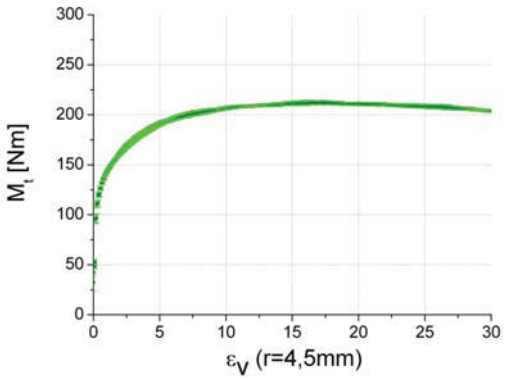

(b) OA: RT Mean

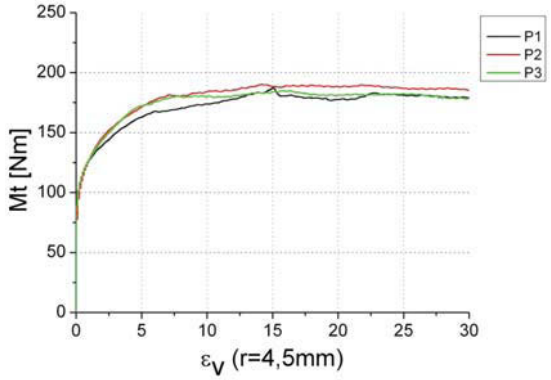

(c) OA: 100°C

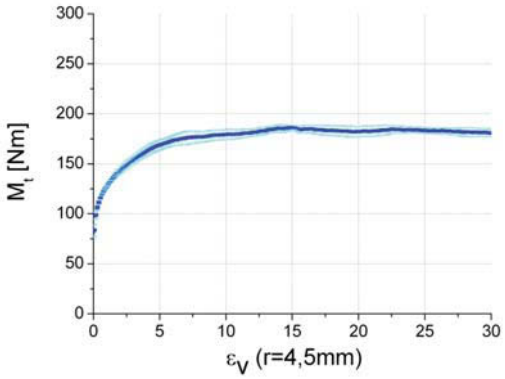

(d) OA: 100°C Mean

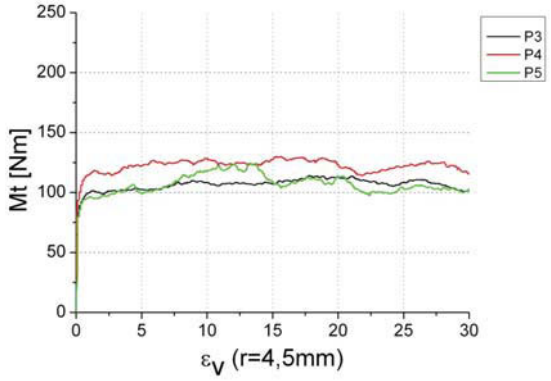

(e) OA: 200°C

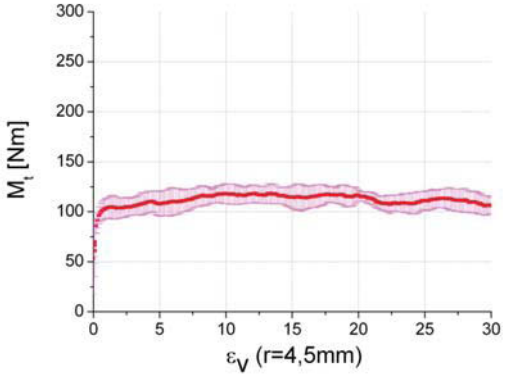

(f) OA: 200°C Mean

Figure C.3.: *Torsional moment measured on OA conditioned samples, in situ during HPT deformation for 3.5 turns, at RT, 100°C and 200°C. The single curves measured at each particular temperature are shown in (a), (c) and (e). The graphs in (b),(d) and (f) are calculated mean value and standard deviation of the associated values on the left.*

D. Aging after HPT Deformation

Figures D.1, D.2, D.3 and D.4 show the full data set corresponding to the aging characteristics described in Section 6. The aging curves were constructed as outlined in section 4.2.

S Condition

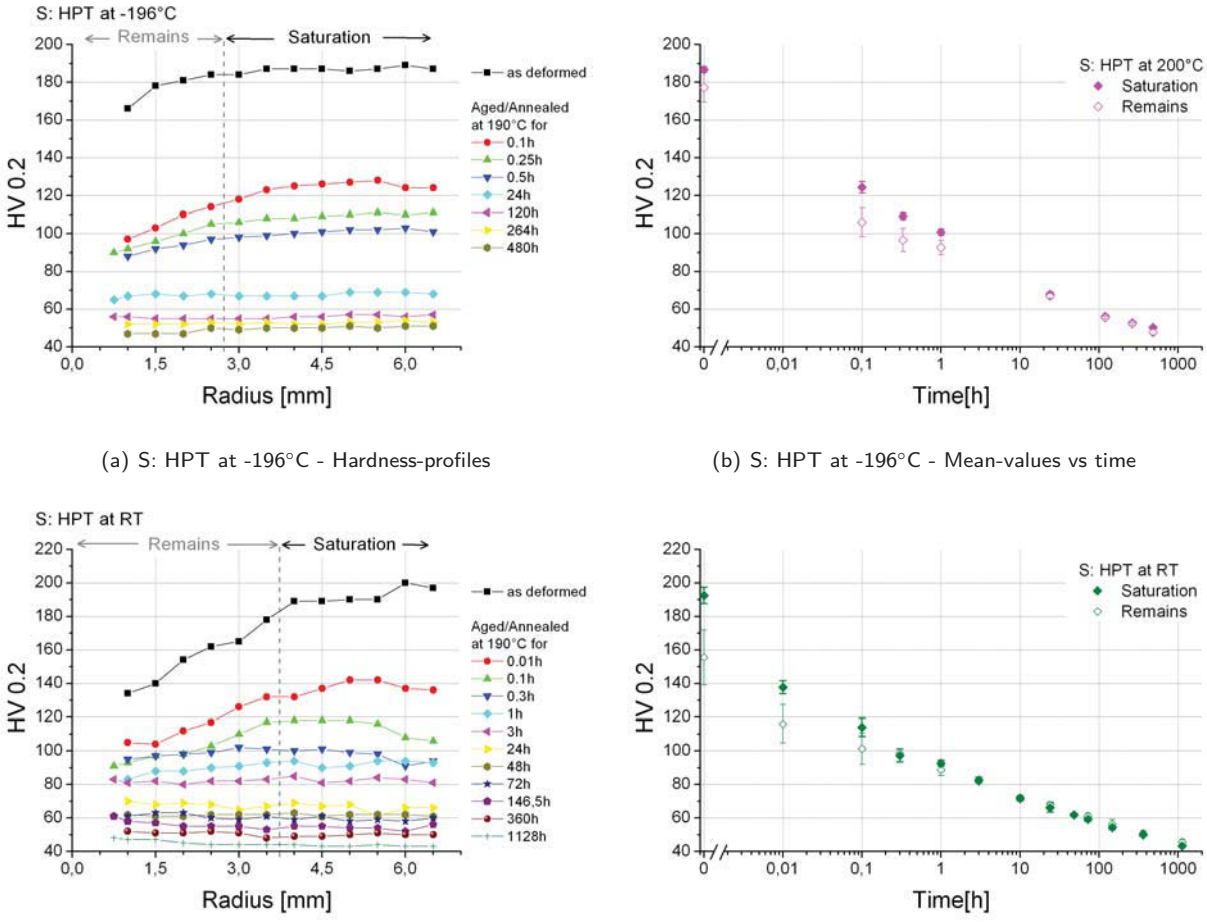

(a) S: HPT at -196°C - Hardness-profiles

(b) S: HPT at -196°C - Mean-values vs time

(c) S: HPT at RT - Hardness-profiles

(d) S: HPT at RT - Mean-values vs time

Figure D.1.: *Aging characteristic of S conditioned samples after HPT deformation for 3.5 turns, at -196 °C in (a) and (b), and at RT in (c) and (d). Note the different hardness scales.*

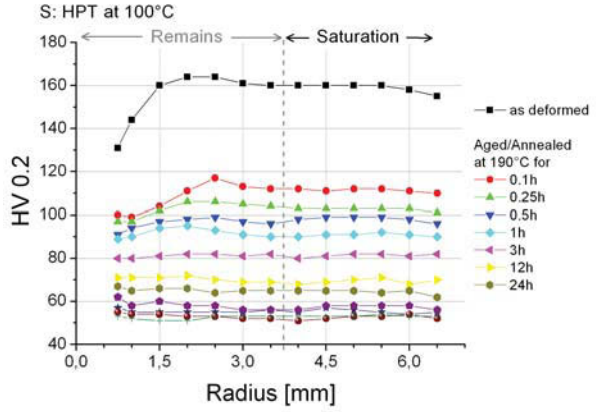

(a) S: HPT at 100°C - Hardness-profiles

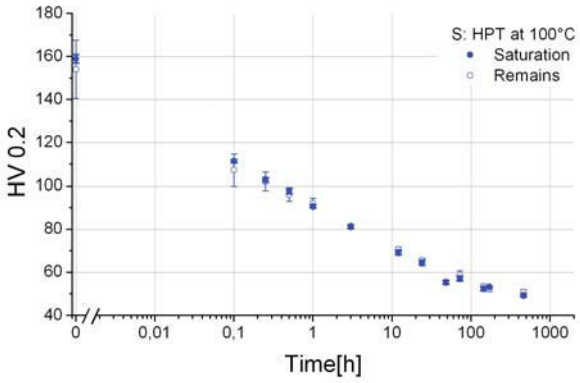

(b) S: HPT at 100 °C - Mean-values vs time

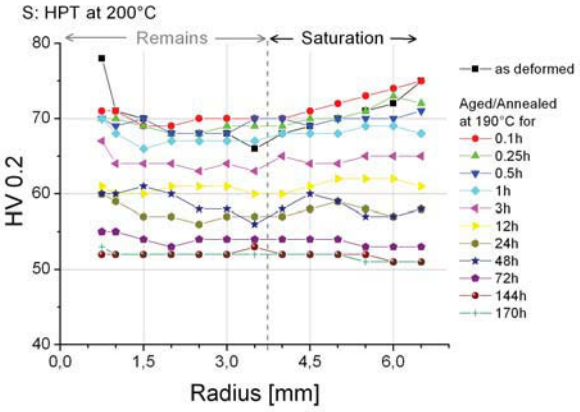

(c) S: HPT at 200 °C - Hardness-profiles

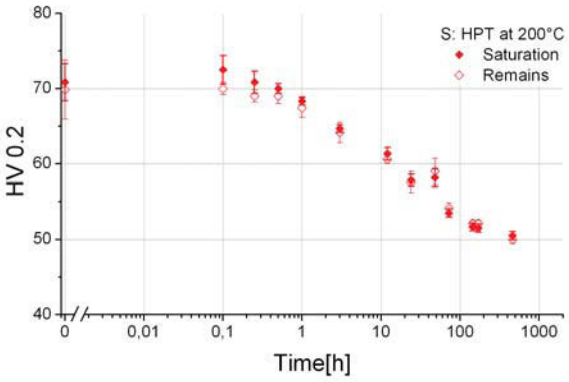

(d) S: HPT at 200 °C - Mean-values vs time

Figure D.2.: *Aging characteristic of S conditioned samples after HPT deformation for 3.5 turns, at 100°C in (a) and (b), and at 200°C in (c) and (d). Note the different hardness scales.*

PA Condition

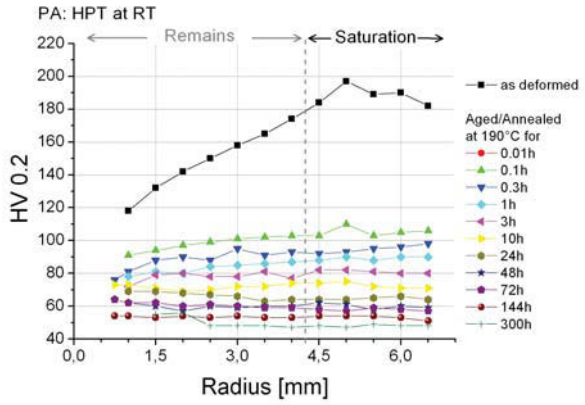

(a) PA: HPT at RT - Hardness-profiles

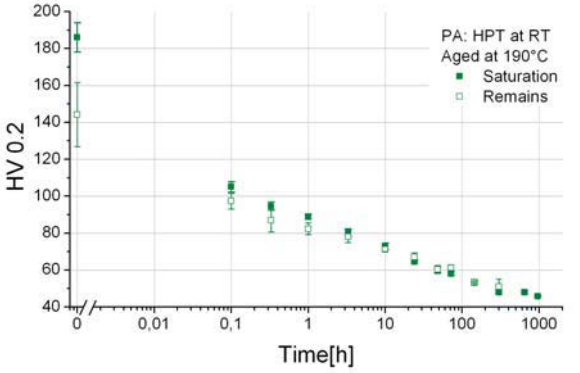

(b) PA: HPT at RT - Mean-values vs time

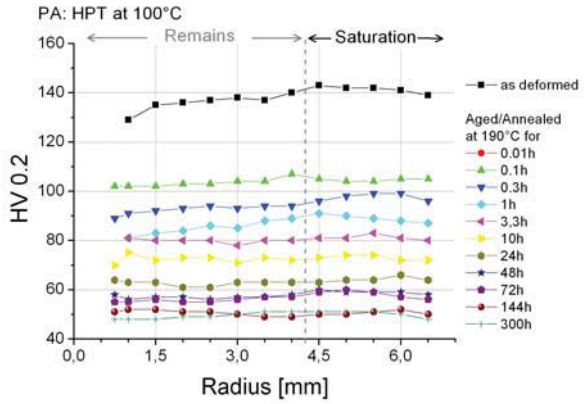

(c) PA: HPT at 100°C - Hardness-profiles

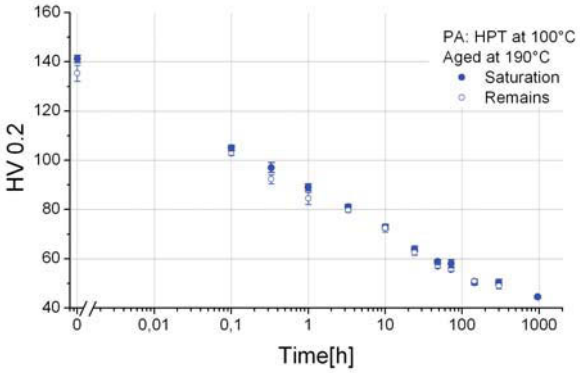

(d) PA: HPT at 100°C - Mean-values vs time

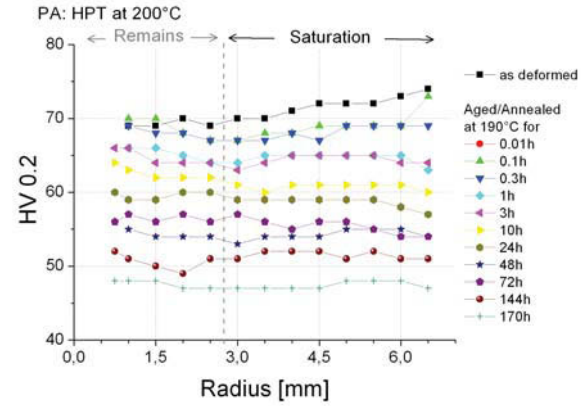

(e) PA: HPT at 200°C - Hardness-profiles

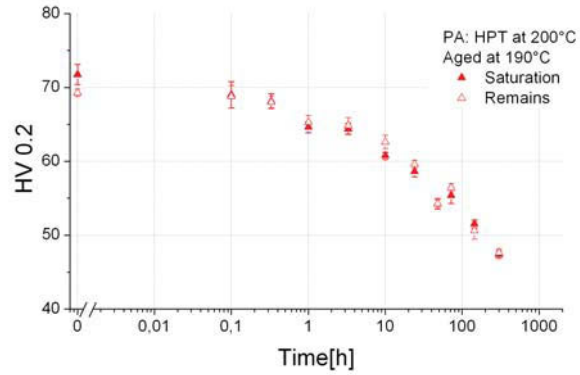

(f) PA: HPT at 200°C - Mean-values vs time

Figure D.3.: *Aging characteristic of PA conditioned samples after HPT deformation at RT (a;b), at 100°C in (c;d) and at 200°C (e;f) for 3.5 turns at 2.1 GPa and 0.2 rev/min. Note the differing hardness scales.*

OA Condition

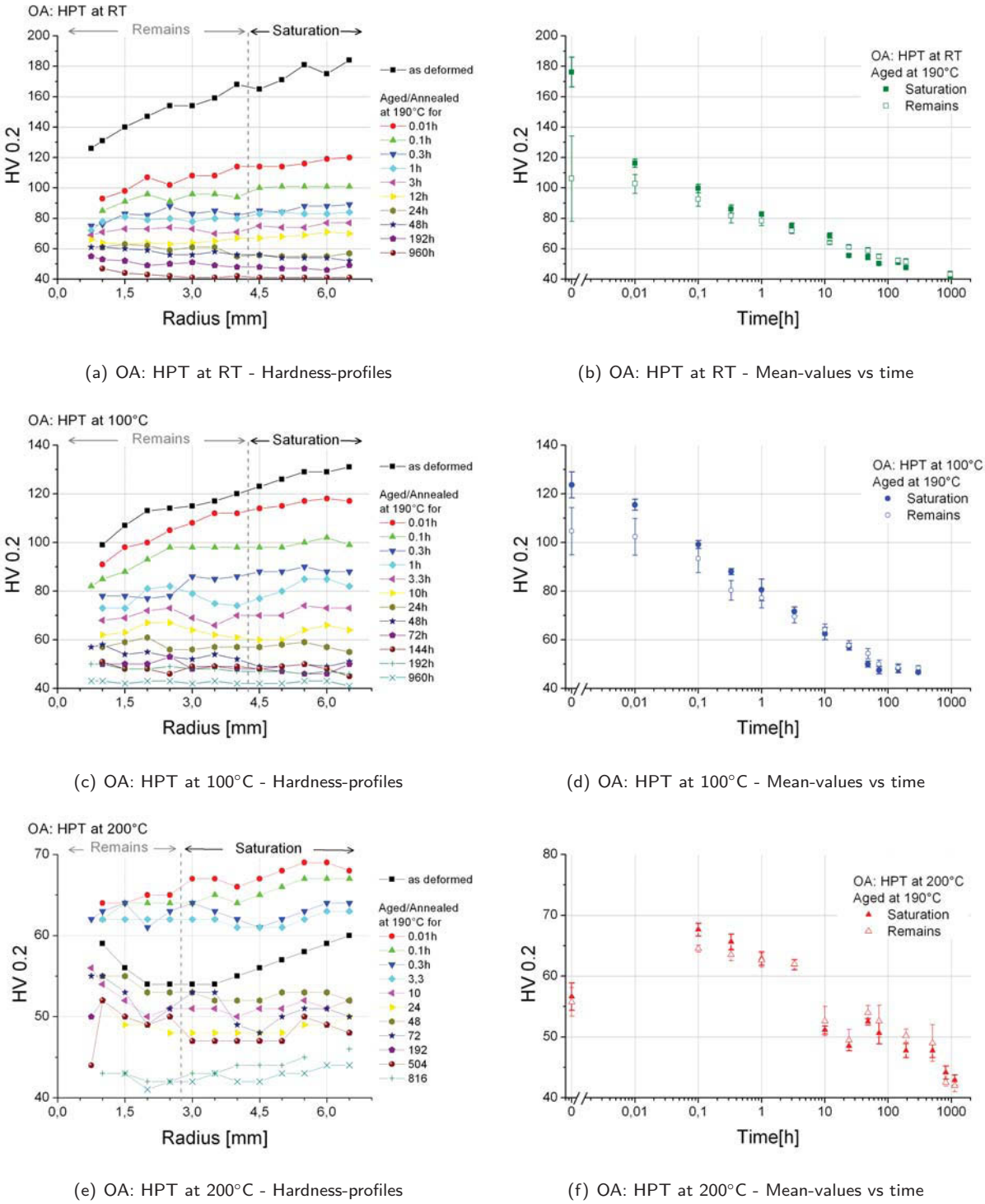

(a) OA: HPT at RT - Hardness-profiles

(b) OA: HPT at RT - Mean-values vs time

(c) OA: HPT at 100°C - Hardness-profiles

(d) OA: HPT at 100°C - Mean-values vs time

(e) OA: HPT at 200°C - Hardness-profiles

(f) OA: HPT at 200°C - Mean-values vs time

Figure D.4.: *Aging/Annealing characteristic of OA conditioned samples after HPT deformation at RT (a;b), at 100°C in (c;d) and at 200°C (e;f) at 2.1 GPa and 0.2 rev/min. Note the differing hardness scales.*

List of Figures

List of Tables

Literature

[1] J.W. Martin. *Precipitation Hardening.* Pergamon Press, 1968.

[2] R. Z. Valiev, Y. Estrin, Z. Horita, T. G. Langdon, M. J. Zechetbauer, and Y. T. Zhu. Producing bulk ultrafine-grained materials by severe plastic deformation. *JOM Journal of the Minerals, Metals and Materials Society*, Volume 58; Issue - 4:33–39, 2006.

[3] R.Z. Valiev, R.K. Islamgaliev, and I.V. Alexandrov. Bulk nanostructured materials from severe plastic deformation. *Progress in Materials Science*, 45:103–189, 2000.

[4] R. Pippan, F. Wetscher, M. Hafok, A. Vorhauer, and I. Sabirov. The limits of refinement by severe plastic deformation. *Advanced Engineering Materials*, 8(11):1046–1056, 2006.

[5] A. Bachmaier, A. Hohenwarter, and R. Pippan. New procedure to generate stable nanocrystallites by severe plastic deformation. *Scripta Materialia*, 61:1016–1019, 2009.

[6] D.A. Porter and K.E. Easterling. *Phase Transformations in Metals and Alloys.* Chapman & Hall, 2nd edition, 1992.

[7] D. Altenpohl. *Aluminium Viewed from Within.* Aluminium-Verlag, Düsseldorf, 1982.

[8] vol. ed. H. Mughrabi. *Materials Science and Technology: Vol.6. Plastic deformation and fracture of materials.* Weinheim; New York , Basel; Cambridge : VCH., 1993.

[9] P.N.T. Unwin, G.W. Lorimer, and R. B. Nicholson. The origin of the grain boundary precipitate free zone. *Acta Metallurgica*, 17:1363–1377, 1969.

[10] P.W. Bridgeman. Effects of high shearing stress combined with high hydrostatic pressure. *Physical Review*, 48:825–847, 1935.

[11] K. Edalati, Z. Horita, and T.G. Langdon. The significance of slippage in processing by high-pressure torsion. *Scripta Materialia*, 60(1):9 – 12, 2009.

[12] Yuki Ito and Zenji Horita. Microstructural evolution in pure aluminum processed by high-pressure torsion. *Materials Science and Engineering: A*, 503(1-2):32 – 36, 2009. International Symposium on Bulk Nanostructured Materials: from Fundamentals to Innovation, BNM 2007.

[13] C. Xu, Z. Horita, and T.G. Langdon. The evolution of homogeneity in an aluminum alloy processed using high-pressure torsion. *Acta Materialia*, 56(18):5168 – 5176, 2008.

[14] A.P. Zhilyaev, K. Oh-ishi, T.G. Langdon, and T.R. McNelley. Microstructural evolution in commercial purity aluminum during high-pressure torsion. *Materials Science and Engineering: A*, 410-411:277 – 280, 2005. The Langdon Symposium: Flow and forming of Crystalline Materials.

[15] B.B. Straumal, B. Baretzky, A.A. Mazilkin, F. Phillipp, O.A. Kogtenkova, M.N. Volkov, and R.Z. Valiev. Formation of nanograined structure and decomposition of supersaturated solid solution during high pressure torsion of al-zn and al-mg alloys. *Acta Materialia*, 52:4469–4478, 2004.

[16] A. Bachmaier, M. Hafok, and R. Pippan. Rate independent and rate dependent structural evolution during severe plastic deformation. *MATERIALS TRANSACTIONS*, 51(1):8–13, 2010.

[17] M. Murayama, Z. Horita, and K. Hono. Microstructure of two-phase al-1.7at%cu alloy deformed by equal-channel angular pressing. *Acta Materialia*, 49:21–29, 2001.

[18] E.F. Prados, V.L. Sordi, and M. Ferrante. Microstructural development and tensile strength of an ecap - deformed al-4 wt%cu alloy. *Materials Research*, 11, No.2:199–205, 2008.

[19] Z. Horita, K. Ohashi, T. Fujita, K. Kaneko, and T.G. Langdon. Achieving high strength and high ductility in precipitation hardened alloys. *Advanced Materials*, 17:1599–1602, 2005.

[20] Xiao-chang XU, Zhi-yi LIU, Yun-tao LI, Peng DANG, and Su-min ZENG. Evolution of precipitates of al-cu alloy during equal-channel angular pressing at room temperature. *Transactions of Nonferrous Metals Society of China*, 18(5):1047 – 1052, 2008.

[21] T. Soma, M. Ishizuka, and H. Matsuo Kagaya. Solid solubility of cu in al under pressure and elastic moduli. *physica status solidi (b)*, 186(1):95–100, 1994.

[22] H. B. Aaron and H.I. Aaronson. Growth of grain boundary precipitates in al-4%cu by interfacial diffusion. *Acta Metallurgica*, 16:789–798, 1968.